Comprehensive Transport Studies Of Topological Kondo Insulator Samarium Hexaboride

by

Dmitri Mihaliov

A dissertation submitted in partial fulfillment
of the requirements for the degree of
Doctor of Philosophy
(Applied Physics)
in the University of Michigan
2026

Doctoral Committee:
Professor Cagliyan Kurdak, Co-Chair
Professor Lu Li, Co-Chair
Associate Professor John Heron
Professor Kai Sun

Dmitri Mihaliov

dmitrim@umich.edu

ORCID iD: 0000-0002-6993-3621

©Dmitri Mihaliov 2026

Dedication

For Those Who Come After

Acknowledgements

Firstly, I would like to acknowledge the pivotal role in my formation as a researcher by Professor Çağlıyan Kurdak. His willingness to take me on as an lab assistant in my first year in undergrad was directly responsible for allowing me to pursue further academic studies into this present thesis. His excitement for physics and focus on teaching things in a "real world" way, i.e. being tangible and being able to be understood in the context of everyday life, developed within me a deep appreciation for physics and a grounded way in approaching research. More than that he indeed has been a father to me, and I consider him, Dr. Nadine Wang, Kaya and Ayla to be family, and I am forever grateful to have met them.

I would like to also acknowledge Professor Lu Li as an irreplaceable mentor. His balanced approach towards research, being both driven and precise in experimentation whilst simultaneously caring and supportive of his students is exemplary and should be a model for how all research labs in the University of Michigan should operate. Furthermore, his willingness to try new approaches and truly wrestle with the data embodies the academic ideals.

At the University of Michigan, I have been very fortunate to have learned under, and collaborated with, many professors who have taught me many new subjects and ways of approaching problems that I never would have considered before. In this I particularly want to thank Professor Kai Sun whose theoretical groundwork in SmB_6 was crucial in the development of studies into the material and to this thesis. In addition, his explanations of physics theories and concepts, both during lectures and in conversations, were immensely helpful in the advancing of my own understanding.

My time as a researcher would not have been quite the same without the wonderful members of my research groups. Professor Yun Suk Eo provided much elucidation and guidance to me during my time researching as an undergraduate. Also during my time as an under-

graduate, I worked closely with Dr. Bret Gergely whose proactive approach really brought up zeal in experimentation. I think fondly of the many thought-provoking conversations over a multitude of subjects that we've had. I would like to also thank Dr. Kuan-Wen Chen for much support he gave me during experiments using the cryogenic systems. During my time as a graduate researcher, I was privileged to share an office with Dr. Armando Gil and Shriya Sinha, who have not only been immensely helpful in their aid to experiments conducted, but also provided a fun atmosphere with solid banter. In addition I would like to acknowledge Eric Chandler, Arun Bhattacharya, Yuting Zhang, and Zecheng You for their contributions to the experiments.

This research could not have been done without the collaboration of Dr. Priscila Rosa for sharing her expertise on sample growth and strongly correlated materials. Her guidance and supplying of SmB_6 samples allowed us to collect the findings of this thesis. Furthermore, I would like to thank Dr. Pilar Herrera-Fierro and Dr. Robert Nidetz in providing expertise on the tools and techniques available in the Laurie Nanofabrication Facility.

Most of all, I would like to profess my undying love for my wife, Dr. Alexa Mihaliov, who not only supported me as my wife, but also in conducting research, analyzing data, and correcting/improving my writing. It's no understatement to say that without her this thesis would never have been made. And of course, I want to thank my mother, Irina Loukina, whose steadfastness through all of life's ups and downs, and true love, allowed me to be where I am today.

Funding for this work was provided by NSF AGEP #1707620. The PPMS system, which was used for cryogenic measurements, was acquired through the NSF MRI Award No. 1428226. I acknowledge the University of Michigan College of Engineering for financial support and the Michigan Center for Materials Characterization and the Laurie Nanofabrication Facility for use of the instruments and staff assistance. And finally, I would like thank the Applied Physics Program at the University of Michigan for providing financial support through its student fellowships.

Table of Contents

Dedication ii

Acknowledgements iii

List of Figures viii

List of Tables xi

Abstract xii

Chapter 1 Introduction 1

1.1 Early Measurements . . . 2

1.1.1 Magnetic Anomalies and Van Vleck Susceptibility . . . 3

1.1.2 Spectroscopic Evidence for Mixed Valence . . . 4

1.1.3 Mixed-Valence Phenomenology and Chemical Tuning . . . 4

1.1.4 Hybridization, the Kondo Lattice, and Gap Formation . . . 6

1.1.5 Magnetotransport: Anomalous Negative Magnetoresistance . . . 7

1.2 Topological Insulators . . . 7

1.3 Revisiting SmB_6 as a Topological Kondo Insulator . . . 9

1.3.1 Theoretical Prediction . . . 9

1.3.2 Electrical Transport . . . 11

1.3.3 Spectroscopy . . . 12

1.3.4 Magnetotransport . . . 15

1.4 Unresolved Questions for SmB_6 . . . 16

1.4.1 Dependence of Results on Experimental Method . . . 16

1.4.2 Impurities . . . 18
1.4.3 Quantum oscillations . . . 19

Chapter 2 Methods and Techniques **22**
2.1 Growth Methods . . . 22
2.1.1 Flux Growth . . . 22
2.1.2 Floating Zone Growth . . . 24
2.1.3 Point Defects And Dislocations . . . 25
2.2 Preparation Of Crystal Surfaces . . . 25
2.3 Transport Analysis . . . 26
2.3.1 Two-channel conductivity . . . 28
2.3.2 Connection to measurement . . . 29
2.4 Establishing Transport Geometry . . . 30
2.4.1 Hall bar geometry . . . 31
2.4.2 Van der Pauw geometry . . . 31
2.4.3 Corbino geometry . . . 32
2.4.4 Inverted resistance measurements . . . 32
2.4.5 Fabrication . . . 35
2.4.6 Contact Corrections . . . 36

Chapter 3 Bulk Measurements of Pure and Doped SmB_6 **37**
3.1 Introduction . . . 37
3.2 Comparing Samples with Inverted Resistance . . . 38
3.3 Results on floating zone samples . . . 42
3.4 Defects and Dislocations . . . 45
3.5 Doping and Physical Characteristics . . . 52
3.6 Discussion and Conclusion . . . 54

Chapter 4 Ionic Liquid Gating **56**
4.1 Motivation . . . 56
4.2 Understanding the Parameter Space . . . 58

4.3 Role of Subsurface Cracks 60
4.4 Ionic Liquid Gating 62
4.4.1 Calibration on Copper Wire Electrode 64
4.5 Ionic Liquid Gating on SmB_6 64
4.6 Results and Discussion 66
4.7 Conclusion 69

Chapter 5 Strain Studies **71**
5.1 Introduction 71
5.2 Strain Experiment 73
5.2.1 Piezoelectric-Based Strain Device 73
5.2.2 Experimental Preparation and Challenges 74
5.2.3 Results 77
5.3 Discussion 78
5.4 Conclusion 80

Chapter 6 Conclusion and Outlook **82**
6.1 Summary 82
6.2 Future Work and Open Questions 84
6.2.1 Impurities and Doping 84
6.2.2 Surface Studies 84

Bibliography **86**

List of Figures

1.1 Sketch of cubic structure of SmB_6. Purple spheres are Sm atoms and green spheres are B atoms. 2

1.2 Temperature dependence of SmB_6 as reported by Allen et al. [7] 3

1.3 (a) Sketch of the unhybridized band structure of SmB_6. (b) Sketch of the hybridized band structure of SmB_6. Figure courtesy of A. Mihaliov. 5

1.4 Illustration of band inversion. (a) Trivial insulator with no band inversion. (b) Band inversion of a topological insulator thereby producing a Dirac cone. Figure from Ref. [50] 9

1.5 Surface Brillouin zone of SmB_6. One Dirac cones is expected at the Γ and and two at the X points for the (001) surface, and three Dirac cones are expected at the M points for the (111) surface. Figure from Ref. [55] 10

1.6 Example of ARPES spectrum of the SmB_6 band structure near the Fermi energy. Spectral weight extending upwards through the Fermi energy provides evidence for in-gap states. Figure from Ref. [60] 12

1.7 An STM spectrum of a flux grown SmB_6 sample. Dispersing QPI signals are marked by dashed guides: green (labelled $q1$) and blue ($q2$) lines track surface states, while the red guides track KI states. A box-windowed Fourier transform (FT) (magnified inset in a) enhances the low-q signal (blue) compared with the Hanning-windowed FT that reduces spread of the high-q states in the main panel. Figure from Ref. [74] 14

2.1 Microscope picture of Al flux-grown SmB_6 samples. 23

2.2 Schematics of (a) Hall bar geometry, (b) van der Pauw geometry, (c) standard Corbino disk, and (d) four-terminal Corbino disk. 31

2.3 Schematic of two-sided inverted resistance measurement. (a) Top surface, with a four-terminal Corbino geometry. (b) Side view, showing a standard resistivity measurement. (c) Side view, showing an inverted resistance measurement. (d) Bottom surface, showing a two-terminal Corbino geometry. 33
2.4 (a) An example simulation based on a three voltage contact Hall bar geometry, (b) a plot of the simulated to ideal resistance ratio as a function of contact size, with samples of various thicknesses provided. Figure courtesy of E. Chandler 36

3.1 Example of standard and inverted curve of a stoichiometric Al flux grown sample. 39
3.2 Example of of an indentation after a Vickers microhardness measurement. . . 40
3.3 Inverted resistance measurement of four Al flux grown SmB_6 samples of varying stoichiometry. 41
3.4 Inverted resistance measurement of four floating zone grown SmB_6 samples. . 43
3.5 Bulk resistivity conversion from Fig. 3.4 measurements plotted with the stoichiometric flux grown sample. 45
3.6 Sketch of dislocations in a floating zone boule. Dislocations colored green are those that begin within a slice of thickness ϵ, while those colored blue end within that slice. The remaining grey dislocations may pass through the slice but otherwise begin and end elsewhere. 48
3.7 Examples of etch pits on the (001) surfaces of (a) a floating zone sample etched for 340 seconds and (b) a flux-grown sample etched for 600 seconds. 51
3.8 (a) Resistivity and (b) Hall coefficient on three doped SmB_6 samples. 53

4.1 Constructed parameter space with three fundamental limits and experimental data, following Ref. [88] 58
4.2 (a) The circuit diagram, alongside (b) plotted impedance spectroscopy. . . . 64
4.3 Longitudinal resistance vs. temperature at various voltages applied to the ionic liquid. 66
4.4 (a) Hall coefficient and (b) transverse resistance vs. magnetic field at various voltages applied to the ionic liquid. 67

4.5 Magnetoresistance at various voltages applied to the ionic liquid. 68
4.6 Extracted crack-independent quantity based on Eq. 4.7 with a line of best fit indicating the tunability of carrier density and mobility with gate voltage. . 68
4.7 Ionic liquid result (green line) superimposed on the parameter space shown in Fig. 4.1, showing agreement with QPI Γ pocket results. 69

5.1 Hysteresis and surface conduction persisting up to 240 K as reported in Stern, et al. [135]. 73
5.2 (a) Schematic diagram of a piezoelectric strain device as detailed in Hicks et al.[136], and (b) photograph of the wired setup with mounted SmB_6 sample. 74
5.3 Example of in situ monitoring of strain application as a function of time, showing (a) strain voltage applied, (b) capacitance output, (c)R_{xx} output, and (d) R_{xy} output. 75
5.4 (a) Resistance versus temperature for strain conditions up to 50 V compression and tension, with (b) a zoom of the same data to show response of surface conduction to strain. 78
5.5 Transverse resistance (R_{xy}) versus magnetic field for various strain conditions at 2 K. 79

List of Tables

3.1 Details of the four flux grown samples measured. Samples were grown with a starting composition Sm:B:Al = (1−r):6:700, where r also gives the percentage of Sm vacancies. 40

3.2 Details of the four floating zone samples measured. Sample names indicate growths by collaborators at University of Warwick (Warwick) and Johns Hopkins University (JHU). 44

5.1 Summary of outcomes of each of 11 attempts to perform strain experiments on SmB_6. Sample C is the same sample used for ionic gating in Chapter 4, and Sample E is Sample S1 used in inverted resistance in Fig. 3.3. 77

Abstract

Samarium hexaboride (SmB_6) is a fascinating material of which classification has long generated energized discussion. It is now known to be a strongly correlated mixed valence material in which a small Kondo hybridization gap opens below 100 K. Later studies also identified that a low-temperature conduction feature arises from topologically protected surface sates, making SmB_6 the first topological Kondo insulator. Past experimental results show a striking difference between SmB_6 samples grown by the aluminum flux method and the optical floating zone method that cumulatively shows that the electronic nature of these two samples types are fundamentally different. In this work, it is demonstrated floating zone samples may be compromised by bulk conduction of unknown origin. In contrast, SmB_6 grown stoichiometrically by the aluminum flux method is shown to have a truly insulating bulk, unlike band topological insulators. Doping SmB_6 with vacancies, europium, or lanthanum adds a bulk conduction channel at low temperature, and this feature reproduces a bulk conduction channel in supposedly stoichiometric samples grown by the optical floating zone method. One-dimensional conduction paths through dislocations are proposed as the origin of this conduction channel, and aluminum flux grown samples are found to be preferred due to their low dislocation density. To understand the topological surface conduction channel in aluminum flux grown SmB_6, the carrier density and mobility of the Γ and 2X pockets of the surface Brillouin zone are discussed, and a parameter space for these two quantities is presented. Since transport measurements detect topologically protected conduction on all surfaces, the role of subsurface cracks in transport is discussed, and a crack-independent quantity is presented for analyzing surface transport in a Hall bar. Ionic liquid gating is used to tune the topological surface state, and extracted transport parameters using the crack-independent quantity further restrict the parameter space and are found

to agree with quasiparticle interference results. Finally, uniaxial strain measurements are presented; strain is also able to tune surface conduction in aluminum flux grown SmB_6 but is not found to significantly affect bulk conduction. Material parameters including hardness, brittleness, and elasticity constants are discussed in relation to the challenges in performing the strain experiments. These results yield a picture of SmB_6 as a material unique among both topological insulators and strongly correlated systems.

Chapter 1

Introduction

From the pages of theory papers to the cryostats of laboratories, the study of quantum materials is one of the fastest growing and most exciting areas of research in condensed matter physics. Quantum materials include a large variety of systems with properties that are defined by quantization. Examples of quantum materials include topological insulators (TIs), strongly correlated systems, Dirac semimetals, magnets, and superconductors. It was once thought that these classes existed independently, but further developments have shown that they can exist simultaneously within a material. The interactions between multiple combinations of processes present can produce unique properties.

One material in which this mix of quantum systems occurs is samarium hexaboride (SmB_6), which is both strongly correlated and a TI. The strong correlations arise from the Kondo lattice effect, wherein a band gap forms from the hybridization of f and d electrons. [1, 2] This effect is caused by the formation of Kondo singlets by the coupling of local moments (f electrons on Sm atoms) and conduction electrons (d electrons) at low temperatures. In SmB_6, the Fermi energy lies within the created gap, thus it is a Kondo insulator (in fact, it was the first one to be identified). [3]

In the following section, a historical overview will be used to contextualize current research on this distinctive material. Particular attention will be devoted to recent investigations aimed at clarifying its properties. In some instances, these efforts have led to a reexamination of earlier conclusions.

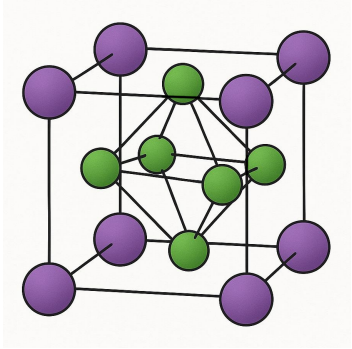

Figure 1.1: Sketch of cubic structure of SmB_6. Purple spheres are Sm atoms and green spheres are B atoms.

1.1 Early Measurements

Samarium hexaboride, SmB_6, belongs to the family of rare-earth hexaborides RB_6 that crystallize in the simple-cubic space group *Pm3m*. The fundamental building block of the lattice is the B_6^{2-} octahedron, whose strong intra-octahedral covalent bonds produce a rigid, nearly incompressible boron framework. [4] These octahedra occupy the cube corners of the unit cell, thereby generating a three-dimensional cage. The rare-earth ion resides at the body center of this boron cage, so the cation sublattice itself is also simple cubic but offset by half a lattice constant. Because the B_6 network is electronically inert over a wide energy window, the valence configuration of the metal ion largely governs whether a given RB_6 compound is metallic or insulating. Compounds that contain a divalent rare-earth ion, such as CaB_6 or EuB_6 under modest pressure, are normally band insulators, whereas trivalent ions, as found in LaB_6 or CeB_6, generally lead to a partially filled conduction band and thus to metallic behavior. Since samarium atoms can be in the divalent and trivalent states, SmB_6 was investigated, but it unexpectedly does not fall on either side of this dichotomy. [5] It behaves like a poor metal at room temperature, exhibits thermally activated transport below about 50 K with an activation energy on the order of 3–5 meV, and unexpectedly develops a resistivity plateau below roughly 4 K in high-purity single crystals. [6, 7, 8]

Early interpretations drew on standard semiconductor physics. The thermally activated increase in resistivity was attributed to carrier freeze-out, and the low-temperature plateau was ascribed to impurity bands situated within the gap. However, several experimental ob-

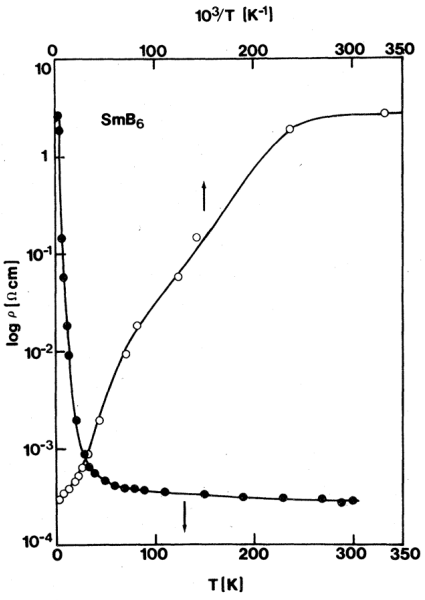

Figure 1.2: Temperature dependence of SmB_6 as reported by Allen et al. [7]

servations challenged that view. First, the measured bulk impurity concentration was far too small to account for the magnitude of the residual conductivity. Second, the Hall coefficient R_H underwent a sign reversal: it was negative (electron-like) below around 65 K but positive (hole-like) at higher temperatures. [7] Models that invoked two independent conduction channels or a temperature-dependent mobility ratio could reproduce the sign change only by adopting unrealistic parameter values. These resistivity and Hall anomalies signaled that the electronic ground state of SmB_6 could not be understood within the conventional framework of a lightly doped narrow-gap semiconductor.

1.1.1 Magnetic Anomalies and Van Vleck Susceptibility

Magnetometry supplied an additional set of puzzles. Over a broad temperature window, the magnetic susceptibility χ(T) of SmB6 obeys a Curie–Weiss form with an effective moment close to that of a free Sm^{3+} ion ($J = 5/2$), hinting at the presence of localized f moments. [9, 6, 10] Yet χ(T) deviates systematically from Curie behavior both above about 150 K and below about 40 K. At elevated temperature the deviation is upward, consistent with a sizable Van Vleck contribution common among $4f$ ions where the spin–orbit interaction is strong and the crystal-field splitting is comparatively weak. At lower temperatures, χ(T) falls below

the Curie law and eventually levels off, suggesting the emergence of a spin gap. Early workers tried to model this downturn solely through a Van Vleck term, [6] but subsequent analyses showed that an Arrhenius factor, $\exp(-\Delta_s/k_BT)$, where $\Delta_s \approx 5$ meV, is required. [11, 12] The low-temperature susceptibility can therefore be viewed as a superposition of three elements: a Curie–Weiss component from partially screened $4f$ moments, a temperature-independent Van Vleck background, and an activated contribution that indicates gap formation.

1.1.2 Spectroscopic Evidence for Mixed Valence

The notion that SmB_6 possesses an unusual valence state emerged from two complementary spectroscopic techniques: X-ray absorption spectroscopy (XAS) at the L edges of samarium, and Mössbauer spectroscopy. In the early 1970s, XAS revealed a double-peaked structure in the absorption coefficient. One peak matched the energy expected for a Sm^{2+} ($4f^6$) final state and the other corresponded to a Sm^{3+} ($4f^5$) final state, prompting the interpretation that the crystal comprised a physical mixture of divalent and trivalent ions. [13, 14] Mössbauer measurements soon complicated that picture. The isomer shift of the ^{149}Sm resonance, which is sensitive to the s-electron density at the nucleus and therefore to the nominal valence, lay midway between the shifts characteristic of purely divalent and purely trivalent Sm compounds. [15] Crucially, the hyperfine spectrum did not exhibit two distinct lines but a single broadened line, implying that every samarium site experienced the same time-averaged electronic environment. [16] The simplest way to reconcile these facts is to invoke homogeneous mixed valence: each Sm ion fluctuates rapidly between the $4f^6$ and $4f^5$ configurations, producing a non-integer average valence n ≈ 2.6 over timescales longer than 10^{-8} s.

1.1.3 Mixed-Valence Phenomenology and Chemical Tuning

Mixed-valence (MV) compounds may be grouped into two broad categories. Inhomogeneous MV materials, such as many transition-metal oxides, contain spatially distinct sites that are locked into different integer valences. In contrast, homogeneous MV systems exhibit quantum mechanical admixture of electronic configurations on every lattice site. A key

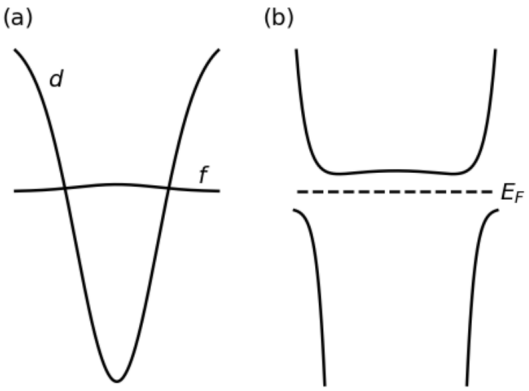

Figure 1.3: (a) Sketch of the unhybridized band structure of SmB_6. (b) Sketch of the hybridized band structure of SmB_6. Figure courtesy of A. Mihaliov.

requirement for homogeneous MV behavior is near-degeneracy between a localized f (or d) level and an itinerant *spd* band at the Fermi energy, permitting charge fluctuations. [17] The rare-earth elements, owing to their localized $4f$ shells and variable oxidation states, furnish several canonical MV examples besides SmB_6, among them SmS under pressure, TmSe, and $YbInCu_4$. [18, 19, 20, 17]

Chemical substitution allows systematic manipulation of the mean Sm valence in SmB_6. Replacing samarium with a trivalent ion such as La^{3+} injects extra electrons, shifting the average valence toward 2+. [21] Conversely, introduction of divalent dopants like Eu^{2+} or the creation of Sm vacancies removes electrons and drives the system toward the 3+ limit. Valence changes induced in this fashion correlate smoothly with shifts in transport gaps, magnetic responses, and lattice constants, reinforcing the picture of a rigid yet tunable hybridized electronic structure. [22, 23, 21] Hydrostatic pressure provides another tuning parameter but its effect on SmB_6 is surprisingly muted: diffraction and XAS up to 150 kbar show that the samarium valence remains intermediate rather than collapsing to 3+. This is in stark contrast to SmS, which undergoes an abrupt black-gold transition from Sm^{2+} to Sm^{3+} at only 6 kbar. [24, 25]

1.1.4 Hybridization, the Kondo Lattice, and Gap Formation

The unusual coexistence of local-moment features with a small charge gap led theorists to propose that SmB6 is a Kondo insulator, [3] a subset of the broader family of heavy-fermion materials. In the Kondo lattice model, local f moments pair with conduction electrons (here primarily derived from Sm $5d$ electrons) to form a Kondo singlet below a characteristic coherence temperature T_K. [1, 2] This pairing opens a small gap. In the case of SmB_6, the Fermi level resides inside that gap and becomes a narrow-gap insulator at low temperature.

Multiple experimental probes support the Kondo insulator scenario in SmB6. Angle-integrated photoemission spectroscopy shows a transfer of spectral weight away from the Fermi level as the sample is cooled below approximately 100 K, consistent with gap opening. [14, 26, 27] Angle-resolved photoemission spectroscopy (ARPES) observes the emergence of a hybridization gap of roughly 15 meV at the X point of the Brillouin zone and detects flat $4f$-derived bands hybridizing with dispersive conduction bands. [28] Optical conductivity, measured via infrared reflectivity, reveals a suppression of low-energy spectral weight and the appearance of a mid-infrared peak that scales with the hybridization energy, while inelastic neutron scattering identifies dispersive magnetic excitons whose minimum lies near 14 meV, the same energy scale inferred from optics. [29]

Pressure experiments add a complementary perspective. Early four-probe resistivity studies reported a pressure driven metal–insulator transition between 40 and 80 kbar. [24, 30, 31] Subsequent measurements that combined transport, synchrotron X-ray diffraction, and resonant inelastic X-ray scattering clarified that the transition does not originate from a structural phase change nor from a collapse of the intermediate valence. Instead, the gap closes because hybridization is weakened under compression. [24] At still higher pressure the material enters an antiferromagnetic state, as evidenced by both neutron diffraction and muon spin rotation. [32] The competition between Kondo screening (favoring singlet formation and an insulating gap) and the Ruderman–Kittel–Kasuya–Yosida (RKKY) interaction (driving magnetic order) therefore seems to control the phase diagram of SmB_6. [33]

In a canonical Kondo insulator the charge gap deduced from activation of the electrical resistivity and the spin gap extracted from the downturn in magnetic susceptibility should

be of comparable magnitude, because both originate from the same hybridization process. [12] SmB_6 obeys this relation rather well: transport, optical, and tunneling spectroscopy report a gap of 15–20 meV, whereas the spin gap inferred from susceptibility and specific heat data is about 15 meV, lending additional weight to the Kondo insulator designation. However, while Kondo physics explains bulk properties, it does not in itself account for the robust residual conductivity observed in transport and magnetoresistance at temperatures below 4 K.

1.1.5 Magnetotransport: Anomalous Negative Magnetoresistance

Magnetoresistance measurements present an intriguing puzzle. At temperatures between roughly 10 K and 100 K, the longitudinal resistivity ρ_{xx} decreases upon application of a magnetic field, demonstrating negative magnetoresistance [34, 35, 36, 37] that is qualitatively consistent with Zeeman suppression of a Kondo or hybridization gap. One would expect this behavior to reverse or vanish once the system becomes metallic below 4 K, yet experiments down to millikelvin temperatures show that the negative magnetoresistance persists and sometimes even strengthens below the resistivity plateau. Early explanations invoked donor- or acceptor-type impurities that would form bound magnetic polarons, [35, 38] but careful correlation with impurity concentrations and with luminous optical centers failed to substantiate that mechanism. An alternative picture attributes the low-temperature conduction to a metallic surface state whose carrier density and mobility are field dependent. Despite these advancements, quantitative understanding remains incomplete, and magnetoresistance in SmB_6 continues to stimulate debate. [39]

1.2 Topological Insulators

Topology as a mathematical discipline comprises classification of objects based on their shape. If an object can be deformed into another object without introducing or closing up a hole, the two objects are topologically identical. Geometrically, this can be illustrated by a doughnut and a coffee mug. Both contain one hole, so they are topologically equivalent to each other, but they are not equivalent to a sphere, which has no holes. The topology of an

object can be represented by an integer – in the doughnut example, this integer would be the number of holes the object has. Two objects described by the same integer, or topological index, are considered to be topologically equivalent.

More abstractly, solids can also be classified by their topology via an integer or set of integers. In 1980, the integer quantum Hall effect (IQHE) was observed in a two-dimensional electron gas (2DEG). [40] When a magnetic field is applied, the Hall conductivity becomes quantized and the electrons in the bulk of the 2DEG undergo circular motion. However, near the edges of the piece, the electrons cannot form full orbits. Instead, they follow a semicircular path and "bounce" off the edges, creating a chiral edge state where the electrons travel in only one direction. Later work classified this chiral edge state as topological, [41] arising from the breaking of time reversal symmetry (TRS) when the magnetic field is applied.

TRS breaking is fundamental to the topological insulator. In the IQHE, the external field provides the TRS breaking, but later work showed that TRS breaking does not have to be external. In the quantum spin Hall (QSH) insulator, two spin-polarized integer quantum Hall systems are combined, to create chiral edge states with opposite spin polarization. The two edge states form a time reversed pair, allowing the system to be topological even when the magnetic field is not present. The original proposal for a QSH system was in graphene with spin-orbit coupling. [42] The spin-orbit coupling in graphene allowed for spin polarization in the edge states; in modern topological studies, this is known as spin-momentum locking. In the QSH model, the topological index that arises is the Z_2 index. [43] The Z_2 index represents the number of times the chiral edge states cross the Fermi level, which shows that information about topology can be contained within the band structure. This QSH phase was eventually realized in HgTe/CdTe quantum wells. [44, 45]

While both the IQHE and the QSH are based on 2D systems, the idea of TRS breaking and spin-momentum locked edge states were soon extended to three dimensions. [46, 47] In three-dimensional TIs, spin-momentum-locked surface states are present, and the surface states arise from the inversion of the valence and conduction bands in materials with strong spin-orbit coupling. When band inversion driven by spin–orbit coupling or hybridization is present, these effects can cause time reversal invariant momenta to switch. If an odd number of these momenta exist, the insulator becomes non-trivial and a metallic surface

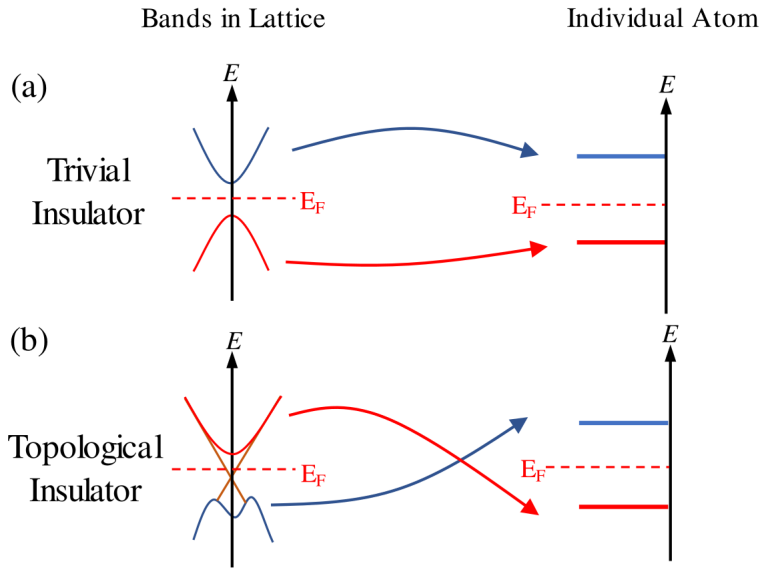

Figure 1.4: Illustration of band inversion. (a) Trivial insulator with no band inversion. (b) Band inversion of a topological insulator thereby producing a Dirac cone. Figure from Ref. [50]

state must bridge the bulk gap. The surface state is known as a Dirac point or Dirac cone, and to be topologically non-trivial, there must be an odd number of Dirac points in the gap. These Dirac points must also exist in the Brillouin zone of all crystal surfaces. [48] The number of Dirac points in the gap is related to the Z_2 topological index, as in the 2D systems. Electronically, the surface states comprising the Dirac points cross the gap and are therefore conductive while leaving an insulating bulk. The first 3D TIs experimentally identified TI were all bismuth-based: $Bi_{1-x}Sb_x$, Bi_2Se_3, and Bi_2Te_3. citehasan These were identified by using angle-resolved photoemission spectroscopy (ARPES) to directly map the band structure and reveal the presence and number of Dirac cones. [49]

1.3 Revisiting SmB_6 as a Topological Kondo Insulator

1.3.1 Theoretical Prediction

The first 3D TIs were band insulators, but later work proposed that Kondo insulators could also host topologically protected states. [51, 52, 53] The hybridization between f electrons and the conduction sea opens the gap and forms distinct valence and conduction bands. The

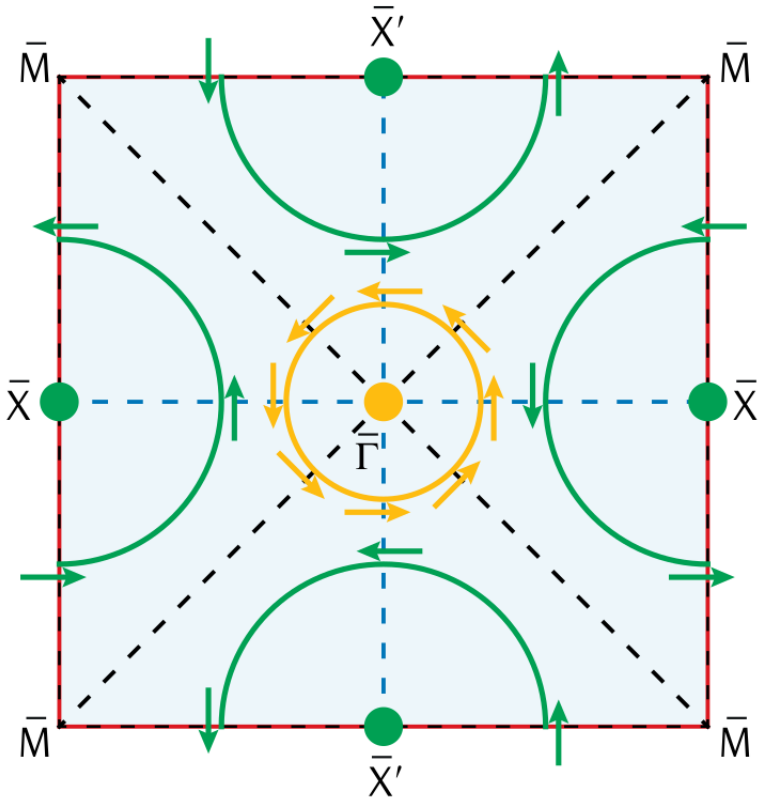

Figure 1.5: Surface Brillouin zone of SmB_6. One Dirac cones is expected at the Γ and and two at the X points for the (001) surface, and three Dirac cones are expected at the M points for the (111) surface. Figure from Ref. [55]

strong spin orbit coupling that leads to hybridization also allows for a TI to form. SmB_6 was predicted to have time reversal symmetry breaking, and its inverted band structure would lead to a topologically protected surface state in the Kondo hybridization gap. For the (001) surface Brillouin zone, one Dirac cone at the Γ point and two equivalent Dirac cones at the X points were predicted, while the (111) surface would host three cones at the M points. [54] A sketch of the surface Brillouin zone of SmB_6 with high symmetry points labeled is shown in Fig. 1.5. [55]

Because the bulk gap in SmB6 arises from f–d hybridization rather than from s–p inversion, the TKI concept broadens the landscape of topological phases to include strongly correlated electron systems. The proposal that SmB_6 could be a topological insulator – that is, an insulator with protected metallic states bridging the gap – is the current picture used to resolve some of the unexpected experimental results observed in SmB_6.

1.3.2 Electrical Transport

The earliest experimental tests of topological protection in SmB_6 exploited the defining characteristic of a topological insulator: a fully insulating bulk coexisting with metallic surfaces. [56, 57, 58] As the temperature drops below approximately 4 K, the bulk of SmB_6 becomes increasingly resistive owing to the opening of the Kondo hybridization gap, while the resistivity saturates instead of diverging to infinity. This resistivity plateau suggested that a parallel conduction channel survives. To distinguish surface from bulk contributions, researchers employed multiple-lead configurations in which current and voltage contacts were placed on opposite sample faces. [56] By comparing longitudinal resistances measured in various geometries, they established that current flows predominantly along the exterior below the crossover temperature, thereby confirming surface-dominated conduction.

A complementary thickness-dependent Hall experiment provided additional evidence. The Hall coefficient of a purely three-dimensional conductor scales inversely with sample thickness, whereas a two-dimensional conductor exhibits thickness-independent Hall response. By fabricating wedge-shaped specimens and mapping the Hall coefficient at different local thicknesses, the investigators found that, below 4 K, the Hall coefficient was identical regardless of thickness. [57] In parallel, researchers observed that the temperature at which the resistivity plateau emerges is higher for thinner samples, consistent with the idea that the bulk contribution is progressively suppressed as the surface-to-volume ratio increases. [58]

While transport measurements thus demonstrate robust surface conduction, the question of whether that surface is topologically protected remains unsettled. One magnetotransport study reported spin-momentum locking signals, inferred from the circular polarisation of emitted terahertz radiation under pulsed current drive, yet independent groups have not reproduced these signatures. [59] As a result, researchers have turned to additional probes to further scrutinize the possible topological character.

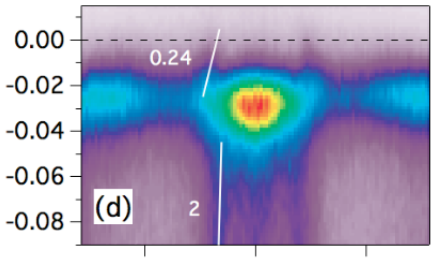

Figure 1.6: Example of ARPES spectrum of the SmB_6 band structure near the Fermi energy. Spectral weight extending upwards through the Fermi energy provides evidence for in-gap states. Figure from Ref. [60]

1.3.3 Spectroscopy

Angle-resolved photoemission spectroscopy (ARPES) has become a central technique for revealing the momentum-resolved electronic structure of candidate topological insulators because it can visualize Dirac cones and associated spin textures. For well-studied band topological insulators such as Bi_2Se_3, the inverted bulk gap is on the order of several hundred meV to a few eV, which places the Dirac point far from the Fermi level and permits straightforward measurements with conventional photon energies. By contrast, the hybridization gap of the Kondo insulator SmB_6 is roughly two orders of magnitude smaller, complicating the extraction of a reliable band picture from photoemission data. Additionally, although the IQHE and early quantum systems were probed using transport, band TIs, while insulating in theory, often host degenerate bulk conduction through defects and impurities. ARPES could then reveal the Dirac cones in the band structure where transport is more difficult to perform.

Most ARPES studies on SmB_6 have targeted the (001) surface, where theory predicts topologically protected surface bands centered at the Γ and X points of the two-dimensional Brillouin zone. [54] These campaigns have attempted to catalog weak in-gap features distinguishable from the bulk $5d$–$4f$ hybridization bands. Initial measurements reported Dirac-like crossings at Γ as well as at the two symmetry-related X points. [61] An example of an ARPES spectrum near the Fermi energy is shown in Fig. 1.6. In combination with circular dichroism, these observations were interpreted as evidence for spin-momentum locking, lending credence to a nontrivial topological classification. [62, 63] Subsequent studies, however, challenged

this narrative. Several groups identified three metallic states yet attributed them to trivial origins such as surface-induced band bending, [64] dangling boron bonds that arise upon cleavage, [65] Rashba-type splitting, [66] or even surface-confined many-body resonances of the $4f$ manifold. [67] Others failed to detect a clear Γ-point Dirac cone, observing only electron-like pockets near the X points without the requisite odd-number count of surface bands expected for a strong Z_2 topological insulator. [60, 68, 69]

Part of the controversy may originate from the intricate surface morphology produced when SmB_6 single crystals are cleaved under ultra-high vacuum for ARPES measurements. Scanning tunneling microscopy (STM) routinely reveals a patchwork of micron-scale terraces that include two families of polar unreconstructed surfaces terminated solely by either samarium or boron and a third nonpolar (2×1) reconstruction comprising alternating Sm and B rows. [70, 71, 72] Polar terminations possess excess surface charge that induces local electrostatic potential gradients, which in turn shift surface states in energy through band bending. Scanning tunneling spectroscopy (STS) confirms that the energy position of near-gap spectral features depends sensitively on whether the probe sits atop Sm-rich, B-rich, or mixed terminations. Since typical ARPES spot sizes span tens of micrometres, a single measurement averages over many nanoscale domains with distinct potentials, which can distort dispersions. [67, 73] Consequently, Dirac crossings may be blurred beyond recognition, or trivial states may inadvertently masquerade as topological ones.

A promising strategy to mitigate polarity issues involves cleaving along the (111) plane, which is nonpolar by symmetry. An ARPES study performed on freshly cleaved (111) facets revealed three symmetry-equivalent M-point pockets whose spin polarization was consistent with helical surface states. [75] Despite the clarity of this observation, it has not received equal attention because most experimental and theoretical efforts remain focused on the (001) orientation. Given the absence of polarity-induced band bending and the higher surface symmetry of the (111) face, future work emphasizing this geometry may be decisive in settling debates about the existence of nontrivial surface states in SmB_6.

Complementary insights have come from quasiparticle interference (QPI) imaging with STM/STS. In a prototypical topological material, elastic scattering that reverses momentum without flipping spin is suppressed, leading to characteristic suppression of backscattering

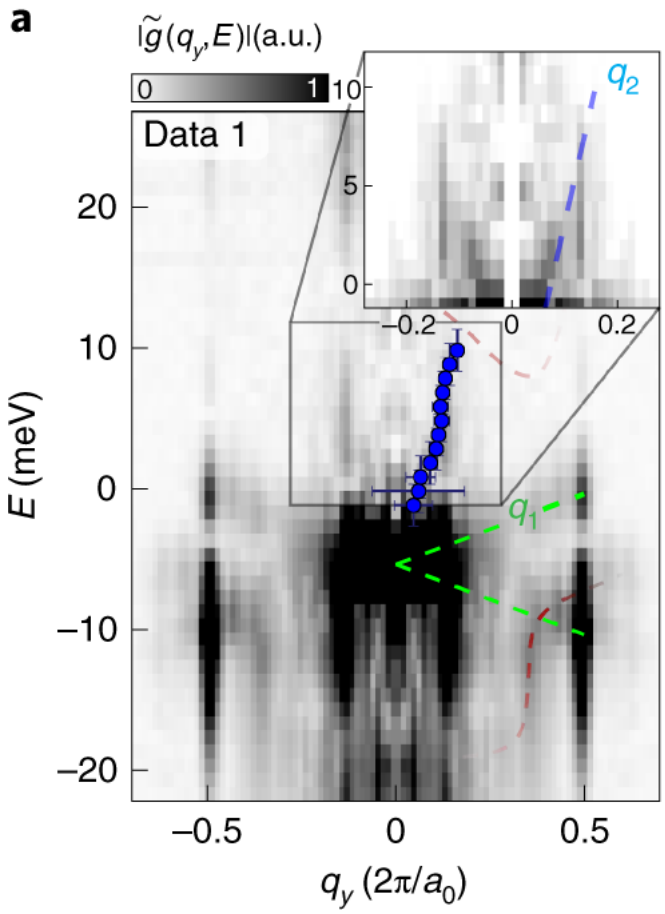

Figure 1.7: An STM spectrum of a flux grown SmB_6 sample. Dispersing QPI signals are marked by dashed guides: green (labelled $q1$) and blue ($q2$) lines track surface states, while the red guides track KI states. A box-windowed Fourier transform (FT) (magnified inset in a) enhances the low-q signal (blue) compared with the Hanning-windowed FT that reduces spread of the high-q states in the main panel. Figure from Ref. [74]

wave-vectors in Fourier-transformed conductance maps. A single report [74] has presented QPI data on SmB_6 indicating such suppression and has extracted three Dirac cones at Γ and the two X points. Nevertheless, the extracted Fermi velocities and spin orientations differ from those obtained by ARPES, again underscoring the tensions between surface-sensitive probes.

1.3.4 Magnetotransport

In systems that preserve time-reversal symmetry and exhibit strong spin-orbit coupling, weak anti-localization (WAL) arises from destructive quantum interference between time-reversed scattering trajectories. The suppression of backscattering enhances the conductivity near zero magnetic field. Applying a perpendicular field breaks time-reversal symmetry and quenches this interference, producing a conductance minimum or, equivalently, a resistance maximum at small fields. The high-field magnetoresistance then decreases as the field further increases. Quantitatively, the Hikami–Larkin–Nagaoka (HLN) formula captures this behavior through a dephasing length and a prefactor α, where each independent spin-helical surface channel contributes 0.5 to α. For SmB_6, with two spin states on each of three predicted Dirac cones, one expects $\alpha \approx 3$ if all channels contribute equally.

Experimental attempts to observe WAL in SmB_6 have yielded inconsistent outcomes. Three groups employing standard Hall-bar devices have reported resistance upturns near zero field that fit the HLN expression, yet the extracted prefactors vary widely, often deviating by an order of magnitude from the theoretical value. [76, 77, 36] Furthermore, WAL-like features occasionally appear even for magnetic fields nominally aligned along the direction of the current, where surface states on the Hall bar should experience negligible perpendicular field. [36] Such anomalies might arise because the Hall bar geometry allows current to traverse all faces of a rectangular crystal. When the external field is oriented in-plane for the four longer surfaces, it is perpendicular to the end surfaces, potentially giving rise to WAL contributions from those faces.

A Corbino geometry, in which a circular current path confines transport to a single surface and is insensitive to carrier sign, was adopted in a subsequent study to minimize such ambiguities. Although a peak in resistance near zero field was again recorded, its

magnitude turned out to depend strongly on the magnetic-field sweep rate. [37] Genuine WAL is an intrinsic quantum interference phenomenon and should not display sweep-rate dependence. The authors therefore attributed their observations to extrinsic effects, perhaps related to slow magnetization dynamics in a surface oxide or to trapping and release of carriers by defects.

Negative magnetoresistance, rather than WAL, has also been invoked as evidence for a crossover to surface conduction. The bulk resistivity of SmB_6 diminishes dramatically when a moderate magnetic field is applied, reaching a maximum negative value near 5 K. Some researchers interpret the shift of this maximum as an indication that the bulk-to-surface conduction ratio changes with temperature and field. [38, 78, 79] In addition, angle-dependent magnetoresistance has revealed evolution from fourfold symmetry above 5 K, consistent with cubic bulk transport, to twofold symmetry at lower temperatures. [78] The emergence of twofold symmetry is naturally explained if the surface states on the four side faces are not all equivalent or if the current is increasingly confined to one dominant facet.

1.4 Unresolved Questions for SmB_6

1.4.1 Dependence of Results on Experimental Method

A striking aspect of the SmB_6 literature is the degree to which data sets can be categorized by the type of measurement. One major source of disagreement is due to the crystal growth method. Two principal growth methods dominate: aluminum flux growth and optical floating-zone growth. Flux growth involves combining stoichiometric amounts of samarium and boron with an excess of molten aluminum at temperatures well below the melting point of SmB_6. The aluminum serves both as a solvent and as a protective medium that minimizes samarium volatilization, thereby aiding in the preservation of stoichiometry. The resulting single crystals typically measure a few millimeters across and may incorporate isolated pockets of residual aluminum that are difficult to eliminate. [80] Floating-zone growth, in contrast, employs an optical image furnace to melt a feed rod of stoichiometric SmB_6 with-

out crucible contamination. The molten zone is translated along the rod, solidifying into a large centimetre-scale crystal. [81] The higher processing temperature, however, introduces the risk of thermal stress, samarium evaporation, and a correspondingly greater density of vacancies and defects.

Standard bulk characterization techniques reveal no dramatic compositional differences between the two crystal types. [82, 81] Nonetheless, a consistent pattern emerges when one enumerates which samples underpin specific claims. ARPES studies reporting trivial surface states preferentially utilize floating-zone crystals, [66] whereas those presenting topological surface dispersions more commonly employ flux grown samples. [62, 63] In the quantum oscillation arena, the two-dimensional oscillations attributed to surface states originate from flux crystals, [83, 84] while the three-dimensional Fermi surfaces are reported exclusively on floating-zone material. [85, 86, 87] Thermal transport also follows this dichotomy, with flux-grown specimens exhibiting negligible residual heat conductivity, in contrast to the variable behavior documented for floating-zone counterparts. Even in electrical transport, the shape of the resistance plateau below 4 K differs between flux-grown and floating zone grown samples. In flux-grown samples, the plateau is usually a true horizontal plateau, while in floating zone grown samples, the plateau nearly always still displays activated behavior. [87]

Even within measurements on the same sample type, there is very little agreement among experimental methods. For example, transport results all taken from flux-grown samples will often find very different values for the resistivity plateau below 4 K. Estimates of the carrier density derived from transport and other methods like ARPES also disagree. Previous work attempted to reconcile predictions with these disparate experimental results by creating a parameter space of carrier density and mobility based on theoretical calculations of the Γ and X pockets. Then, experimental values from a variety of studies were plotted together to quantify the disagreement. [88], and new results on flux-grown samples will be presented later in this work. However, more systematic cross-comparisons, ideally incorporating identical measurement protocols on well-characterized crystals from both growth techniques, are essential for disentangling these possibilities. In Chapter 3, a comparison of flux and floating zone grown samples will be presented, and their bulk conduction analyzed.

1.4.2 Impurities

Impurities occupy a central place in the historical and contemporary discourse on SmB_6. In the 1970s the low-temperature conductivity plateau was initially linked to impurity bands, [7] an explanation that eventually fell out of favor once the Kondo insulating mechanism was established. In the modern era, impurities have reemerged as potential culprits in the diverse phenomena that complicate the interpretation of experimental data.

The most prevalent form of chemical disorder arises from residual rare-earth contaminants, mainly gadolinium, that are notoriously difficult to remove from samarium during purification. Mechanical stresses during growth or post-growth cooling can further introduce point defects, dislocations, or strain-induced phases. Isotopic purification to ^{154}Sm, followed by zone refining, reduces but does not fully eliminate such contaminants. [89]

Magnetic impurities carry special significance because they can locally break time-reversal symmetry. In a topological insulator, their presence would introduce backscattering and possibly open a gap in the surface Dirac cone. Within the Kondo picture, magnetic impurities can act as localized moments that are screened by conduction electrons, thereby perturbing the coherence of the hybridized bands. One experimental program introduced sub-percent levels of Gd into SmB_6 and observed that even minimal concentrations depress the Kondo coherence temperature and broaden the hybridization gap. [90] Another study proposed that partially screened Gd moments generate oscillatory magnetization as a function of field, potentially explaining quantum oscillations without invoking a genuine Fermi surface. [91]

Nonmagnetic impurities, including samarium vacancies and nonmagnetic rare-earth dopants, are equally consequential. Systematic transport studies indicate that less than one half percent substitution of yttrium suppresses the surface conduction channel, consistent with a sensitivity of the Kondo lattice to disorder. [92] A recent investigation of samarium-deficient SmB_6 found that vacancies increase the residual resistivity by an order of magnitude, consistent with enhanced elastic scattering. [93] Surprisingly, angle-integrated photoemission and bulk specific heat reported that the hybridization gap magnitude remains largely intact, suggesting that the gap is robust against certain types of disorder even though transport

channels are strongly disrupted.

A theoretical perspective posits that nonmagnetic point defects can create mid-gap resonant states characteristic of Kondo insulators, leading to percolating metallic pathways. Numerical calculations support the idea that short-range disorder may tip SmB_6 toward a nodal semimetallic phase, in which conduction and valence bands overlap at isolated points. [94, 95] Under such conditions, quantum oscillations reminiscent of those in metals could emerge. Competing theories invoke excitonic condensates, disorder-assisted Kondo breakdown, and even unconventional Majorana fermion bands that appear below the gap.[92]

1.4.3 Quantum oscillations

Magnetic quantum oscillations, whose canonical examples are the de Haas–van Alphen effect in magnetization and the Shubnikov–de Haas effect in resistivity, provide a sensitive probe of Fermi-surface geometry. In an insulator, quantum oscillations would normally be absent, yet multiple groups have observed dHvA oscillations in SmB_6 at high magnetic fields. The findings, however, diverge dramatically regarding both the dimensionality of the underlying Fermi surface and the effective masses extracted. This puzzle is one of the major sources for ongoing debate about SmB_6.

One study investigated Al-flux-grown crystals and detected three prominent oscillation frequencies. Two of these frequencies evolved with field angle exactly as would be expected if their origin were cylindrical Fermi surfaces projected from the X points of the bulk Brillouin zone onto different crystallographic faces. The third frequency was weaker and attributed to the Γ center. Crucially, the angular dependence was essentially two-dimensional: the cross-sectional area scaled with the cosine of the angle between the applied field and the surface normal, as anticipated for surface states. Nevertheless, the cyclotron effective masses for the surface states derived from the temperature dependence of the oscillation amplitude were surprisingly small, conflicting with ARPES measurements of heavier quasiparticles. [83, 96]

By contrast, a study of optical floating-zone crystals reported oscillations with substantially higher frequencies that varied smoothly with field orientation, more consistent with a three-dimensional ellipsoidal Fermi surface reminiscent of related metallic hexaborides. That group proposed that neutral quasiparticles, decoupled from the charge sector yet still

carrying spin, occupy a bulk Fermi surface and give rise to the observed oscillations, despite SmB_6 being an insulator. In later work, they argued that these neutral excitations could be understood within a theoretical framework that allows for the breaking of gauge symmetry in a Majorana-like band or within models in which the hybridization gap collapses in sufficiently strong fields. [84, 85]

The stark disagreement has sparked a wide range of experimental and theoretical efforts aimed at identifying either intrinsic mechanisms that permit oscillations in a gapped Kondo system or extrinsic artifacts that could mimic such signals. Thermal conductivity measurements represent one avenue of attack: if neutral fermions are present, they should transport heat even when charge transport is frozen. [85] Experiments on flux grown crystals have generally failed to detect a residual linear term in the low-temperature thermal conductivity, whereas some studies of floating-zone specimens report a finite intercept, supporting the neutral quasiparticle hypothesis. [86] An additional puzzle is the anomalous excess specific heat that persists in SmB_6 below roughly 4 K. Several groups attribute this excess to localized magnetic impurities or in-gap resonant states, yet others argue it could be evidence for a neutral Fermi surface. [97]

Not all investigators are persuaded that the oscillations are intrinsic. Careful microstructural analysis has revealed micron-scale inclusions of elemental aluminum in flux grown single crystals. When such inclusions are dissolved by selective etching, the dHvA signal often disappears, suggesting that metallic inclusions rather than SmB_6 itself might generate oscillatory magnetization. [98] On the other hand, in floating-zone crystals, aluminum contamination is absent, yet oscillations are still observed at higher frequencies. Rare-earth impurities are another suspect; [99] however, systematic magnetization data indicate that dilute concentrations of magnetic ions alone cannot account for the amplitude and frequency of the observed oscillations.

The absence of Shubnikov–de Haas oscillations up to magnetic fields approaching 80 T remains a perplexing feature. [100] SdH oscillations typically emerge at fields similar to those required for dHvA oscillations in conventional metals. One suggestion is that surface states, if they dominate electrical conduction, may possess short quantum lifetimes because of scattering from step edges or adatoms, thereby suppressing SdH even while allowing the

thermodynamic dHvA signal to persist. Alternatively, if neutral quasiparticles give rise to the magnetization oscillations, they would not couple to charge transport and therefore would not manifest in resistivity.

Chapter 2

Methods and Techniques

2.1 Growth Methods

The two primary ways in which SmB_6 samples are grown are the aluminum flux method or the optical floating zone method, both of which rely on processes that use the samarium-boron phase diagram in order to control the final product. [101] The aluminum flux method produces millimeter-sized crystals and relies on crystallizing SmB_6 within a solution of liquid aluminum. [80] The optical floating zone method produces significantly larger crystals of up to 10 centimeters long and relies on melting a packed rod of Sm and B together in an optical furnace. [102]

2.1.1 Flux Growth

Flux growth uses a stoichiometric mixture of the desired crystal dissolved into a solvent called flux, which is typically a molten metal or oxide. In the case of SmB_6, the flux used is almost always aluminum. In typical processes where high purity is required and there are concerns of contamination from the air, a quartz ampuole may be utilized to isolate the stoichiometric mixture. However, SmB_6 formation requires a higher temperature than can be used for a sealed quartz ampoule [80] and thus a ceramic crucible, capable of withstanding high temperatures, under an inert gas, typically argon, is used. [103]

To grow SmB_6 by the Al-flux method, powders of samarium and boron are mixed with

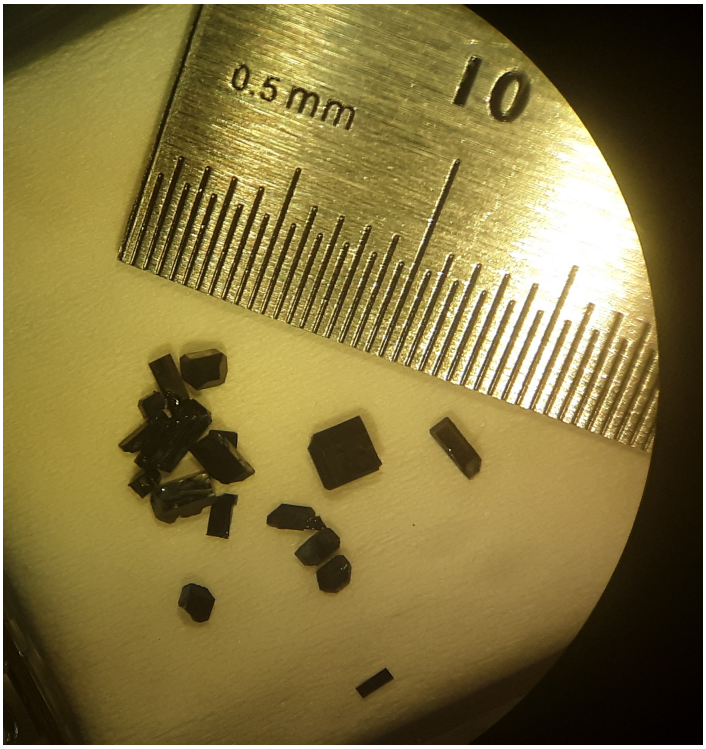

Figure 2.1: Microscope picture of Al flux-grown SmB_6 samples.

aluminum pellets in a crucible, heated to approximately 1600°C, and stirred until the solids fully dissolve in the now molten flux. The mixture is then cooled back to room temperature at a slow and carefully controlled rate, to ensure that the growth of the SmB_6 crystals is done at thermodynamic equilibrium, thereby leading to high and consistent crystal quality with reduced defects or inclusions. This cooling may take place over the course of several hours up to two weeks. [104, 105] Once cooled, the residual aluminum is dissolved with a strong acid or base, typically sodium hydroxide, revealing needle- or plate-shaped crystals, each a few millimeters in size. [80] A photograph of some flux-grown samples are shown in Fig. 2.1.

Despite the consistency and quality of the SmB_6 crystals produced by the Al-flux method, there remain a few shortcomings, the chief limitation being the unintentional trapping of flux within the crystals during formation. Almost every SmB_6 sample contains epitaxial aluminum pockets whose morphology mimics the external habit of the crystals, i.e needle-shaped inclusions in needle crystals and plate-shaped inclusions in plate crystals. The mirrored, epitaxial aluminum reflects the matching lattice parameter between Al and SmB_6 at aluminum's

melting point. [81] Some studies have proposed Sm_3Al_{11} as an additional inclusion, but its lattice parameter and structure differ markedly from those of SmB_6 and its presence in samples has not yet been identified. [80, 106] Other occasional defects include voids (often tied to off-stoichiometric melts) and twinned or polycrystalline regions that arise when separate seeds merge or when the flux is intentionally doped with other rare-earth elements.

2.1.2 Floating Zone Growth

Optical floating zone growth of SmB_6 is carried out at its 2,500°C melting point. Powders of Sm and B are first pressed into a "feed rod" which is mounted above a small SmB_6 seed crystal inside a four-mirror furnace illuminated by focused halogen or xenon arc lamps. As the seed end is brought to the melt temperature, the rod is slowly lowered so the molten zone travels upward; the descending melt solidifies below the zone, building a single crystal from the seed. As in aluminum flux growth, the entire process is conducted under an inert argon atmosphere to limit contamination from the air. [102]

Crystal quality in floating zone growth depends on the translation of the feed rod through the molten zone and the rotation parameters of the feed rod. Slower passing rates minimize polycrystallinity, twin crystals, and cracking, while counter-rotating the rod and grown crystal promotes compositional uniformity in the molten zone. [107] Re-melting the crystal in second or third passes can further improve crystal quality, but extended time at 2,500°C exacerbates Sm loss by evaporation, often as elemental Sm or SmB_4. Thus, SmB_6 growers typically compensate for this by starting with a Sm excess. However, even with these precautions, property gradients remain; the lattice parameter has been found to contract with distance from the seed, signaling a rising density of Sm vacancies and dislocations along the sample. [81] Furthermore, another quality consideration is in radial phase or property segregation, wherein the center of the rod is one phase (or has one material characteristic value) while an outer portion is another phase (or has a differing material characteristic value). The floating zone growth method was initially developed for the formation of single element materials, and thus nominally minor variation in the temperature between the center and outer cross-sectional portions of the boule was of lesser concern; however, with two-element materials, variations must be considered.

Despite the concerns of quality and consistency, floating zone crystals have been preferred over flux grown crystals in several fields where large sample surface areas are required and flux grown crystals do not reach a desired area threshold, such as neutron scattering or terahertz spectroscopy. Similarly, while floating zone grown SmB_6 samples used in transport studies must be cleaved due to their size, which may be as long as 10 cm in length and 1 cm in diameter, they allow for greater flexibility in sample sizes and easier manipulation and formation of transport geometries.

2.1.3 Point Defects And Dislocations

Whether SmB_6 is synthesized by Al-flux or optical floating zone methods, some level of point defects and one-dimensional (1D) defects are present. In regards to point defects, these defects are primarily Sm-centered, whether it is due to impurities of the Sm precursor itself or arising during crystal formation. In the former case, it is well known rare-earth powders are difficult to purify and thus sits as an unavoidable fabrication limitation. In the latter case, the preferred method of forming SmB_6, if these point defects are to be avoided, is the Al-flux grown method, which avoids Sm evaporation present in the floating zone method. In regards to 1D defects, such as dislocations, while there have been limited studies on them within SmB_6 specifically, [108] they are well known within the field of semiconductors as strong scattering centers (such as within GaN). [109] During bulk crystal synthesis, dislocations can nucleate from thermal gradients, compositional inhomogeneities, mechanical vibration, impurity sites or, depending on growth method, may propagate from a dislocation in the seed crystal. [110]

2.2 Preparation Of Crystal Surfaces

For transport studies on SmB_6, having a well-defined surface geometry is critical to obtain meaningful measurements. Due to the fact that as a suspected topological insulator, every exposed surface can conduct. Although the Al-flux grown or cleaved faces of floating-zone SmB_6 are large enough for direct measurements, surface irregularities inflate the effective area and obscure the geometric factors. While polishing may come to mind as a means of

smoothing the surface, conventional polishing can make matters worse: aggressive mechanical polishing induces subsurface cracks that act as hidden conductive pathways, further complicating electrical characterization. [111]

To minimize both the roughness and the subsurface cracks, we adopted a gradual polishing sequence. We start with P1200 SiC grit (15 μm) to thin samples, eliminate large edges or bumps, and, in the case of Al-flux grown crystals, reach a surface with no Al pockets present. This is followed by finer SiC papers, either P2500 (8 μm) and P4000 (5 μm), for an intermediate finish. And then a final polish with a 0.3 µm alumina slurry until no defects were visible under 10× magnification. Alternatively, dilute nitric-acid etching has been suggested as a means to strip surface Sm oxides and improve rougher samples with uniform etching while avoiding the risks of subsurface cracks from mechanical polishing. [112] However, applying this etch to one of our finely polished SmB_6 crystals produced no measurable change in transport behavior, indicating that careful mechanical polishing alone can yield surfaces adequate for precise electrical measurements. It is noted that the polishing must be completed on every surface where measured electrical conduction may occur; thus differing transport geometries require different surfaces to be polished.

2.3 Transport Analysis

Electrical transport experiments in this work were done using a low frequency within the linear response regime (the DC limit. Here, the applied electric field $\mathbf{E}$ produces a proportional current density $\mathbf{j}$ in the sample according to Ohm's law:

$$\mathbf{j} = \sigma \mathbf{E}. \tag{2.1}$$

where σ is the conductivity matrix. A magnetic field $\mathbf{B}$ may also be applied, and it is standard to assume this is in the z-direction while measurements are taken in the $x - y$ plane.

The Drude model is used to analyze transport parameters. The conductivity matrix for

particles with charge e are obtained from Newton's law:

$$\frac{d\mathbf{p}}{dt} = e(\mathbf{E} + \mathbf{v} \times \mathbf{B}). \tag{2.2}$$

If the particle has effective mass m^* and scattering time τ, then

$$m^*(\frac{d}{dt} + \frac{1}{\tau})\mathbf{v} = e(\mathbf{E} + \mathbf{v} \times \mathbf{B}). \tag{2.3}$$

It is also assumed that transport is the steady state case and that the magnetic field is oriented only in the z-direction ($\mathbf{B} = B\hat{z}$). Then, Eq. 2.3 can be written in three dimensions:

$$\begin{aligned} \frac{m^* v_x}{\tau} &= e(E_x + v_y B) \\ \frac{m^* v_y}{\tau} &= e(E_y - v_x B) \\ \frac{m^* v_z}{\tau} &= e(E_z). \end{aligned} \tag{2.4}$$

Using $\mathbf{j} = -ne\mathbf{v}$, where n is the carrier density, to relate velocity to the current density given in Eq. 2.1), the conductivity matrix for a general case can be constructed:

$$\sigma = \begin{pmatrix} \frac{ne\mu}{1+\mu^2B^2} & \frac{ne\mu^2B}{1+\mu^2B^2} & 0 \\ -\frac{ne\mu^2B}{1+\mu^2B^2} & \frac{ne\mu}{1+\mu^2B^2} & 0 \\ 0 & 0 & ne\mu \end{pmatrix}, \tag{2.5}$$

where the mobility is $\mu = e\tau/m^*$. It is assumed that the magnetic field is small enough that $\mu^2B^2 << 1$ and this term can be neglected. When magnetic field is applied in the z-direction as previously assumed, transport measurements are performed only in the $x-y$ plane. Then Eq. 2.5 becomes

$$\sigma = \begin{pmatrix} ne\mu & ne\mu^2B \\ -ne\mu^2B & ne\mu \end{pmatrix}. \tag{2.6}$$

Since resistivity $\rho = 1/\sigma$, the inverse of this matrix gives the resistivity:

$$\rho = \frac{1}{1+\mu^2 B^2} \begin{pmatrix} \frac{1}{ne\mu} & -\frac{B}{ne} \\ \frac{B}{ne} & \frac{1}{ne\mu} \end{pmatrix}. \tag{2.7}$$

where we again make the assumption that $\mu^2 B^2 << 1$. This results in the classical Drude transport equations

$$\begin{aligned} \rho_{xx} &= \frac{1}{ne\mu} \\ \rho_{xy} &= -\frac{B}{ne}. \end{aligned} \tag{2.8}$$

Depending on the transport geometry used, ρ_{xx} and ρ_{xy} can be calculated from the data and used to find the carrier density n and mobility μ. Experimentally, the Hall coefficient $R_H = -1/(ne)$ is often reported in place of ρ_{xy} and can be used to find the carrier density n and the sign of the charge carriers. Then, ρ_{xx} can be used to find the mobility μ.

2.3.1 Two-channel conductivity

Eq. 2.8 is the simplest case of transport in which there is a single type of charge carrier. In many systems, there is more than one conduction channel. Conductivity is additive, so the conductivity matrix Eq. 2.8 can be modified to account for two channels starting from Eq. 2.6 to obtain

$$\sigma_{n_1,n_2} = \begin{pmatrix} n_1 e\mu_1 + n_2 e\mu_2 & n_1 e\mu_1^2 B + n_2 e\mu_2^2 B \\ -(n_1 e\mu_1^2 B + n_2 e\mu_2^2 B) & n_1 e\mu_1 + n_2 e\mu_2 \end{pmatrix}, \tag{2.9}$$

where n_1 and μ_1 are the carrier density and mobility of the first channel, and n_2 and μ_2 are the carrier density and mobility of the second channel. As in the single channel analysis

above, this matrix can be inverted to obtain

$$\rho_{n_1,n_2} = \frac{1}{e^2(n_1^2\mu_1^2(1+\mu_1^2B^2) + n_2^2\mu_2^2(1+\mu_2^2B^2) + 2n_1n_2\mu_1\mu_2(1+\mu_1\mu_2B^2)} \times \begin{pmatrix} n_1e\mu_1 + n_2e\mu_2 & n_1e\mu_1^2B + n_2e\mu_2^2B \\ -n_1e\mu_1^2B - n_2e\mu_2^2B & n_1e\mu_1 + n_2e\mu_2 \end{pmatrix}, \tag{2.10}$$

Again, as above, it is assumed that both $\mu_1^2B^2 << 1$ and $\mu_2^2B^2 << 1$, so the denominator of the prefactor simplifies to $(n_1e\mu_1 + n_2e\mu_2)^2$, so that for two channels

$$\begin{aligned} \rho_{xx} &= \frac{1}{n_1e\mu_1 + n_2e\mu_2} \\ \rho_{xy} &= \frac{B}{e}\frac{n_1\mu_1^2 + n_2\mu_2^2}{(n_1\mu_1 + n_2\mu_2)^2}. \end{aligned} \tag{2.11}$$

Any number of conduction channels may be added in this way. In a topological insulator, there would be a bulk (three-dimensional) electron channel and a surface (two-dimensional) electron channel, as in a topological insulator. To account for dimensionality in combining the terms, the three-dimensional channel should be multiplied by the thickness t. The resulting equations are:

$$\begin{aligned} \rho_{xx} &= \frac{1}{n_2e\mu_2 + n_3e\mu_3t} \\ \rho_{xy} &= \frac{B}{e}\frac{n_2\mu_2^2 + n_3\mu_3^2t}{(n_2\mu_2 + n_3\mu_3t)^2}, \end{aligned} \tag{2.12}$$

where the subscripts here refer to the dimension. In data, the coexistence of two channels can be identified by a bump feature at the point where the two channels contribute equally to the resistance.

2.3.2 Connection to measurement

In a typical electrical transport experiment, a current I is applied to the sample and the resulting voltage drop V is recorded, allowing the resistance to be calculated as $R = V/I$. This resistance serves as the central experimental observable and can be tracked while systematically varying external parameters including temperature, magnetic field, or pressure,

to probe the material's electronic response; the present work focuses on temperature and field sweeps against various strain and gating conditions. R is connected to the intrinsic resistivity ρ derived in classical transport theory and thus allows us to obtain values for desired characteristics. Converting between these two quantities requires knowledge of both the sample dimensions and the contact layout, underscoring the importance of a carefully controlled transport geometry, as is detailed in the following sections.

2.4 Establishing Transport Geometry

Provided that the sample dimensions and electrode layout are accurately characterized, both the longitudinal resistivity (ρ_{xx}) and the Hall resistivity (ρ_{xy}) can be extracted from transport measurements. Three configurations are treated here: van der Pauw geometry, Hall bar geometry, and Corbino disk geometry. Van der Pauw measurements are the most basic, with four contacts placed on four corners of a plate-shaped sample. It is also ideal for samples with non-symmetric shapes for which no other transport geometry would be well-defined. In van der Pauw measurements, two contacts allow for current flow and two are used to measure the voltage. The current contacts may be non-adjacent, allowing for a measurement of R_{xx}, or they may be adjacent, allowing for a measurement of R_{xy}. Hall bars are optimized for elongated or needle-like crystals, and employs separate voltage probes aligned longitudinally and transversely with respect to the current path, allowing simultaneous determination of R_{xx} and R_{xy}. Corbino disks consist of concentric inner and outer circular contacts deposited on a flat surface of the crystal. Current flows radially between the electrodes, removing transverse (Hall) voltages but allowing a direct measurement of R_{xx} that is insensitive to edge effects. Because it can be patterned on any polished face, the Corbino configuration is particularly useful for isolating surface conduction in layered materials, for studying each crystal plane of a material individually, and for disentangling bulk and surface contributions. Figure 2.2 shows each of these geometries.

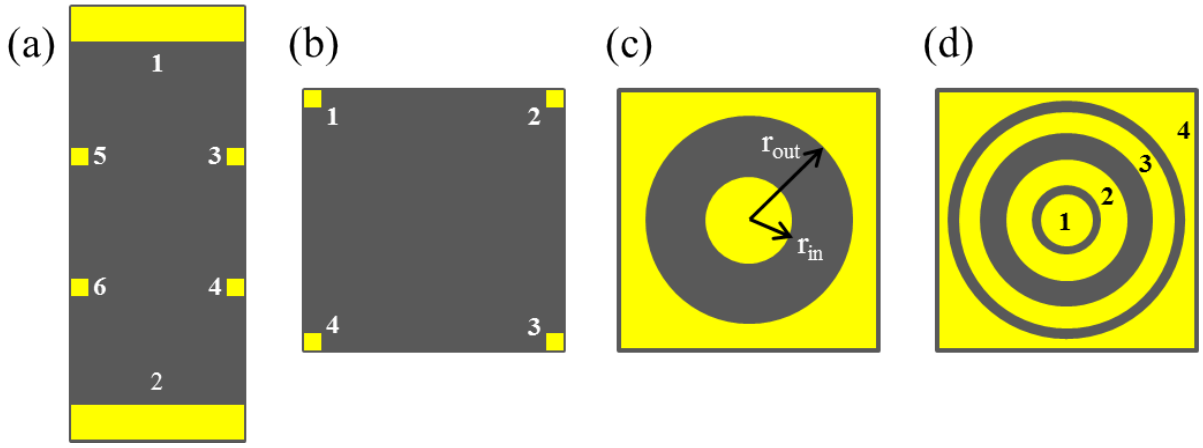

Figure 2.2: Schematics of (a) Hall bar geometry, (b) van der Pauw geometry, (c) standard Corbino disk, and (d) four-terminal Corbino disk.

2.4.1 Hall bar geometry

The layout of Hall bar geometry shown in Fig. 2.2(a). R_{xx} is measured by $R_{1,2;3,4}$, meaning that current flows from contact 1 to contact 2, and the response is measured between contacts 3 and 4. R_{xy} is measured by $R_{1,2;3,5}$. These are converted to ρ_{xx} and ρ_{xy} by

$$\begin{aligned} \rho_{xx} &= \frac{wt}{\ell} R_{xx} \\ \rho_{xy} &= tR_{xy} \end{aligned} \tag{2.13}$$

where w, t, and ℓ are the width, thickness, and length of the sample. The prefactor of ρ_{xx}, in this case wt/ℓ, is called the "geometric factor" of the transport geometry. The Hall coefficient is related to the above parameters by

$$R_H = \frac{\rho_{xy}}{B} = \frac{t}{B} R_{xy}. \tag{2.14}$$

2.4.2 Van der Pauw geometry

A schematic of van der Pauw geometry [113] on a square sample is shown in Fig. 2.2(b). R_{xx} is obtained by an average of $R_{1,2;4,3} = R_{xx,1}$ and $R_{1,4;2,3} = R_{xx,2}$, while R_{xy} requires either

$R_{1,3;2,4}$ or $R_{2,4;1,3}$. Then, ρ_{xx} and ρ_{xy} are obtained by

$$\begin{aligned} \rho_{xx} &= f\frac{\pi t}{\ln 2}\frac{R_{xx,1}+R_{xx,2}}{2} \\ \rho_{xy} &= tR_{xy} \end{aligned} \tag{2.15}$$

where, in the geometric factor, f satisfies

$$\frac{R_{xx,1}-R_{xx,2}}{R_{xx,1}+R_{xx,2}} = f\cosh^{-1}(\frac{\exp \ln 2/f}{2}). \tag{2.16}$$

If the measurements of $R_{xx,1}$ and $R_{xx,2}$ are identical, $f = 1$. In square samples, f is usually approximated as 1, although a few percent correction can be made by including this factor.

2.4.3 Corbino geometry

Standard Corbino geometry, shown in Fig. 2.2(c) is made up of two concentric circular contact pads, where current flows from the inner ring to the outer ring. [114] Voltage is measured in the region between the two disks. The measured R_{xx} is related to transport parameters by

$$R_{\text{Corbino}} = \frac{\ln(r_{out}/r_{in})}{2\pi}\frac{1+\mu^2B^2}{ne\mu} = C\rho_{xx}, \tag{2.17}$$

where the inner (r_{in}) and outer (r_{out}) radii are the radii of the two current contacts. An adaptation of the standard Corbino geometry used in this work utilizes the four-terminal Corbino disk, shown in Fig. 2.2(d). Measured R_{xx} would here be obtained by $R_{1,4;2,3}$.

2.4.4 Inverted resistance measurements

Corbino disk geometry is extremely powerful for topological materials because it allows a single surface to be isolated and it allows edge effects to be removed. In the inverted resistance method, Corbino disk geometry allows the surface and bulk conduction channels to be separated. [115, 50] Here, at least four concentric rings are needed, and varying which rings function as current and voltage electrodes allows the researcher to select which conduction channel is measured. In a standard measurement, the current would flow from the innermost to the outermost electrode, and voltage measurements would be taken at the

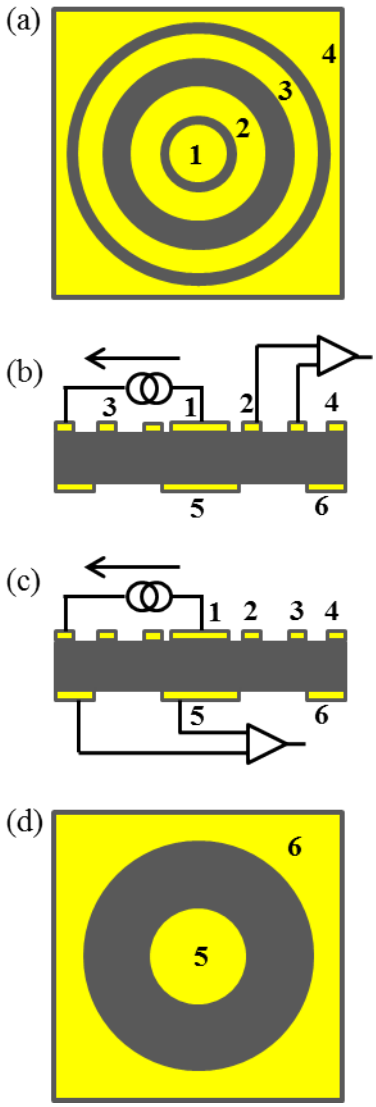

Figure 2.3: Schematic of two-sided inverted resistance measurement. (a) Top surface, with a four-terminal Corbino geometry. (b) Side view, showing a standard resistivity measurement. (c) Side view, showing an inverted resistance measurement. (d) Bottom surface, showing a two-terminal Corbino geometry.

two inner electrodes. In the inverted method, current is confined between the two innermost electrodes. If the measured material is purely two-dimensional, no signal would be measured, as the current is confined to the surface between the inner electrodes. In a three-dimensional material, the inverted resistance measurement would pick up a small signal arising from the bulk channel only.

Consider three cases. First, if the material is a purely bulk conductor, the resistance is proportional to the bulk resistivity as in Eq. 2.17:

$$R = C_b \rho_{xx}, \tag{2.18}$$

where C_b is a geometric factor (as in Eq. 2.17).

If surface conduction is dominant, the standard measurement will be proportional to the surface resistivity (also known as sheet resistance), R_{sq}:

$$R = C_s R_{\mathrm{sq}}, \tag{2.19}$$

where C_s is also a geometric factor but with different form than C_b due to the reduced dimensionality.

If signal depends on both the bulk and surface resistivities:

$$R_{\mathrm{Inv}} = C_{\mathrm{Inv}} \frac{R_{\mathrm{sq}}^2}{\rho_{xx}}, \tag{2.20}$$

where C_{Inv} is another geometric factor. Because Eq. 2.20 is inversely proportional to bulk resistivity, the temperature dependence of the inverted measurement will be inverse to the temperature dependence of the bulk measurement in regions where bulk conduction dominates.

In practice, a larger signal for the inverted measurement is obtained by using a double-sided Corbino configuration, where a four-terminal Corbino is fabricated on one side of a sample and a two-terminal (standard) Corbino is fabricated on the reverse side, shown in Fig. 2.3(a) and (d). Fig. 2.3(b) illustrates a standard measurement, as described above for a four-terminal Corbino disk. Besides using $R_{1,2;3,4}$ as described above for the inverted

resistance, $R_{1,4;5,6}$ is also an inverted measurement, as surface conduction is confined to the top plane of the sample, and only current traveling through the bulk is measured on the bottom surface.

2.4.5 Fabrication

After the SmB_6 sample surface is prepared, contact pads are added in the desired transport geometry. For a Corbino disk, we rely on standard photolithography processes in the cleanroom of the Lurie Nanofabrication Facility: S1813 photoresist is spun to 1.3 μm on a CEE 100 spinner, the pattern is exposed for 6 s with an MJB-3 contact aligner, and the resist is developed in AZ726 on the CEE developer. A brief plasma exposure using the YES plasma strip removes residual organics, after which 50 Å of Ti and 1500 Å of Au are evaporated in the Enerjet system and lifted off in an acetone bath using an ultrasonic apparatus.

Crystal size introduces complications to the processing because the SmB_6 pieces used are only a few millimeters across, whereas semiconductor device fabrication tools are optimized for full wafers. Small samples can develop a thick resist "bead" along one edge during spin-coating; if the Corbino disk placement overlaps this bead, subsequent patterning fails. To mitigate this, crystals are often polished alongside dummy Si or glass pieces so the bead forms on the dummy material instead of the sample. For Hall bar or van der Pauw geometry, the irregular crystal sizes make a single photomask impractical, so contacts are defined either by hand-painting S1813 or by using a shadow mask before following the same cleaning, metallization, and lift-off steps.

After the pads are formed, gold wires are attached by wire bonding or by-hand with silver paste or indium. Wire bonding is preferred for narrow Corbino contacts. Silver paste offers flexibility and ease for Hall bars, but can lift off easily if the surface is not cleaned properly beforehand. Indium yields the most robust joints, which are crucial for samples submerged in liquids or under strain, but the heated soldering iron risks damaging pads or the sample. Regardless of the method, care must be taken to keep the adhesive strictly within the pad boundaries to preserve the intended geometry, especially on samples patterned by hand or shadow masks.

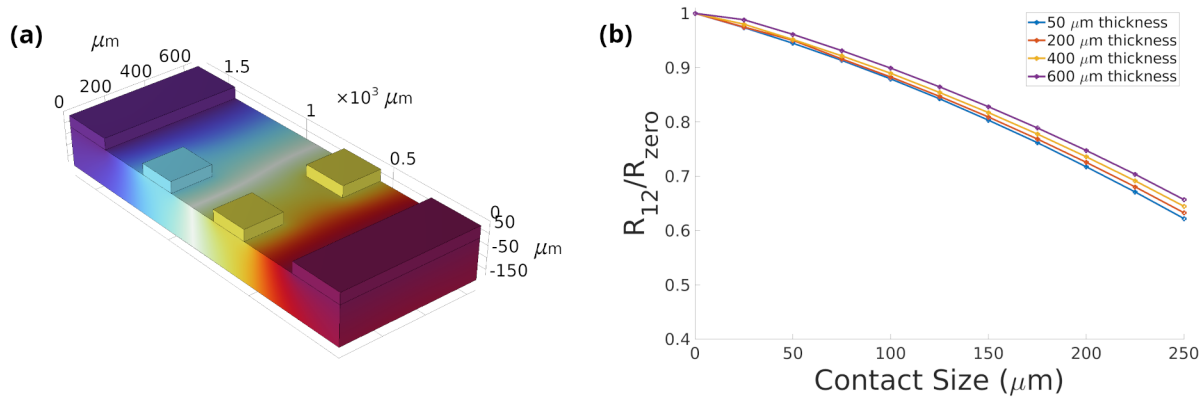

Figure 2.4: (a) An example simulation based on a three voltage contact Hall bar geometry, (b) a plot of the simulated to ideal resistance ratio as a function of contact size, with samples of various thicknesses provided. Figure courtesy of E. Chandler

2.4.6 Contact Corrections

Although the contacts and subsequent wire attachments are done with care, the contacts often do not have perfectly uniform shapes or sizes, or the wiring agent may extend beyond the bounds of the contact. This is especially true in the cases where the patterns or wiring are done by hand. The finite size of the contacts themselves leads to an imperfect geometry which can have an effect of up to an order of magnitude on the measurements, and nonuniform shapes make it difficult to calculate the appropriate corrections. To reduce these errors and improve derived material values from the experiments, contact simulations were performed.

These contact simulations were made using COMSOL to carry out finite element analysis. A simulated SmB_6 sample is created using the geometric values of the measured sample, with a separate insulating bulk and conducting surface. Simulated copies of the contacts, as shown in Fig. 2.4(a), are then made using reference photos of the contacts and wire adhesive wherein precise measurements were taken under a microscope. The simulated replica then runs a transport experiment to find the conductivity between contacts and then compares that to a simulated replica using ideal contacts. The result is a correction factor based on the particular sample in question, which is then applied directly to the resistance to obtain an accurate resistivity value. The correction factor as a function of contact size for the simulation is shown in Fig. 2.4(b).

Chapter 3

Bulk Measurements of Pure and Doped SmB_6

3.1 Introduction

In Chapters 1 and 2, differences between aluminum flux grown and floating zone grown SmB_6 were highlighted. An overview of the methods used to grow these samples as well as concerns about quality and consistency in each growth method were given in Chapter 2. In Chapter 1, a multitude of experimental results on both types of samples were summarized, with a key component being the dependence of study results on the sample growth method. Floating zone samples tend to yield reports of trivial surface states, [66] a three-dimensional Fermi surface, [85, 86, 87] and variable thermal conductivity and transport behavior. Al flux grown samples generally yield resistivity with temperature-independent plateaus. [31, 116, 105] Floating zone samples are less consistent and can behave similarly to flux-grown samples, show temperature-dependent behavior, or even a step-like behavior. [117, 39, 81] An open question is whether these differences in behavior are due to different surface characteristics or bulk characteristics. If the differences are due to surface characteristics, the low-temperature bulk behavior should be similar between both types of samples. But, if bulk characteristics differ at low temperatures, this would be reflected in inverted resistance measurements.

In this chapter, a detailed study of the bulk of SmB_6 on both flux and floating zone

grown samples is presented. Previous data using the inverted resistance method for Al flux grown samples reported in PNAS (Ref. [93]) are included; the pure (undoped) Al-flux sample showed insulating behavior down to 2 K while samples grown intentionally with off-stoichiometry to induce vacancies demonstrate a small residual bulk conduction channel. A comparison of Al flux and floating zone grown samples by inverted resistance, reported in Phys. Rev. Materials (Ref. [108]), is also discussed here. This result shows that the floating zone samples contain bulk conduction at the lowest temperatures, but vary between samples, perhaps due to growth conditions in the optical furnace. Given the similarity in low temperature conduction between the intentionally off-stoichiometry flux grown samples with vacancies and the floating zone samples, the attribution of this bulk channel to point defects and dislocations (one-dimensional defects) is presented. The presence of dislocations in both Al flux and floating zone grown samples is verified through chemical etching. Finally, the role of doping with both magnetic (Eu) and non-magnetic (La) metals is discussed.

3.2 Comparing Samples with Inverted Resistance

As introduced in Chapter 2, the inverted resistance measurement comprises a voltage measurement outside of the region where current flows. In a Corbino disk geometry with four concentric circles, an inverted measurement can be set up by confining current between the two inner rings and measuring the resulting signal on the two outer rings. [115] If a material is a pure surface conductor, the resulting signal is zero as the second-to-innermost ring acts as a Faraday cage to constrain the current inside. For materials with both surface and bulk conduction, then, the measured signal must arise from the bulk. In the study in Ref. [93], a double sided Corbino disk is utilized; this method was discussed in Chapter 2 and a sketch of the geometry can be found in Fig. 2.2.

Both the standard and inverted resistance measurements are used to create a single "inverted" curve. In SmB_6, the standard resistance curve is proportional to the bulk resistivity (ρ_b) above about 5 K but proportional to surface resistivity (ρ_s) below this temperature. The inverted curve is also proportional to the bulk resistivity above about 5 K, because bulk conduction is dominant at higher temperatures. At lower temperatures, the inverted curve

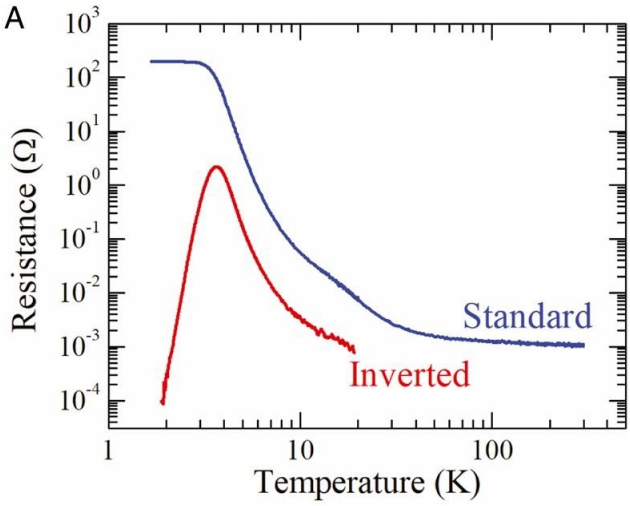

Figure 3.1: Example of standard and inverted curve of a stoichiometric Al flux grown sample.

contains surface and bulk contributions described by $R_{\text{Inv}} \propto \rho_s^2/\rho_b$. An example of standard and inverted resistance curves in a flux-grown sample is shown in Fig. 3.1.

To calculate the bulk resistivity over the whole temperature range, $1/R_{\text{Inv}}$ is calculated; since $R_{\text{Inv}} \propto \rho_s^2/\rho_b$, $1/R_{\text{Inv}} \propto \rho_b$. The resultant curve extends the activated bulk behavior seen in the standard curve above 5 K to temperatures below 5 K. Due to misalignment of the two Corbino disks during patterning, the two curves do not always match exactly, but they can be aligned following Refs. [115, 93].

The inverted resistance method was used to measure bulk transport on four flux grown SmB_6 samples from 2-300 K. The sample S1 was grown stoichiometrically, with a 1:6 Sm:B ratio. S2, S3, and S4 were grown with off-stoichiometry, which allowed the introduction of Sm vacancies. A summary of the four samples and their characteristics is given in Table 3.1. While the three samples grown with off-stoichiometry differ in properties compared to S1, the exact percent of vacancies is difficult to measure and likely does not match the growth ratio.

During sample preparation, as outlined in Chapter 2, the non-stoichiometrically grown SmB_6 samples were observed to polish significantly faster than stoichiometrically grown samples. To check if this observation was consequential, the microhardness of the samples that were used in the transport studies was tested. It is known that the introduction of defects into a crystalline material can influence the microhardness. The relationship between

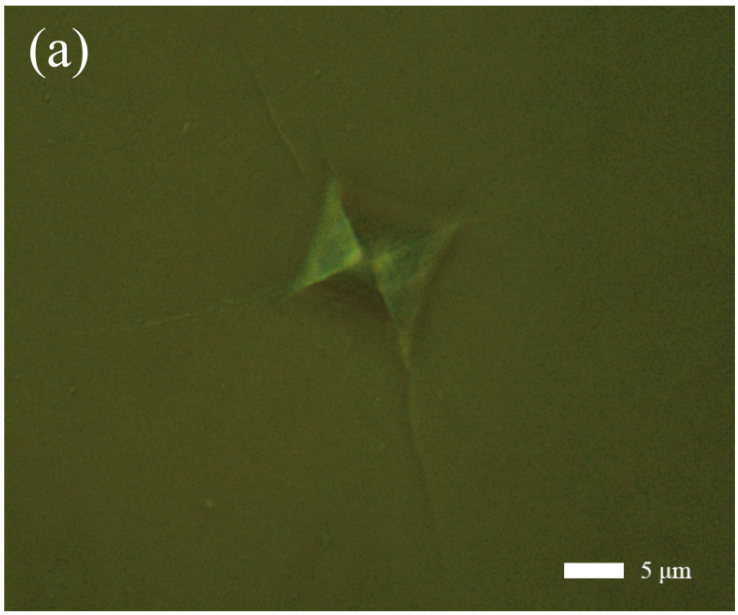

Figure 3.2: Example of of an indentation after a Vickers microhardness measurement.

Sample	r	E_a (meV)	Hardness (kgf/mm^2)
S1	0	4.01 ± 0.0054	2191 ± 125
S2	0.1	4.12 ± 0.0041	1913 ± 16.5
S3	0.25	3.97 ± 0.0047	1781 ± 111
S4	0.40	3.85 ± 0.0038	1563 ± 50.8

Table 3.1: Details of the four flux grown samples measured. Samples were grown with a starting composition Sm:B:Al = $(1-r)$:6:700, where r also gives the percentage of Sm vacancies.

hardness and point and extended defects is not universal, but hardness is known to be inversely proportional to extended defects. [118] Microhardness of the samples was measured using the Vickers hardness test, which is performed by applying a force on the flat (001) surface using a pyramidal diamond indenter and then measuring the area of indentation. A picture of a typical indentation is shown in the figure. For each specimen, multiple indentations were made with a force of 300 kgf and the area was measured in an optical microscope. This was repeated on multiple samples from the same batch to determine an average Vickers Pyramid Number (HV). The HVs of samples from the same batches as S1, S2, S3, and S4 are given in Table 3.1, and an example indentation is shown in Fig. 3.2 The values of Vickers microhardness show that all four samples indeed differ physically.

Results from these four samples are shown in Fig. 3.3. In the stoichiometrically grown

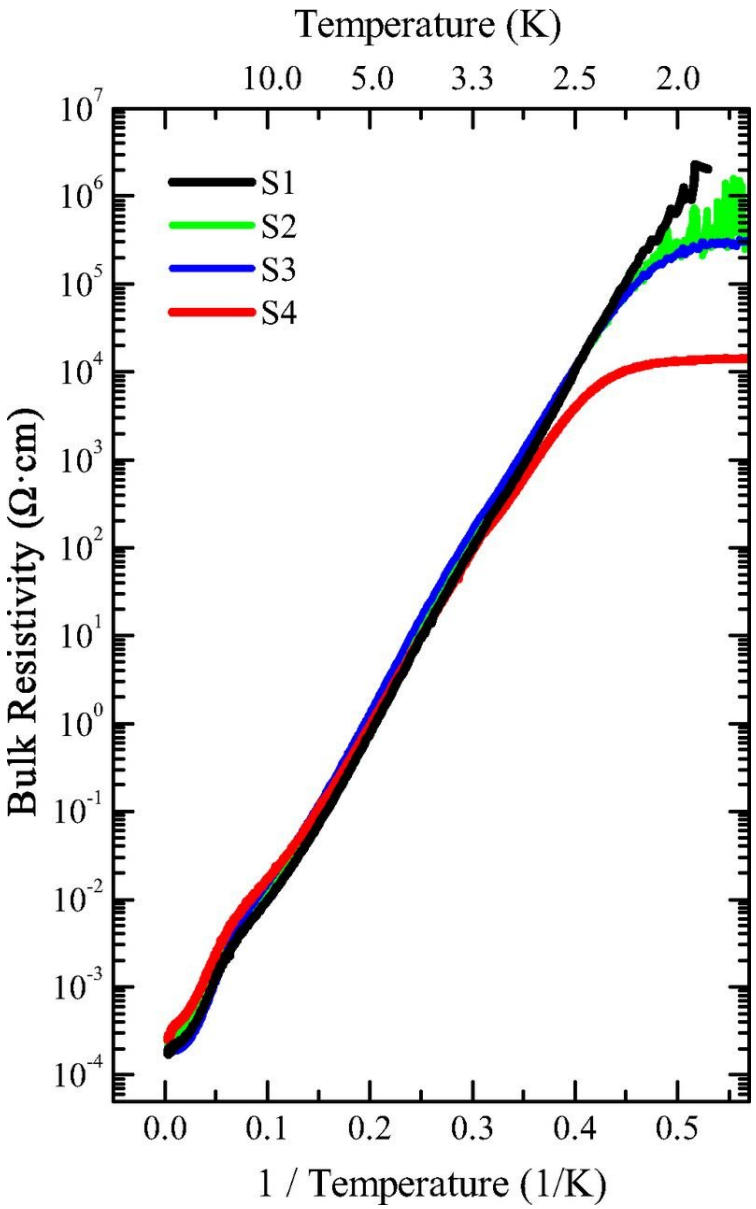

Figure 3.3: Inverted resistance measurement of four Al flux grown SmB_6 samples of varying stoichiometry.

sample (S1) result, the activated behavior continues at low temperatures, indicating that the carrier density continues to decrease as the temperature is decreased with a total of ≈10 orders of magnitude. From this continuing exponential decrease, we estimate a carrier density of 10^{12} (cm^{-3}) at the lowest measurable temperature (2 K). This implies that there are only ≈107 carriers in the bulk region of our entire sample at this temperature, and there would be less than 1 bulk carrier below 1 K by extrapolating the thermally activated behavior. The off-stoichiometrically grown samples (samples S2, S3, and S4) also indicate that no more than 10^{15} (cm^{-3}) bulk carriers are left before the bulk resistivity saturates below 2.5 K. For the saturation of the nonstoichiometrically grown samples, the magnitudes are too high for them to be attributed to the extrinsic regime of a semiconductor. It is important to note that this is in stark contrast to other hexaboride systems and other Kondo insulators that all show strong dependence of disorder in the temperature-dependent resistivity measurements. Notably, this resistivity saturation after such a large increase of magnitude is only seen in very pure semiconductors. [119, 120]

Nevertheless, the low-temperature resistivity saturations in the nonstoichiometrically grown samples indicate that there is a small response to disorder. Fits of the data to the temperature-dependent hopping conduction through an impurity band are not compelling, and the high resistivity magnitude makes this case unlikely. One possibility is that the conduction path has a confined or lower-dimensional percolative current channel instead of a homogeneous channel in the bulk. A plausible possibility is that extended defects, such as grain boundaries and dislocations, harbor topologically protected conduction and may be a conduction path. We observe signatures of twinning in our samples and a smaller hardness in the off-stoichiometric–grown samples that indicate that crystallographic defects like dislocations are certainly present in the samples we measure. [93]

3.3 Results on floating zone samples

Four floating zone samples were prepared for the inverted resistance measurement. Details of the samples' origins and growth methods can be found in Table 3.2. All samples were polished with grits down to 0.3 μm. The Corbino disks were patterned by photolithography.

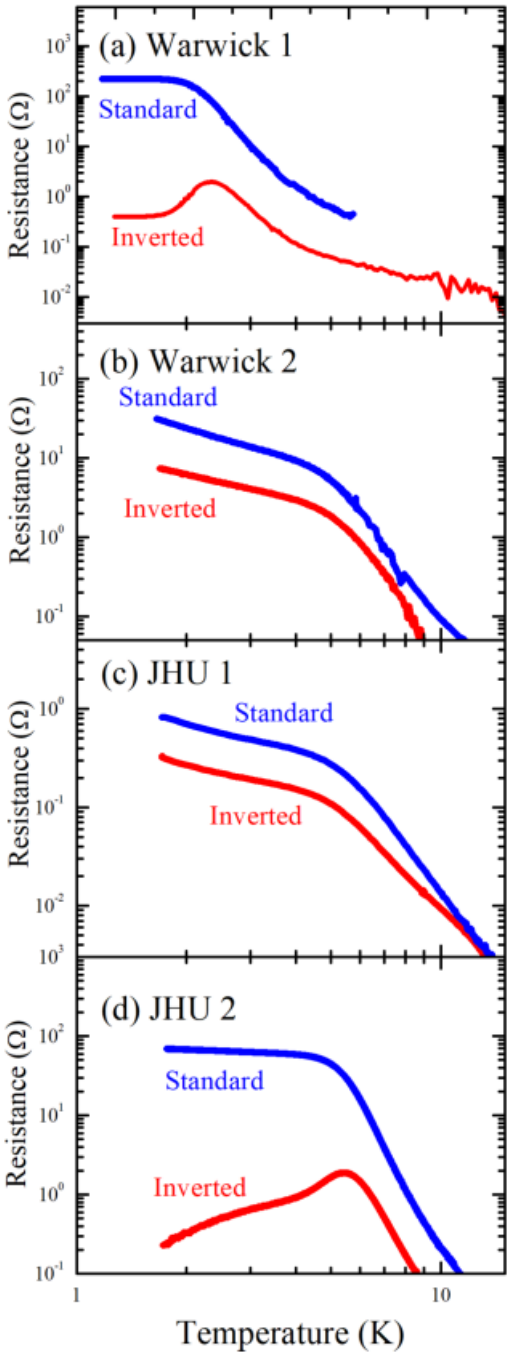

Figure 3.4: Inverted resistance measurement of four floating zone grown SmB_6 samples.

Sample	Growth details	Starting powder origin
Warwick 1	Standard growth [82]	Alfa Aesar
Warwick 2	Standard growth [82]	American Elements
JHU 1	Standard growth [81]	Testbourne Ltd.
JHU 2	Doubly-isotope enriched, Sm deficient	Alfa Aesar

Table 3.2: Details of the four floating zone samples measured. Sample names indicate growths by collaborators at University of Warwick (Warwick) and Johns Hopkins University (JHU).

Ti/Au was deposited on the samples using e-beam evaporation and later a lift-off process with acetone was used to define the pattern and electrodes. We used gold wires to make electrical connection from the electronics to the sample, and attached them using either silver paste or wire bonding.

Fig. 3.4 shows the resistance vs. temperature of all four samples. The blue curves are the standard resistance measurements and the red curves are the inverted resistance measurements. In the standard measurements (blue curves), all four samples show a change in slope around 4 K that would conventionally be regarded as a surface plateau. Fig. 3.4 (a) and (d) show little to no temperature dependence in the standard measurement below about 4 K, especially compared to Fig. 3.4 (b) and (c). Using the inverted curves (red), we can determine whether these "plateaus" arise from surface or bulk conduction channels. We see dramatic differences in the inverted resistance results for each sample. Fig. 3.4 (a) shows a resistance that drops and saturates, similar to the non-stoichiometric flux growths observed previously. [93] The inverted resistance measurement shown in Fig. 3.4 (d) has a feature similar to Fig. 3.4 (a) but also a moderate drop at lower temperatures. In Fig. 3.4 (b) and (c), we see a temperature dependence that is close to parallel to the standard measurement.

We convert the measured resistances to bulk resistivity in Fig. 3.5, except for the sample Warwick 1 (Fig. 3.4(a)) which was complicated to convert due to the Corbino disks being placed on different crystal planes. We compare the results from this study to the previously reported result on a stoichiometric flux grown sample (black trace). [93] We find that the remaining three floating zone grown samples have a significant slope change in bulk resistivity which indicates that the intrinsic exponential temperature dependence in bulk resistivity is interrupted. That is, another bulk conduction mechanism is present in these samples in

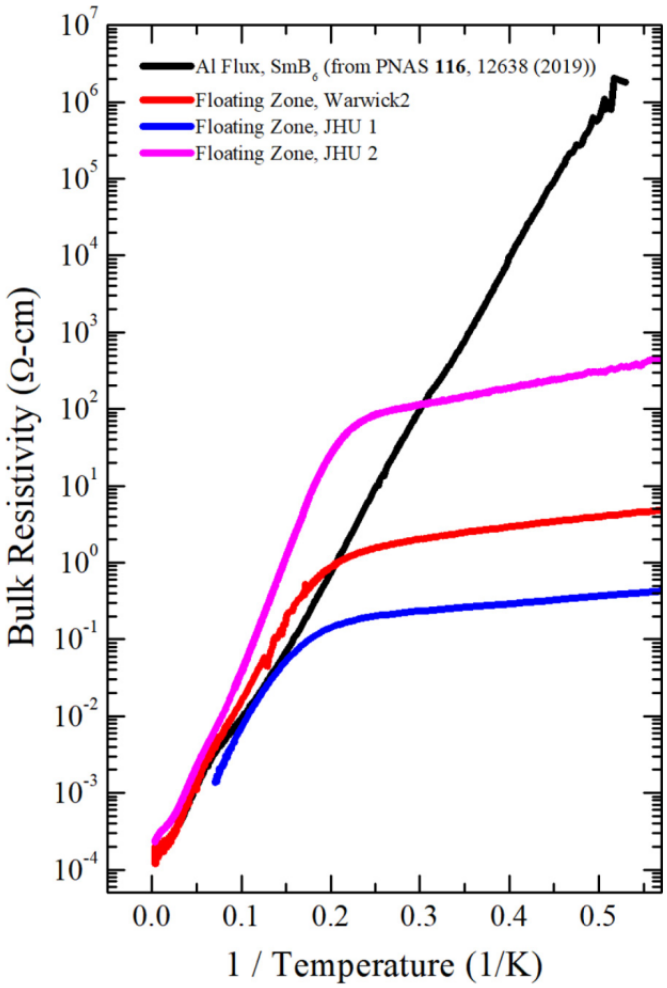

Figure 3.5: Bulk resistivity conversion from Fig. 3.4 measurements plotted with the stoichiometric flux grown sample.

addition to the standard mechanism responsible for activated behavior.

3.4 Defects and Dislocations

Figs. 3.4 and 3.5 show that the four floating zone samples presented here have non-negligible bulk conduction, but the characteristics of the bulk conduction differ by sample. In Fig. 3.4 (b) and (c) the standard and inverted resistance curves are parallel to one another, demonstrating that these samples are bulk conductors and can be described by Eq. 2.18. In terms of transport, this means that either the surface conduction is nonexistent or that the bulk conduction channel dominates.

Many researchers have proposed impurities as a possible origin for residual bulk conduction in SmB_6. Most point defects come from the starting material, as rare earth elements are notoriously difficult to purify. In our samples, the starting materials were sourced from different companies, so the purity of the Sm used in the growth may differ among samples. One way to reduce rare earth impurities is via isotopic purification to Sm-154, as was done for our sample JHU 2. The only remaining rare-earth impurity is Gd-154, which is magnetic. [89] Gd impurities have been studied previously, beginning with the observation that the substitution of even 1% Gd could dramatically change the electrical properties of SmB_6. [121] Later, a Gd doped sample was used to test the TI hypothesis by searching for time reversal symmetry breaking below 4 K. [122] Gd impurities have also been shown to increase the residual heat capacity at low temperatures [89] and have been suggested as an avenue for screening of the Kondo effect at low temperatures. [123] Debate is ongoing about the role of Gd impurities; recent reports have suggested that it is not responsible for bulk dHvA oscillations. [99] However, the local environment of Gd impurities is metallic even at very low concentrations, and at higher concentrations this could lead to percolation through the sample in transport measurements. [90]

Results from the isotopically purified sample shown in Fig. 3.4 (d) have different features in the inverted resistance curve compared to the non-purified samples (Figs. 3.4 (b) and (c)). Since the standard and inverted curves are not parallel, this sample does not have dominant bulk conduction, but it may have parallel surface and bulk channels. Since the sample is isotopically pure, the bulk channel could come from the remaining Gd impurities, Sm vacancies introduced during growth, or both.

A model of impurities used in semiconductors and other materials is the effective mass approximation, where the impurity is treated hydrogenically, with an effective Bohr radius and binding energy. [124] As discussed in Chapter 3, the conditions for standard hydrogenic impurites are not satisfied in SmB_6 when the model for semiconductors is used. [125] However, the model introduced by B. Skinner in Ref. [126] demonstrated that the effective mass approximation can be modified for SmB_6. In the Skinner model, the quadratic potential used in the original treatment of the effective mass approximation [124] is swapped for the "Mexican hat" dispersion seen in SmB_6. New conditions for the effective radius and binding

energy of the impurity state are determined. The total dc conductivity in the presence of these new impurity states is also derived and found to be a combination of the standard activated behavior with activation energy E_1 and an activated hopping term with activation energy E_3, [126]

$$\sigma(T) = \sigma_1 \exp\left(\frac{E_1}{k_B T}\right) + \sigma_3 \exp\left(\frac{E_3}{k_B T}\right). \tag{3.1}$$

This type of impurity band could be present in all samples and could describe both magnetic and nonmagnetic point impurities, including Sm vacancies. As discussed earlier in the chapter, since the addition of Sm vacancies to flux grown samples has been shown to induce bulk conductivity, [93] some portion of the residual bulk conductivity seen in this work in floating zone samples could also be due to Sm vacancies as described above. However, the magnitude of the bulk conduction seen in the inverted measurements is much greater in all the floating zone samples, including the isotopically purified sample, so it is unlikely that vacancies or impurities alone could be the origin.

Another possibility for the source of the residual bulk conduction is one-dimensional defects, or dislocations. These have been studied in semiconductor thin films, where they provide a significant source of scattering. [109] Dislocations form during thin film growth, especially at interfaces where a substrate and film have different lattice constants. The strain on the deposited layer due to lattice mismatch leads to their formation, with dislocations forming in the growth direction and terminating on the top surface of the film. The density of dislocations in a film can be estimated by the change in lattice parameter, $n_{\mathrm{dis}} = |1/a_1^2 - 1/a_2^2|$, where a_1 and a_2 are the lattice parameters on the two surfaces of the film. [127]

Dislocations can also form in crystals due to internal stresses during growth. Impurities, including vacancies, create nucleation sites for dislocations. Thermal fluctuations in the growth can also promote dislocations, and the high temperatures at which growth occurs can exacerbate thermal problems. [127] Important for floating zone growth, dislocations can extend from a seed crystal containing dislocations to new growth based on that seed. [110] Also, dislocations do not have to form and terminate only along the direction of growth; dislocations could also terminate on the side surfaces of the crystal, as shown in Fig. 3.6. Thus, the dislocation density in crystals is expected to depend both on the change in lattice

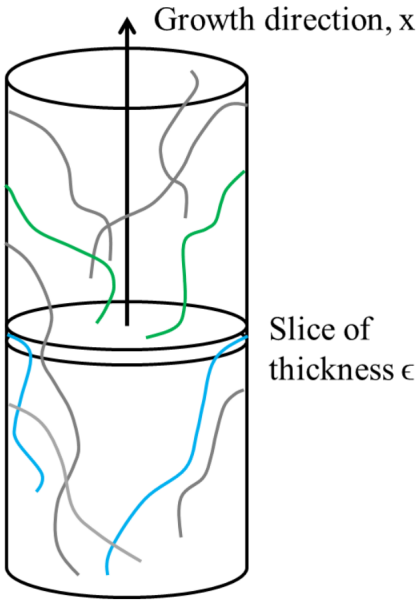

Figure 3.6: Sketch of dislocations in a floating zone boule. Dislocations colored green are those that begin within a slice of thickness ϵ, while those colored blue end within that slice. The remaining grey dislocations may pass through the slice but otherwise begin and end elsewhere.

constant in the direction of growth and on the size (radius) of the crystal.

While dislocations are expected to form in both flux and floating zone samples, the effect of dislocations would be more pronounced in floating zone samples as thermal fluctuations in the feed rod and high temperatures are both characteristic to floating zone growth. The long size of the feed rod and previous studies on the quality of the crystal declining as the growth moves away from the seed crystal would also make floating zone growth more susceptible to dislocations. In SmB_6, one study reports a change in lattice constant over the length of a floating zone sample. [81] Unlike the case of thin films, to the best of our knowledge there is no literature describing how to estimate dislocation density in bulk crystals where there is a variation in lattice constant. Here, we introduce a method to understand the formation of dislocations in bulk materials. Later, we use our model to estimate the dislocation density in SmB_6 samples. We consider a floating zone sample as its size and growth parameters make it susceptible to dislocation formation.

To estimate the dislocation density, we model the floating zone rod as forming from a series of thin slices of thickness ϵ as the molten zone passes through the furnace. In analogy

with the equation above for semiconductor thin films, the total number of dislocations that nucleate within the slice is

$$\left| \frac{1}{(a(x))^2} - \frac{1}{(a(x+\epsilon))^2} \right| (\pi r^2) \tag{3.2}$$

where $a(x)$ is the lattice parameter at a location x along the growth direction and r is the radius of the crystal. A sketch of these is shown in green in Fig. 3.6. All the dislocations that form in this slice must terminate somewhere on the surface of the sample, whether on the sides or the ends. To account for the dislocation terminating on the sides, we introduce an angle θ_{d} which the dislocation makes with respect to the growth direction. Then, the number of dislocations that terminate within a slice (shown in blue in Fig. 3.6) is related to the surface area of the slice, the dislocation density (n_{dis}), and θ_{d} by

$$(2\pi r\epsilon) n_{\mathrm{dis}} \cos\theta_{\mathrm{d}}. \tag{3.3}$$

Here, $\cos\theta_{\mathrm{d}} = 1$ would correspond to all dislocations oriented along the growth direction. We expect $cos\theta_{\mathrm{d}} < 1$ in an actual sample, since dislocations are expected to terminate randomly on the surface but form with the growth of the rod. Since all the dislocations that formed must terminate, Eqs. 3.2 and 3.3 are equal. Expanding Eq. 3.2 as a Taylor series, we calculate that the estimated dislocation density is

$$n_{\mathrm{dis}} = \frac{r}{\cos\theta_{\mathrm{d}}} \frac{|\nabla a(x)|}{(a(x))^3} \tag{3.4}$$

for the dislocation density.

We can estimate the dislocation density in the sample with reported change of lattice constant from Ref. [81]. The lattice parameter in that sample was $a_1 = 4.134309$ Å on one end of the crystal and $a_2 = 4.133343$ Å on the other end, 8 cm away. The radius of the crystal was 3 mm. Using these values with Eq. 3.4, we estimate that the dislocation density in this floating zone sample is $\sim 10^{10}$ cm^{-2}.

Dislocations are commonly imaged by preparing samples as for transmission electron microscopy (TEM). However, the estimated density of dislocations we calculated is too small to use this method. Instead, we used chemical etching to reveal points where dislocations

terminate on the surface. During etching, material is removed from the area near a crystal defect at a different rate than from the lattice. The etching method allows defects, including dislocations, to be imaged optically. [109] The "etch pit" that forms also mirrors the crystal structure of the sample; for SmB_6 we expect to see square etch pits aligned with the crystal direction. With longer etching time, the size of the etch pits increases and more etch pits start to form, so that the etch pit density observed provides a lower bound on the actual dislocation density.

Equal parts nitric and sulfuric acid diluted to 10% were used to etch flux grown and floating zone SmB_6 crystals. After etching, we observed etch pits using a scanning electron microscope in both types of samples. Examples of etch pits are shown in Fig. 3.7. The floating zone sample shown was etched for 340 seconds and had an etch pit density of 10^5 cm^{-2}. The flux grown sample shown was etched for 600 seconds and had an etch pit density of 2×10^3 cm^{-2}. Even though the flux grown sample was etched longer than the floating zone sample, it has a lower density of etch pits observed, suggesting that the floating zone sample hosts more dislocations than the flux grown sample. In both samples, the locations of the etch pits is nonuniform, which suggests that local inhomogeneities in temperature or stoichiometry, for example, during sample growth are important to the formation of dislocations. In both cases, the observed densities are much lower than the calculated estimate of 10^{10} cm^{-2}, but since imaging was performed immediately after identifying that etch pits were present, our values are lower bounds on the number of dislocations actually present in the samples. Since there is significant sample-to-sample variation in floating zone samples, it is also possible that our floating zone sample had fewer dislocations than the one in Ref. [81].

In addition to impurity hopping and dislocations, we briefly consider other theories proposed to explain some of the novel results of SmB_6. First, the proposal that SmB_6 is a nodal semimetal [94, 95] is inconsistent with the low-temperature bulk conduction that we observe, and it does not explain the difference between flux and floating zone grown samples. Our inverted resistance curves show two regions of activated behavior (above and below about 4 K) rather than activated behavior above 4 K and linear-in-T behavior below 4 K. Next, in heat transport, excess thermal conduction at low temperature was not found in flux-grown samples, and reports have disagreed about whether thermal conduction is present univer-

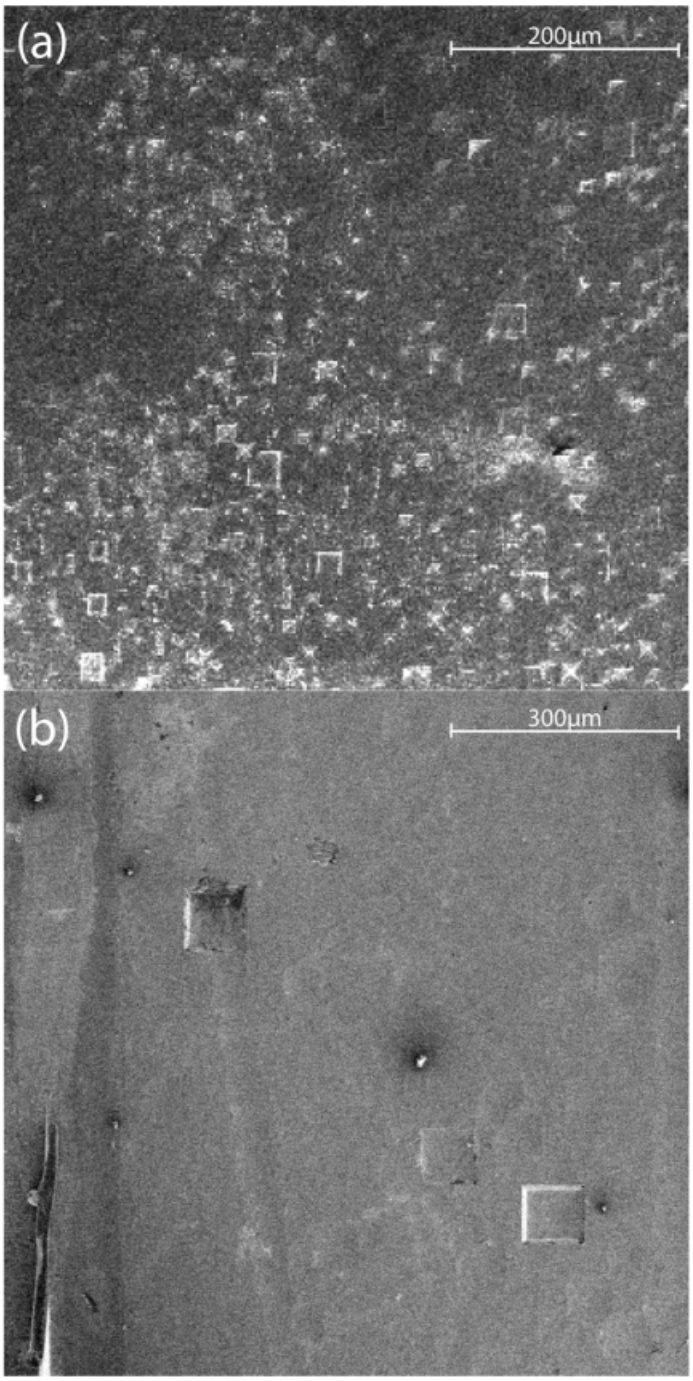

Figure 3.7: Examples of etch pits on the (001) surfaces of (a) a floating zone sample etched for 340 seconds and (b) a flux-grown sample etched for 600 seconds.

sally in floating zone samples. [85, 86, 87]. Theories attempting to reconcile these conflicting results have focused on the possibility that the floating zone samples contain charge-neutral excitations and primarily explored their relevance to dHvA oscillations rather than transport. Our data do not provide evidence for charge-neutral excitations, but the low-temperature bulk channel we observe could conduct heat and contribute to dHvA. Even in samples with very few rare earth impurities, [99] dislocations could still contribute to these effects. A better understanding of the role of dislocations, or more generally, the conduction channel we observe here, will be an intriguing area of further study.

3.5 Doping and Physical Characteristics

Despite the attribution of many features reported in literature to impurities, systematic impurity studies on SmB_6 are few, particularly in transport. Dopants were initially studied as a way of understanding, [121] and later tuning, the mixed valence characteristics. [21, 23, 128] More recent studies on dopants have focused on Gd. Since Gd is magnetic, it would be expected to break time reversal symmetry and significantly change the properties of a topoological surface state in SmB_6. As mentioned earlier in this chapter, Gd-154 is the only impurity that remains in an isotopically purified SmB_6 sample, so its role has also been studied in this context. [89] In one recent study, Ref. [92], presents transport results on both Eu and La doped SmB_6 samples. In their floating zone grown doped samples, SmB_6-like transport behavior is observed up to a doping level of 5%. The authors note that the low-temperature plateau value decreases when dopants are added at a level of a few percent. They also draw a similarlity between Eu and Gd doping, where the plateau is not as strong when magnetic dopants are used.

To further investigate the role of defects in SmB_6, samples doped with La^{3+} and Eu^{2+} are presented here. The La-doped sample contained 3% lanthanum, and the Eu-doped sample contained 2.85% europium; both were grown by the Al flux method. Both samples were prepared by polishing the front and back, and van der Pauw geometry was used to characterize both samples. In the Eu-doped sample, after the first measurement, the sample was thinned from 500μm to 100μm and measured a second time.

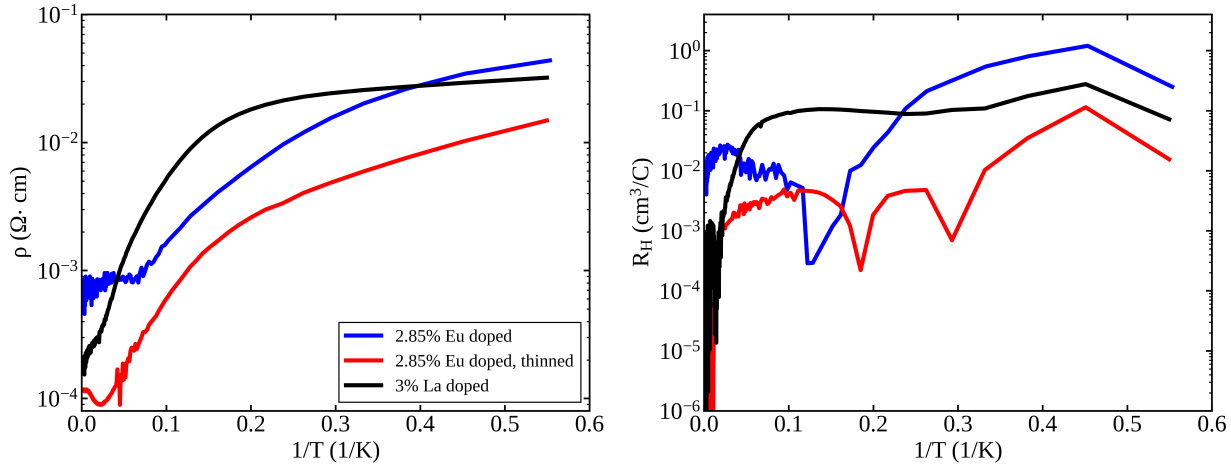

Figure 3.8: (a) Resistivity and (b) Hall coefficient on three doped SmB_6 samples.

Transport results on both samples are shown in Fig. 3.8. In the La-doped sample, the plateau is fairly horizontal as would be expected for an undoped SmB_6 sample, but the resistivity value is lower in comparison. The Eu-doped sample, both before and after thinning, the data does not show a true plateau, mirroring the Standard measurements of the floating zone samples, particularly in Figs. 3.4(b) and (c). The similarity between doped samples and floating zone results suggests that floating zone samples suffer from impurities, and that doped samples grown by the flux method are most similar to floating zone samples. We also note that thinning the Eu-doped sample increased the low temperature resistivity, as expected from polishing. In many of the Eu-doped samples from this batch, polycrystals were visible by eye, so particularly for this sample, thinning likely removed grain boundaries and other crystal defects, resulting in a higher quality measurement surface.

Above about 5 K, where bulk conduction dominates, Fig. 3.8(a) shows activated behavior, meaning that the bulk is still insulating despite the presence of impurities. In Fig. 3.8(b), the high temperature "bump" feature seen in the Hall results is characteristic of all Hall results on SmB_6 and is due to skew scattering before the Kondo gap opens. [129] These effects are likely unchanged compared to a pure sample, particularly in the La-doped sample, as the intentional doping concentration is low, although these samples' concentrations are much higher than unintentional doping due to impurities in the starting materials. In the Eu-doped samples, both the resistivity and Hall features are smeared, perhaps due to

screening of the Kondo effect by magnetic impurities, and thinning improves the clarity of these features.

3.6 Discussion and Conclusion

In this chapter, we reviewed inverted resistance measurements which establish that stoichiometric Al–flux SmB_6 remains a true Kondo insulator to at least 2 K, with a linear thermally activated behavior shown in the bulk resistivity. In contrast, both off–stoichiometric flux crystals and every floating–zone specimen possess a residual bulk conduction channel that saturates at low temperature, as shown in Figs. 3.3 and 3.5, respectively. The magnitude and temperature dependence of this channel vary strongly among floating–zone samples, implicating growth–dependent disorder rather than an intrinsic electronic instability. Flux grown SmB_6 samples with added vacancies and La and Eu dopants reproduced key features of floating zone samples, supporting the view that even modest impurity concentrations generate or amplify extended defects. Most importantly, a high-quality flux-grown sample should always be preferred over a floating zone sample. A high-quality flux-grown sample is immune to point defects, and the truly insulating bulk also sets SmB_6 apart from band TIs like Bi_2Se_3, which are all degenerate bulk conductors.

Complementary micro-hardness testing and chemical-etch imaging reveal a markedly higher density of extended defects in floating–zone material. Square etch pits, aligned with the cubic axes, confirm that dislocations and related line defects permeate these crystals. The Skinner impurity-band model can reproduce part of the low-temperature conductivity, yet point defects alone cannot account for the large conductance observed. One-dimensional paths along dislocations therefore provide a credible parallel network that shorts the insulating bulk and masks surface-state transport.

These findings reconcile disparate reports on SmB_6 by showing that the material's apparent ground state hinges on its defect characteristics. Only crystals with stringent control of stoichiometry and minimal dislocation density exhibit textbook topological Kondo insulator behavior. Future efforts should refine floating–zone parameters, directly image dislocation networks, and couple transport with thermal and spectroscopic probes to quantify the inter-

play of impurities, dislocations, and topological surface states.

Chapter 4

Ionic Liquid Gating

4.1 Motivation

Characterizing the electrically conductive, and potentially topological, surface states of samarium hexaboride (SmB_6) has become a central theme in the recent literature on Kondo insulators. As already outlined in Chapter 1, the low-temperature surface conduction in SmB6 arises from three distinct Fermi-surface pockets: one pocket resides at the Γpoint of the surface Brillouin zone, and two symmetry-related pockets reside at the X points of the (001) surface Brillouin zone. These electronic reservoirs are frequently referred to as the Γ pocket and the X pockets (or 2X pockets). Although electrons from both pockets participate in transport, they do so in markedly different proportions. The X pocket possesses a substantially larger carrier density than its Γ counterpart, yet the Γ pocket exhibits the higher mobility. A reliable quantitative determination of the carrier density (n) and mobility (μ) in each pocket is therefore essential for understanding the unusual low-temperature properties of SmB_6 and for clarifying whether its surface states are indeed topologically protected.

A variety of measurement techniques have been applied in pursuit of these parameters. Magnetotransport using Hall bar lithography, magnetotransport on Corbino disks, torque magnetometry, quantum oscillations, angle-resolved photoemission spectroscopy (ARPES), and optical probes have each provided partial information. However, as discussed in more detail in Chapter 1, results obtained by the different techniques remain in considerable

disagreement. One recurring difficulty is that experiments often fail to isolate the signal from a single crystallographic surface; unintentionally, they collect contributions from multiple surfaces or even from subsurface defects. Even when measurements are constrained to one surface, the X pockets, having higher carrier concentrations, usually dominate the transport signal, which further complicates an independent examination of the Γ pocket.

Among the recent attempts to pin down transport parameters, the study by Eo et al. is particularly instructive. That work exploited the Corbino disk geometry, patterned directly on an optically polished (001) facet of a bulk single crystal of SmB_6. Because the Corbino arrangement employs a concentric contact design, current is restricted to flow within the single surface on which the pattern is fabricated; bulk paths and edge shunts are strongly suppressed. By analyzing the temperature and field dependence of the low-temperature surface resistance, Eo et al. generated estimates for the carrier densities and mobilities of both the Γ and X surface pockets. Furthermore, their discussion suggested that the Corbino disk provides the optimum configuration for studying surface states, whereas the conventional Hall bar was argued to be more suitable for investigations emphasizing bulk contributions.

The present chapter revisits that conclusion. Our experimental program extends the work of Eo et al. by fabricating and measuring Hall bars, carefully incorporating the role of subsurface cracks and polishing-induced damage layers that may support additional conductive paths. In a Hall bar, both the longitudinal resistivity ρ_{xx} and the transverse (Hall) resistivity ρ_{xy} can be measured simultaneously, allowing independent determination of the Hall conductivity σ_{xy} and the longitudinal conductivity σ_{xx}. Intriguingly, as we shall show, crack-related conduction on hidden interior surfaces can be disentangled in the Hall bar format by combining these two resistivity channels. When that contribution is subtracted, the Hall bar becomes a powerful, surface-sensitive probe whose capability was under-appreciated in earlier analyses. In fact, the functional dependence of σ_{xy} on the microscopic parameters is proportional to μ^2, so the pocket with the highest mobility, rather than the pocket with the largest carrier density, dominates σ_{xy}. In SmB_6 that condition places the Γ pocket in the foreground, providing an experimental pathway to a pocket that is notoriously difficult to access by other means. Additional insight can be obtained by electrostatically tuning the surface carrier density through gating. Unlike in thin-film semiconductors or two-dimensional

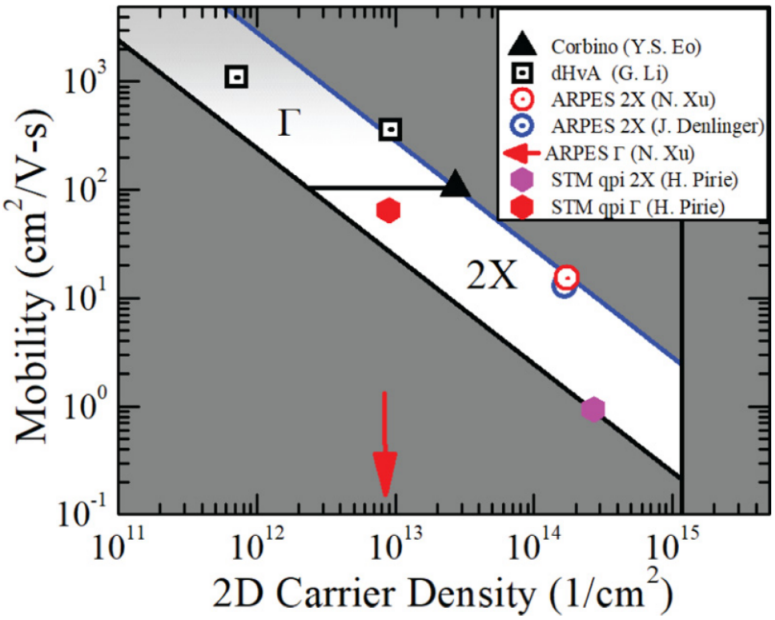

Figure 4.1: Constructed parameter space with three fundamental limits and experimental data, following Ref. [88]

electron gases (2DEGs), where metallic gating separated from the active layer by a dielectric is used, we employ a liquid gate to enable uniform gating of all crystal surfaces of SmB_6.

4.2 Understanding the Parameter Space

To place the above discussion in a rigorous framework, we seek to map the allowed ranges of n and μ for each surface pocket in SmB_6 into a "parameter space." Fig. 4.1 summarizes the resulting landscape, with the shaded regions being excluded based on theoretical boundaries and experimental reports.

The darkly shaded region on the right marks the limit imposed by the surface Brillouin zone. Known as the k_F limit, the total population of the pockets cannot exceed the maximum density corresponding to filling the entire Brillouin zone. For SmB_6, the surface Brillouin zone equates to a carrier density of 1.17×10^{15} cm^{-2}, so any experimental data point falling to the right of that vertical boundary would be incompatible with simple band filling arguments.

A second constraint, displayed as a low-density shaded triangle in the lower left of Fig.

4.1, stems from the Ioffe-Regel limit. In two dimensions, when the mean free path falls below the lattice spacing, the system crosses from a metallic state to a localized or insulating state. The criterion translates to $\sigma_{xx} \approx e^2/h$. Had the surface resistivity of SmB_6 exceeded that threshold, the transport would have turned nonmetallic, in contradiction to the experimentally observed residual metallic conduction.

A third, somewhat softer boundary arises from the absence of Shubnikov–de Haas oscillations in fields up to 80 T. The field B_q at which oscillations become visible satisfies $B_q \approx \hbar/2\pi e \ \mathrm{kF}/\mu$, so the higher the mobility, the lower the onset field. Because oscillations are not seen at 80 T, mobility must remain below the line that corresponds to $B_q = 80$ T. This requirement appears as a slanted gradient shading in the upper left portion of the figure.

Nearly all Hall bar extractions of n and μ in the literature land at densities of order 10^{15} cm^{-2} or greater, clearly violating the Brillouin-zone limit. Although often quoted, those numbers must be interpreted cautiously, because the Hall bar typically probes all six faces plus additional interior surfaces, rather than a single crystallographic face. The Corbino disk measurement by Eo et al., [88] represented in Fig. 4.1 as a triangular symbol, occupies a location well inside the allowed region. The diagonal line extending upward from the Corbino data point in Fig. 4.1 represents an upper bound on the total conductivity extracted from that measurement. Using theoretical considerations and ARPES inputs, Eo et al. further partitioned the permitted parameter space into sub-regions attributable to the Γ pocket and the 2X pockets. The authors' best estimate for the Γ pocket centered at $n \approx 8 \times 10^{12}$ cm^{-2} with $\mu \approx 170$ $\mathrm{cm}^2\ \mathrm{V}^{-1}\ \mathrm{s}^{-1}$, represented in Fig. 4.1 as a red arrow. The 2X pockets were attributed roughly to $n \approx 2 \times 10^{14}$ cm^{-2} and $\mu \approx 10$ $\mathrm{cm}^2\ \mathrm{V}^{-1}\ \mathrm{s}^{-1}$. If the Γ and X pockets each contribute comparably to σ_{xx}, then one pocket must supply carriers at higher density but lower mobility, while the other contributes lower density but higher mobility, consistent with the two-component partition just described. Figure 4.1 also shows measurements from dHvA quantum oscillations, [83] two reports from ARPES, [68, 62] and STM quasiparticle interference (QPI), [74] which all fall in the allowed regions.

4.3 Role of Subsurface Cracks

A remaining source of uncertainty involves the presence of subsurface cracks and polishing-induced microvoids. Even meticulous mechanical polishing with abrasives down to 0.3 μm grain size does not eliminate buried damage entirely. Such cracks effectively create additional conductive surfaces, and current can meander through these internal pathways. Because the exact morphology of every crack is unknown, a direct calculation of its contribution to the measured conductance is impossible. Nevertheless, by combining measurements that are differently sensitive to such pathways, one can deduce and subtract their effect. We demonstrate that a Hall bar patterned on a carefully polished SmB_6 crystal allows this subtraction by exploiting the fact that subsurface cracks provide parallel current paths that predominantly influence σ_{xx}, whereas σ_{xy} is less affected because Hall voltages generated in different planes partially cancel. A detailed comparison of ρ_{xx} and ρ_{xy} over temperature and field then separates the genuine surface signal from the spurious crack contribution.

To review from Chapter 2, in a standard analysis including a magnetic field in the z-direction, the carrier density and mobility are extracted from the x-y conductivity matrix,

$$\sigma = \begin{pmatrix} ne\mu & ne\mu^2 B \\ -ne\mu^2 B & ne\mu \end{pmatrix} \tag{4.1}$$

where n is the carrier density, μ is the mobility, e is the electric charge, and B is the magnetic field. The longitudinal and transverse resistivity are

$$\begin{aligned} \rho_{xx} &= \frac{1}{ne\mu} \\ \rho_{xy} &= -\frac{B}{ne}. \end{aligned} \tag{4.2}$$

Then, carrier density can be found from ρ_{xy} and mobility from n and ρ_{xx}. As discussed above, most Hall results on SmB_6 yield surface carrier densities of order 10^{15} cm^{-2} or higher, Polishing the surface can reduce the carrier density, but not enough to push it below the k_F limit.

To account for subsurface cracks, a second channel (σ_{cr}) can be added to the conductivity

matrix. It is only included in the diagonal elements, since the subsurface cracks are oriented randomly within the sample, and thus it is assumed they will not contribute to the Hall effect. The new conductivity matrix becomes

$$\begin{pmatrix} ne\mu + \sigma_{\rm cr} & ne\mu^2 B \\ -ne\mu^2 B & ne\mu + \sigma_{\rm cr} \end{pmatrix}. \tag{4.3}$$

Following the two-channel conductivity analysis presented in Chapter 2, with $\mu^2 B^2 << 1$, we find that

$$\begin{aligned} \rho_{xx} &= \frac{1}{ne\mu + \sigma_{cr}} \\ \rho_{xy} &= \frac{ne\mu^2 B}{(ne\mu + \sigma_{cr})^2}. \end{aligned} \tag{4.4}$$

The results, with cracks, for the longitudinal and transverse resistance are

$$\begin{aligned} \rho_{xx} &= \frac{1}{ne\mu}\left(\frac{1}{1 + \sigma_{\rm cr}/(ne\mu)}\right) \\ \rho_{xy} &= \frac{B}{ne}\left(\frac{1}{1 + \sigma_{\rm cr}/(ne\mu)}\right)^2. \end{aligned} \tag{4.5}$$

These new expressions are both modified from Eq. 4.2 by the same factor, $\sigma_{\rm cr}$, containing the conductivity of the cracks. By dividing the two equations, we can obtain a crack-independent quantity,

$$\frac{\rho_{xy}}{\rho_{xx}^2} = ne\mu^2 B. \tag{4.6}$$

This crack-independent quantity is equal to the off-diagonal term in the conductivity matrix, or σ_{xy}. Thus, we show that

$$\sigma_{xy} = ne\mu^2 B. \tag{4.7}$$

In the case of multiple channels the term on the right hand side of Eq. 4.7 would simply be summed over all the channels. The new equation allows a relationship between the carrier density and mobility to be extracted from data, but the exact values of both cannot be determined independently from each other. The expression in Eq. 4.6 is general and could be applied to any surface conductor measured by Hall bar geometry, but it is especially

useful in materials where subsurface cracks are present.

To apply this analysis to the Γ and X pockets in SmB_6, we modify the equation for two channels:

$$\sigma_{xy} = n_\Gamma e\mu_\Gamma^2 B + n_{2X} e\mu_{2X}^2 B. \tag{4.8}$$

From Ref. [88], the Γ pocket has an estimated carrier density of 8×10^{12} cm^{-2} and mobility of 170 cm^2/V·s, while the X pockets have an estimated carrier density of 2×10^{14} cm^{-2} and mobility of 10 cm^2/V·s. This means that the Γ pocket, which has the higher mobility of the two surface pockets, dominates the Hall conductivity in SmB_6. Other methods like ARPES or quantum oscillations can more readily probe the X pocket, as it has a higher carrier density than the Γ pocket, but the Hall bar provides a powerful method for accessing the more elusive Γ pocket.

4.4 Ionic Liquid Gating

In 2DEGs, the standard approach to gating is to deposit a metallic top gate separated from the active layer by a dielectric thickness of order a few tens of nanometers. In SmB_6 a conventional metallic gate encounters two obstacles. First, the crystal typically has millimeter-scale thickness, so a planar top gate would only address one face of a larger three-dimensional specimen. Second, all crystallographic surfaces of SmB_6 support conducting states, so gating a single face does not enable a uniform change of carrier density throughout the surface network. Instead of a metallic gate, then, for materials with a large active region, ionic gating may be employed.

Ionic gating is an experimental technique in which an electric field is applied to a material through an electrolyte using a material wherein ions in the electrolyte are not fixed, such as an ionic liquid or an ion-gel. They comprise two large organic molecules with a weak ionic binding. [130]. An ionic liquid behaves as an electrolyte with negligible vapor pressure and very high electrochemical stability, and they are often employed in research involving large-capacitance devices for energy storage applications. [130, 131] When a potential is applied between an immersed gate electrode and the sample, mobile ions in the liquid migrate to form an electric double layer (EDL). A compact layer of opposite charge accumulates at the solid-

liquid interface, leading to extremely large areal capacitances, [132] sometimes exceeding tens of μF cm^{-2}, which translates to substantial carrier density modulation even when only a few volts are applied at the electrode. Because the liquid coats all accessible surfaces, the gate field targets the complete surface manifold of the crystal. Thus, the technique is especially sensitive to two-dimensional conduction channels. This enables systematic studies of how sheet resistance, Hall coefficients, and magnetoresistance evolve with carrier density. In electrical-transport studies, the large carrier density modulation provided by ionic gating allows for the moving of the Fermi level through different electronic bands, switching between insulating and metallic behaviors, and thus is an excellent method of mapping out phase diagrams and probing emergent phenomena that would otherwise require high doping or high pressures.

In our studies, the ionic liquid N,N-diethyl-N-methyl-N-(2-methoxyethyl) ammonium bis (trifluoromethylsulphonyl)imide (DEME TFSI) was used. DEME-TFSI presents several practical advantages for low-temperature transport studies. Its ionic conductivity remains high at room temperature, facilitating rapid equilibration of the EDL. It possesses minimal leakage in the cryogenic range, allowing the applied gate potential to remain stable during temperature sweeps. [133] The material undergoes a glass-like transition near 182 K. Below that temperature ion mobility is severely suppressed, so the EDL becomes effectively frozen. [132, 131] Consequently, all target gate voltages must be applied at or near room temperature, after which the system is cooled to the experimental base temperature while the double layer retains its charge configuration. DEME-TFSI tolerates relatively large biases (approximately 2 V to 3 V) before electrochemical decomposition is likely. [131] Nonetheless, the long-term effects of transient over-bias remain uncertain, and prudent practice limits the magnitude of the applied voltage to the lowest value that accomplishes the desired carrier modulation. DEME-TFSI may also have a finite response time when new voltage is applied, likely due to the size of the molecules hindering immediate movement. This liquid was previously used in Ref. [58] on SmB_6 with Corbino disk geometry.

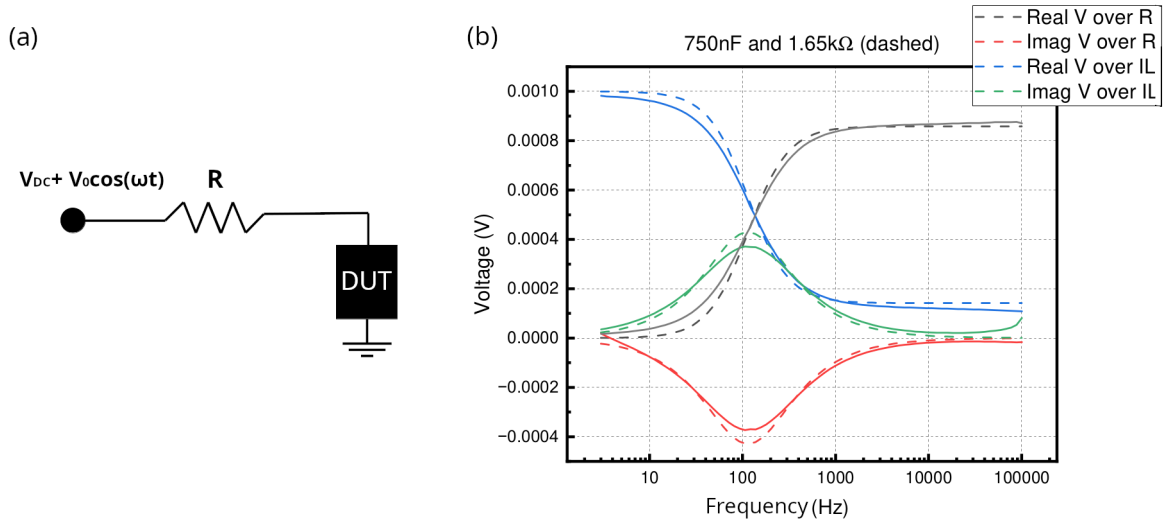

Figure 4.2: (a) The circuit diagram, alongside (b) plotted impedance spectroscopy.

4.4.1 Calibration on Copper Wire Electrode

A separate calibration, conducted with balled copper wires (two 1m and two 0.5m in length) partially immersed in the ionic liquid, determined the effective double-layer capacitance. A supplied voltage $V_{DC} + V_0 cos(\omega t)$ was applied to a wire and the frequency response of the ionic liquid was collected using impedance spectroscopy. The data was then analyzed using best-fit values which provided a resistance and capacitance for the ionic liquid, as seen in Fig. 4.2. In the figure, the solid lines represent the experimental impedance spectroscopy results, and the dashed lines represent a fit with a capacitance of 750 nF and a resistance of 1.65 kΩ. These values are then used with a known mobility of ≈150 $cm^2\ V^{-1}\ s^{-1}$ to directly map the applied gate bias to the induced surface charge density, yielding a correction of 5 $\times 10^{12}$ cm^{-2}/V to 7.5 $\times 10^{12}$ cm^{-2}/V.

4.5 Ionic Liquid Gating on SmB_6

Beyond passive characterization, ionic liquid gating affords dynamic control of the surface electronic structure. Our gating setup employs a Hall bar fabricated by electron-beam lithography and Ti/Au metallization on an SmB6 crystal that was grown by the aluminum flux method. To avoid contamination from residual aluminum inclusions, the crystal was me-

chanically thinned, then polished on all four Hall bar faces using increasingly fine abrasive media down to 0.3 μm. The sample dimensions were 2.5 mm in length between current contacts, 650 μm width, and 175 μm thickness. Electrical contacts were initially attempted with silver epoxy, but the differential thermal contraction at the glassy transition of DEME-TFSI led to bond failure. Instead, we adopted indium solder pads coupled to gold wires, which proved mechanically robust across multiple temperature cycles.

The sample is mounted on a miniature silicon boat purpose-built to expose all faces to the ionic liquid. An indium wire immersed in the liquid serves as the gate electrode. Before measurements, a droplet of freshly prepared DEME-TFSI is dispensed onto the cooled-down assembly inside an argon-purged glove box, then the entire stage is transferred into a Quantum Design Dynacool Physical Property Measurement System (PPMS) that provides magnetic fields up to 14 T and temperature control from 300 K to 1.8 K. Magnetic fields up to $\pm$ 10 T and gate voltages from -2 V to $+2$ V were tested. Although the capacitance extracted from the copper-wire calibration would in principle support even larger changes in carrier density, the simultaneous requirement to avoid electrochemical degradation and the practical limits of the PPMS wiring constrained the voltage window investigated in this study. Following the guidance of previous studies, we ramped the gate voltage in incremental steps of 0.5 V, adopting the sequence +0.5 V, +1 V, +1.5 V, +2 V, then resetting to 0 V and repeating the sequence for negative biases. Due to the finite ionic relaxation time, achieving a well-defined EDL required holding the gate voltage constant at room temperature for 30 minutes prior to cooling. Between the positive and negative applied voltage sweeps the system was left overnight at zero gate bias, ensuring complete discharge of any trapped space charge in the liquid or at the sample interface. Each voltage was also applied at zero magnetic field; for Hall effect measurements the field was applied below the glassy transition temperature to avoid any possible magnetic effects on the ions in the liquid, which are not previously reported. Transport measurements employed a Stanford Research Systems SR830 lock-in amplifier. Longitudinal and Hall resistivities were recorded as a function of magnetic field at each stabilized gate voltage.

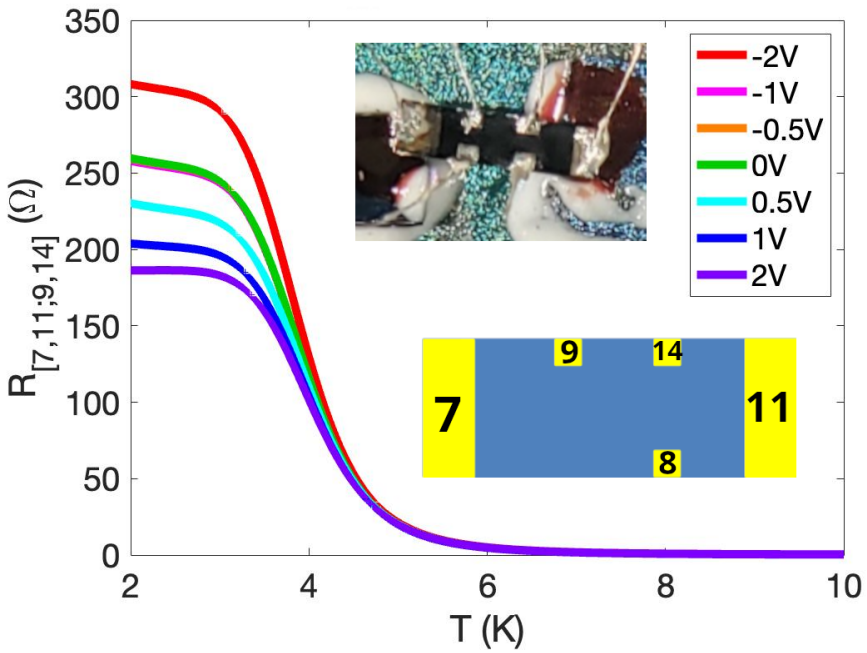

Figure 4.3: Longitudinal resistance vs. temperature at various voltages applied to the ionic liquid.

4.6 Results and Discussion

Consistent with expectations from the gating-induced change in carrier density, we observed systematic shifts in the slope of $\rho_{xy}(B)$ and concomitant modifications of the low-temperature plateau in ρ_{xx}. Results for the longitudinal resistance R_{xx} are shown in Fig. 4.3. The insets show the mounted sample immediately before applying the ionic liquid, as well as a schematic of the Hall bar setup used, with the measurement $R_{7,11;9,14}$ representing the R_{xx} measurement. The resistance was found to vary by more than 100 Ω over the voltage range tested. The qualitative results agree with Ref. [58] in that negative applied voltage increases the resistance plateau and positive voltage decreases the plateau. However, using our Hall bar geometry, we were able to tune the resistance plateau by about 70% compared to about 30% tuning on a Corbino geometry in Ref. [58].

The Hall coefficient as a function of magnetic field is shown in Fig. 4.4(a). Referring to the inset in Fig. 4.3, the transverse measurement $R_{7,11;8,14}$ represents R_{xy}. The Hall coefficient traces are identical, as expected, at temperatures where bulk conduction dominates. Beginning with the characteristic 4 K feature in the Hall coefficient, the effects of gating on

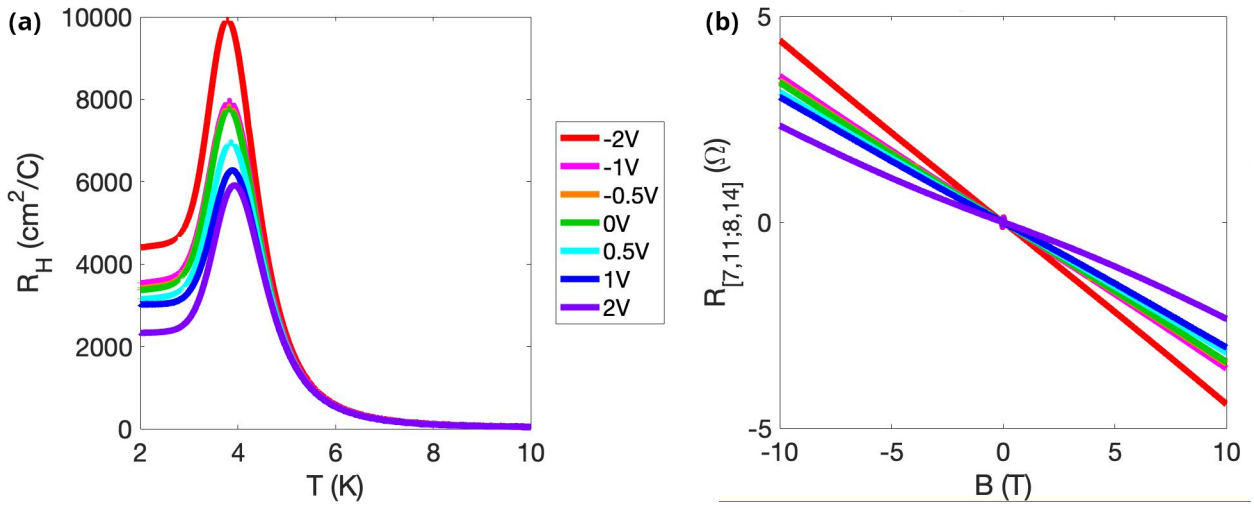

Figure 4.4: (a) Hall coefficient and (b) transverse resistance vs. magnetic field at various voltages applied to the ionic liquid.

the surface Hall coefficient can be observed. Using the COMSOL simulation, the magnitude of this feature is found to be proportional to the ratio $\rho_{bulk}/\rho_{surface}$.

R_{xy} as a function of magnetic field is shown in Fig. 4.4(b). For applied voltages up to 2 V, the traces are linear, as expected, but at 2V applied, there is a nonlinear feature. Magnetoresistance was also measured to understand this feature, and a plot of R_{xx} as a function of magnetic field is shown in Fig. 4.5. The magnetoresistance does not change significantly over the range of magnetic fields measured.

The results in Fig. 4.4 along with the method discussed earlier in this chapter were used to calculate $\sigma_{xy}/(eB)$, which, following Eq. 4.7, is based solely on carrier density n and mobility μ. The data were antisymmetrized and the contact correction described in Chapter 2 was applied. One value for the quantity $n\mu^2$ for each trace in Fig. 4.4 was obtained, and these results are shown in Fig. 4.6. The data were fitted to obtain a value for $n\mu^2$ at 0 V, 4.82 $\times 10^{16}$ cm^2/V$^2\cdot$ s^2.

This value was plotted on the parameter space from Fig. 4.1 as a line, displayed in Fig. 4.7. As the Hall bar measures the Γ pocket, we compare to the Γ reports from the literature. The new value agrees exactly with the QPI result for the Γ pocket. [74]

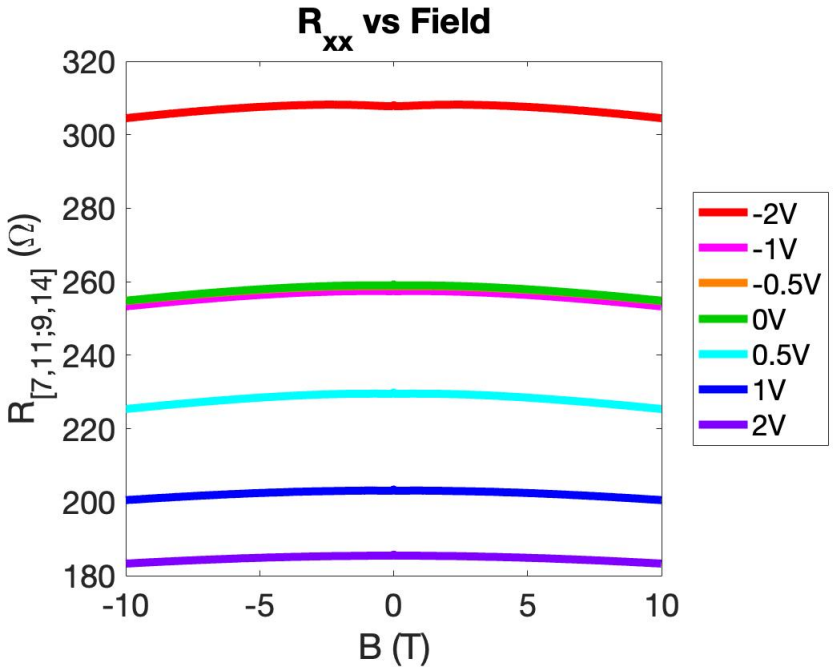

Figure 4.5: Magnetoresistance at various voltages applied to the ionic liquid.

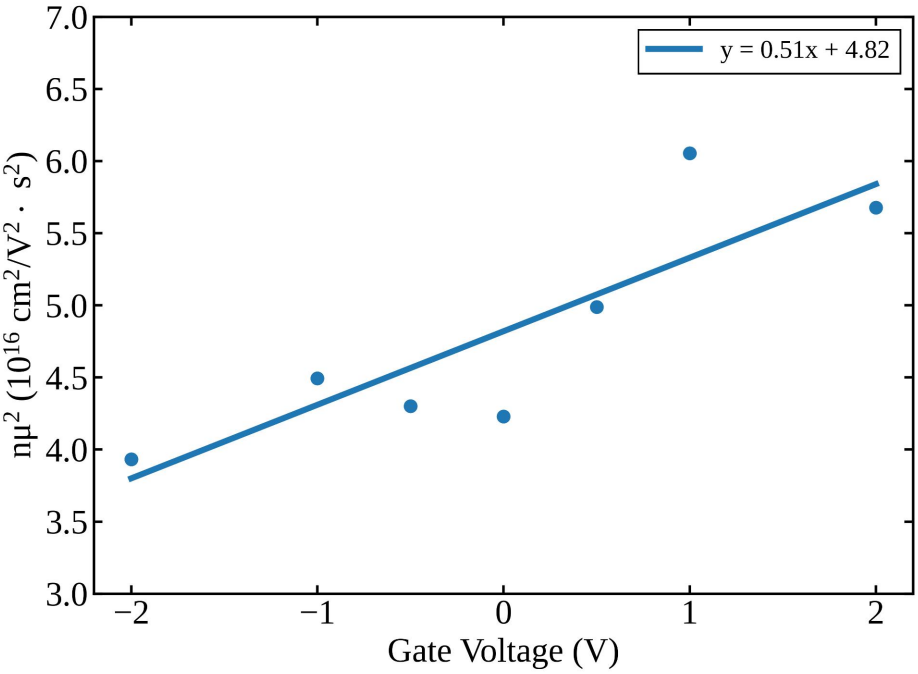

Figure 4.6: Extracted crack-independent quantity based on Eq. 4.7 with a line of best fit indicating the tunability of carrier density and mobility with gate voltage.

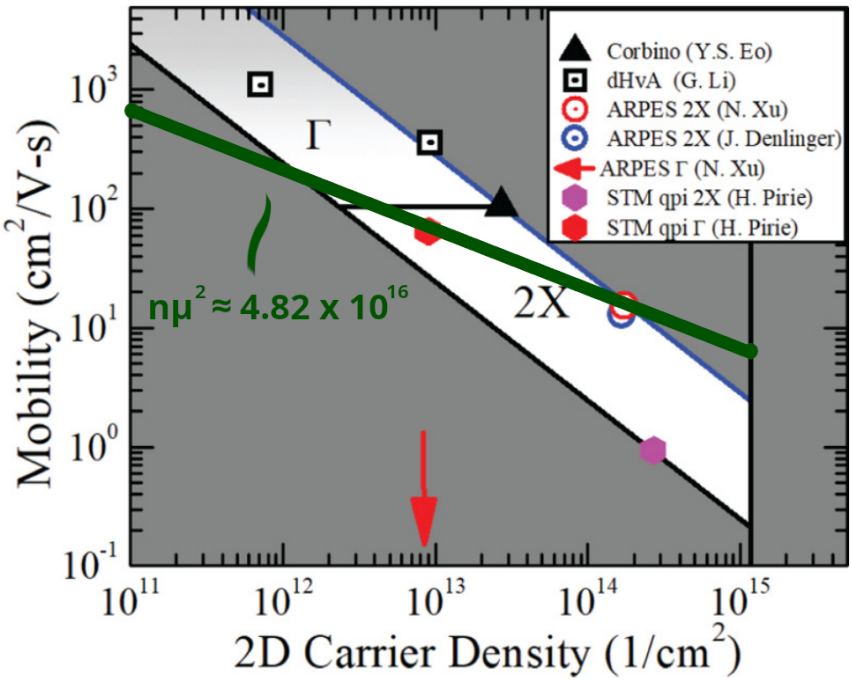

Figure 4.7: Ionic liquid result (green line) superimposed on the parameter space shown in Fig. 4.1, showing agreement with QPI Γ pocket results.

4.7 Conclusion

In this chapter, surface studies on SmB_6 were discussed. The current understanding of the surface state based on fundamental parameters and experimental results were discussed and used to form a parameter space for the carrier density and mobility of the Γ and 2X pockets. Hall bar results are known to exceed fundamental limits in reports of carrier density, so the role of subsurface cracks as an additional provider of surface conduction was discussed for Hall bar geometry. Even when cracks are present, we show that the Hall conductivity is independent of crack conduction, and analysis indicates that the Γ pocket density can be tuned within a limited but measurable range by applying gate voltages of up to ±2 V.

To tune surface conduction and obtain transport parameters, ionic liquid gating was performed on a Hall bar. The range of voltages from −2 V to +2 V allows for tuning of the resistance plateau by 70%. The Hall conductivity was used to obtain an additional constraint for the parameter space. This constraint agrees exactly with the STM quasiparticle

interference results for the Γ pocket. This result is especially exciting because $SmmB_6$ results rarely agree among experimental methods. An interesting avenue for future study, in light of the results presented in Chapter 3, would be to perform ionic liquid gating on floating zone samples to better understand the origin of surface conduction in these samples.

Chapter 5

Strain Studies

5.1 Introduction

Strain engineering is an experimental technique involving the application of controlled mechanical forces to a crystalline sample. The aim is to deform the underlying lattice, which can be achieved through stretching (tensile strain) or compressing (compressive strain) along specific crystallographic axes. This technique differs from hydrostatic pressure, wherein the entire crystal is compressed isotropically, and offers a more directional, targeted method to modulate material properties.

The motivation for strain studies originates from the remarkable sensitivity of electronic states in solids to lattice parameters. Electron orbital overlap is greatly affected by both lattice spacing and symmetry; consequently, even a fractional change in these values can induce substantial modifications in the band structure. As a result, material characteristics such as carrier density, mobility, and even the existence of energy gaps for electronic excitations can be tuned with relative precision via strain.

Historically, strain and pressure have played pivotal roles in elucidating the nature of correlated electron systems and phase transitions, especially in materials exhibiting mixed valence states or Kondo insulating behavior. For studies of SmB_6, application of hydrostatic pressure was shown to induce a transition from a Kondo insulating state to a metallic mixed valence phase.[31, 134, 33] Despite differences in the pressure at which it occurs, these early

experiments demonstrated that the gap attributed to Kondo hybridization could be suppressed by applying pressure to tune interatomic distances, confirming the delicate interplay of interactions.

Uniaxial strain experiments, in contrast to hydrostatic pressure, allow for fine-tuning of phase transitions along selected lattice directions, offering the possibility to probe anisotropy and symmetry-resolved phenomena. In topological materials such as SmB_6, strain emerges as an especially valuable probe. It not only influences bulk electronic properties like the Kondo gap, but it can also modify surface states, which are protected due to topological considerations. A central question in the study of topological insulators is the robustness of surface conduction against perturbations such as strain, and whether strain can drive a transition between topologically nontrivial and trivial phases by inverting electronic bands. In particular, one open question is whether the application of strain can induce a topologically protected state to dominate at a higher temperature than in the unstrained material.

Recent work by Stern et al. [135], observed the persistence of surface conduction in SmB_6 under uniaxial strain along the (100) direction up to temperatures as high as 240 K, far above the previously accepted temperature range for robust surface behavior (<4 K). This study also reports tuning of resistance from 0.1 to 800 Ω with up to 0.8% strain, as well as hysteresis in the bulk resistance as strain is applied and removed at temperatures above 3 K. The results reported by Stern, et al. are shown in Fig. 5.1. No studies since then have been able to replicate the findings, nor do the reported ranges of the tensile strain achieved seem viable given the hardness of SmB_6, as reported in Chapter 3. Micro-cracking, which even if not readily visible, could have artificially enhanced the conductivity via additional conduction paths. [108] This uncertainty motivates further experiments to reproduce the persistence of the surface conduction observed and critically assess the impact of strain on surface and bulk conduction in SmB_6, as well as to establish a clearer connection between mechanical deformation and electronic state evolution.

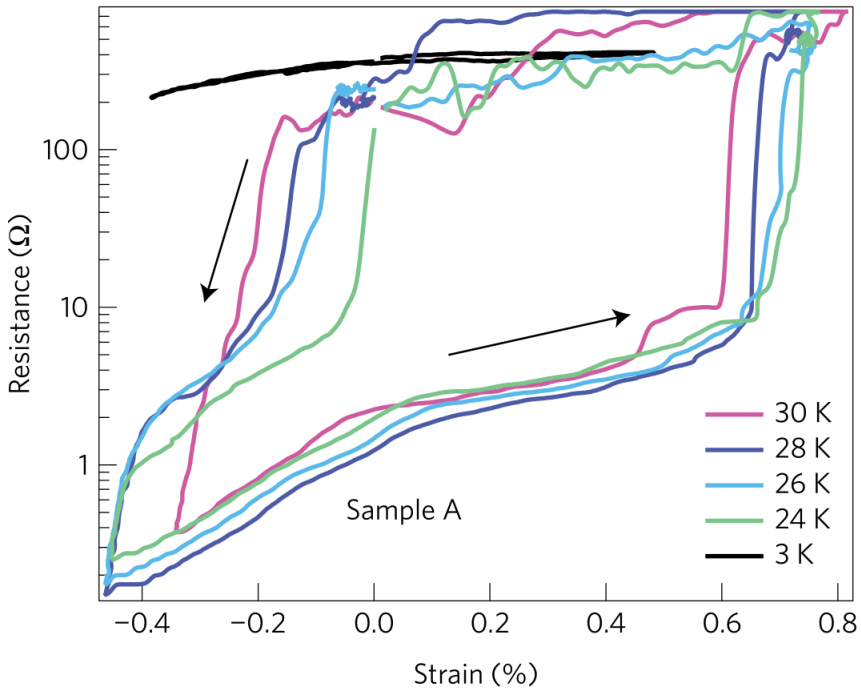

Figure 5.1: Hysteresis and surface conduction persisting up to 240 K as reported in Stern, et al. [135].

5.2 Strain Experiment

5.2.1 Piezoelectric-Based Strain Device

For the current investigation, a piezoelectric stack-driven strain apparatus was selected due to its capacity for precise, tunable control of uniaxial stress. [136] Piezoelectric actuators operate by expanding or contracting in response to an applied voltage, thereby imparting mechanical deformation with high spatial resolution. The system allows for both tensile and compressive strain to be dynamically applied and modulated during the experiment. In the present experiment, the Razorbill Instruments FC100 system was utilized as it can be easily integrated into the Quantum Design Physical Property Measurement System (PPMS).

A schematic diagram of the piezoelectric device and a representative photograph of the wired setup with a SmB_6 mounted are presented in Fig. 5.2. The sample of SmB_6 is placed across the gap on top of the mounting plates and attached via Stycast 2850FT epoxy. The plates are themselves attached to the piezoelectric stacks, which expand and contract upon

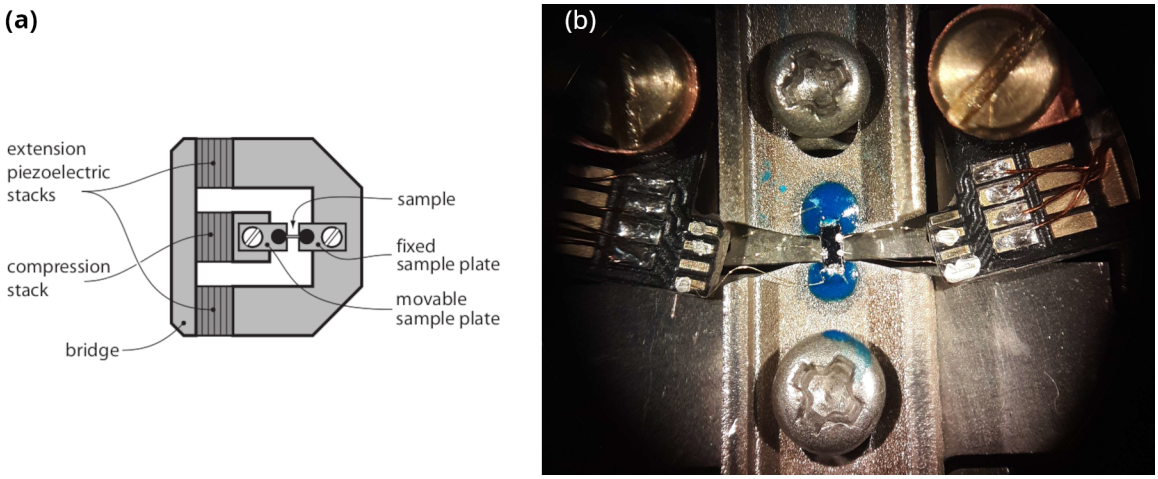

Figure 5.2: (a) Schematic diagram of a piezoelectric strain device as detailed in Hicks et al.[136], and (b) photograph of the wired setup with mounted SmB_6 sample.

electrical actuation. Proper alignment and securing of the sample is crucial to ensure uniform and reproducible strain along the intended crystallographic axis whilst avoiding the risk of shearing the sample.

Calibration of the strain device is essential for translating applied voltages into quantifiable strain values. The manufacturer provides conversion factors based on actuator displacement and the device's mechanical geometry. Additional refinement and zero-point corrections are often necessary. In our experiments, calibration was performed using a combination of device specifications and in-situ measurements. The latter involved monitoring both the actuator displacement via a capacitance reading, and sample resistance to confirm that the temperature behavior matched what was expected and that the applied voltage matched expected strain.

5.2.2 Experimental Preparation and Challenges

One of the most significant challenges in conducting strain experiments on hard and brittle materials like SmB_6 is preventing mechanical damage during the setup and while experimenting. This is especially the case with thinned samples with thicknesses around 100 $/mu$m, which are easily susceptible to snapping. Sample mounting must provide mechanical rigidity that avoids initiating cracks, especially at the sample edges where stress concentrations are highest. Epoxy was used to mount the sample, but its application was carefully done on

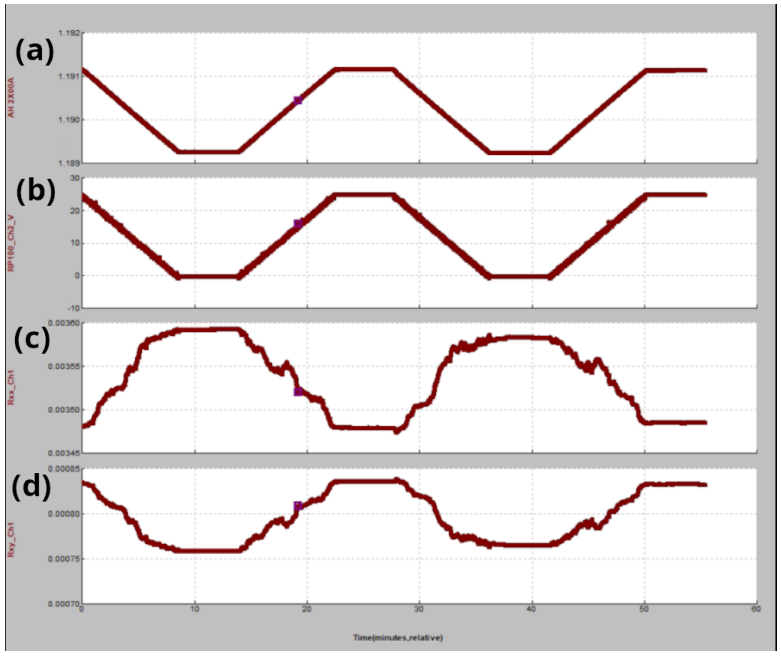

Figure 5.3: Example of in situ monitoring of strain application as a function of time, showing (a) strain voltage applied, (b) capacitance output, (c)R_{xx} output, and (d) R_{xy} output.

both ends to avoid epoxy seepage along the bottom or edges prior to curing. Epoxy on the bottom or edges would increase the chances of shearing or uneven application of strain throughout the sample, as the leaked epoxy would provide unwanted mechanical stability.

Similarly to mounting, wiring was carried out with additional considerations towards sample brittleness. In initial experiment runs, wires were attached using silver paste as contacts can be made without pressure or heating. Unfortunately, these connections can be weak, and especially for the present experiment, wires broke off frequently during strain application. Subsequent experiment runs used indium contacts; although heat is required, the strength of the bond allows for more successful straining.

In most experiments, a Hall bar geometry was used, and it was mounted to allow strain to be applied along the longest dimension of the sample. In a few of the runs, an inverted resistance geometry was also used, and strain was applied uniaxially in the plane of the Corbino disk. For the data that will be presented below, the same stoichiometric Al-flux grown Hall bar sample used in the ionic liquid gating experiment from Chapter 4 was tested.

After wiring, the strain apparatus was loaded into the PPMS. DC transport measurements were performed using a Stanford Research Systems SR830 lock-in amplifier, and ca-

pacitance was monitored using an AH 2700A capacitance bridge. Strain was applied at temperatures below 50 K, and in some experiments, magnetic fields up to ± 14 T were applied. To apply strain, a range of positive and negative voltages was applied to the actuators, corresponding to compressive and tensile mechanical deformation, respectively. These voltages were selected based on both manufacturer recommendations and observed sample performance, although a maximum of ± 200 V was possible with the particular device used. For the data that will be presented, only ±50 V was applied in an effort to prevent damage to the sample.

Concurrently with strain application, electrical transport measurements were performed to monitor sharp changes in resistance and infer modifications to electronic structure. The sequence of strain ramping with measurement collection was carefully designed to reduce thermal and noise effects. After each strain value was reached, the device was allowed to sit and stabilize for 5 minutes, to account for possible piezo creep or relaxation phenomena, which can manifest as time-dependent drift in the applied strain. For some runs, strain was held constant and temperature or magnetic field was varied, and in others, strain was varied at a constant magnetic field and temperature. Particularly when strain was varied, the data was monitored for the expected changes in transport parameters, to ensure that strain was being applied correctly. An example of the in situ monitoring is shown in Fig. 5.3.

Over the course of 11 experiment attempts, SmB_6 crystals were found to be particularly susceptible to cracking and slippage. In some experiments, the sample and epoxy detached from the strain apparatus, so no strain was applied to the sample. In others, the epoxy deformed or shattered, so it was impossible to determine how much strain was being applied to the sample. Additionally, the brittleness of SmB_6 led to cracking, creating parallel conduction paths along the damaged regions and causing sudden and drastic changes in transport measurements. These issues necessitated careful ramping of the voltage applied to the piezos and careful monitoring of the data to ensure that no breakage had occurred. After performing the experiments, the samples were inspected carefully using microscopy to verify structural integrity. For the sample used in this chapter, the experiment resulted in horizontal cracks along both edges close to the epoxy. Some vertical cracks were also observed along the length of the Hall bar. The sample was then re-polished to remove the cracks and

Trial	Sample	Geometry	Outcome
1	A	Hall bar	Wiring disconnected, no strain data acquired
2	A	Hall bar	Wiring shorted on initial strain application
3	A	Hall bar	50 V applied; epoxy found to be malleable
4	A	Hall bar	50 V applied; sample found to be broken lengthwise
5	B	Hall bar	Up to 125 V applied; epoxy broken, leaving sample to move around
6	B	Hall bar	Up to 125 V applied; data was noise and sample was sheared near center across the width
7	C	Hall bar	Up to 150 V applied; epoxy deformed, leaving sample to move around
8	C	Hall bar	Up to 50 V applied; data up to 20 V was usable but noisy. Sample found "cleaved" across the width at the ends near epoxy
9	C	Hall bar	Data presented in this chapter; data up to 50 V was usable and data from 50-150 V unusable. Epoxy shattered, leaving sample to move around
10	D	Corbino	Up to 120 V applied; cracks found in epoxy and sample
11	E	Hall bar	Run was aborted and sample cracked

Table 5.1: Summary of outcomes of each of 11 attempts to perform strain experiments on SmB_6. Sample C is the same sample used for ionic gating in Chapter 4, and Sample E is Sample S1 used in inverted resistance in Fig. 3.3.

measured again at lower applied strain to prevent further cracking. The challenges faced in each of the 11 experiment runs are summarized in Table 5.1.

5.2.3 Results

In the data presented here, the same stoichiometric flux grown SmB_6 used in the ionic gating measurements was subject to strain. Reliable results were collected up to voltages of ± 50 V, corresponding to maximum strains on the order of 0.11%. Within this threshold, only slight electronic modification was observed without catastrophic sample failure. Beyond ± 50 V, resistance traces were no longer consistent with repeated strain application patterns, often including increased resistance noise and sudden jumps when strain is applied.

The experiment showed that SmB_6 under uniaxial strain had a consistent response of the electronic properties to applied mechanical deformation. Fig. 5.4(a) displays the longitudinal

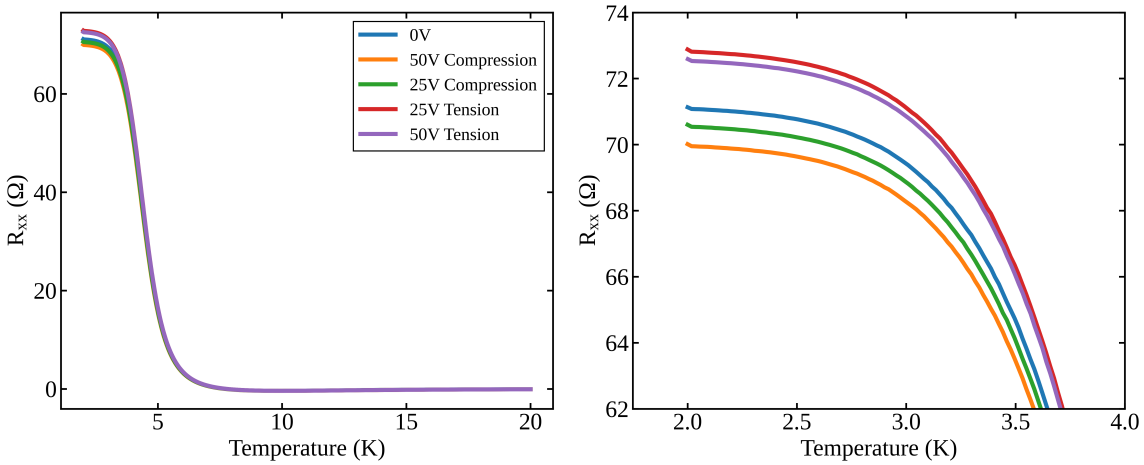

Figure 5.4: (a) Resistance versus temperature for strain conditions up to 50 V compression and tension, with (b) a zoom of the same data to show response of surface conduction to strain.

resistance versus temperature for five strain conditions in this experiment, with Fig. 5.4(b) as a zoom of the same data to show the tunability of the surface conduction with strain. Upon application of tensile strain, a very modest but noticeable increase in resistivity was observed at low temperatures, suggesting an amplification of the gap or a reduction in the carrier density/mobility. Conversely, compressive strain tended to decrease resistivity, which could be interpreted as an enhancement in carrier mobility or potential closure of the hybridization gap. In particular, as shown in the figure, a maximum resistance modulation of approximately 4% is achievable within the range of reliability. At temperatures where bulk conduction dominates, no discernible effect of strain is present.

Fig. 5.5 shows the transverse resistance versus magnetic field for the same modest strain conditions. As is apparent in the figure, strain applied parallel along the R_{xx} axis produced no discernible effect on the R_{xy} traces. This is perhaps expected as the uniaxially applied strain is deforming the crystal only in the longitudinal direction.

5.3 Discussion

The tunability of surface conduction with strain matches qualitatively with previous results. In Ref. [135], the application of uniaxial tension was found to increase the resistance below

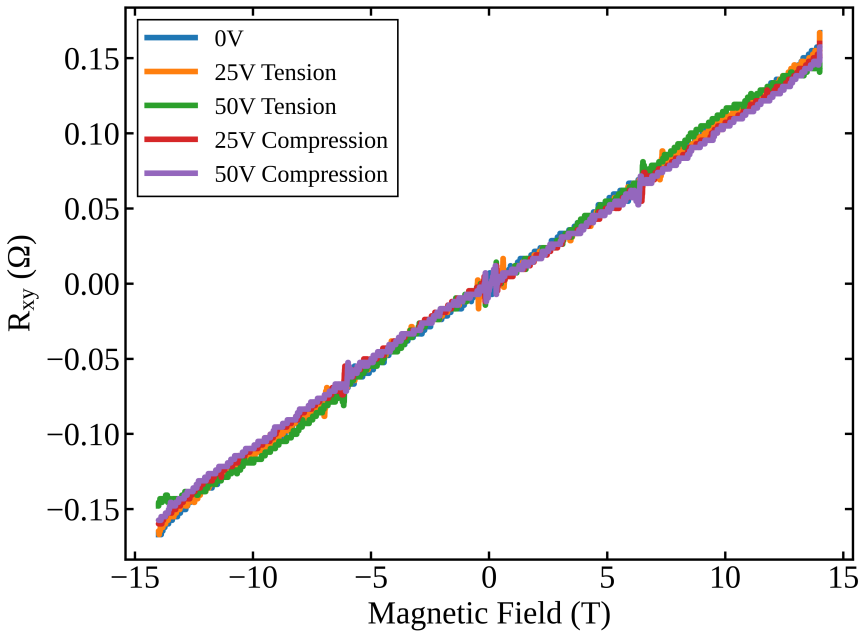

Figure 5.5: Transverse resistance (R_{xy}) versus magnetic field for various strain conditions at 2 K.

4 K, and the results presented here also show the same trend. Although uniaxial strain and hydrostatic pressure affect the crystal differently, hydrostatic pressure experiments show a decrease in resistance upon application of pressure, [31, 33] qualitatively matching the results presented here for uniaxial compression.

The present experiment also shows only a small tuning (4%) of surface resistance, while a much larger effect, over two orders of magnitude change, was seen in Stern, et al., Ref. [135]. No effect on resistance above 4 K was observed in our experiment, contrasting strongly with the observation of surface conduction up to 240 K in Ref. [135]. We were unable to reproduce any features, particularly the hysteresis in bulk resistance, above 4 K as reported in that reference. However, we note that at 3 K, Stern, et al. report minimal hysteresis, and their increase of resistance as compression is decreased and tension is applied does agree with our results.

Given that our experiment faced significant challenges to sample structure, including cracking, slippage, and breakage, it is possible that internal micro-cracking affected the results of Stern, et al. The epoxy in our experiment, which was also used by Ref. [135],

was also subject to cracking or becoming detached from the sample, and it is possible that cracks in the epoxy also affected their results. We were also not able to apply as much strain as in the reference. In Stern, et al., needle-like samples were chosen, and our best results out of 11 runs were performed on Hall bar shaped, needle-like samples. It is possible that a sample with smaller cross-sectional area than we used would allow for more strain to be applied, and for a greater tuning in resistance to be observed. A difficulty arises in that the SmB_6 sample must be thin enough to strain and to exert a meaningful force, while thick enough to be handled and to not snap or crack while mounting the sample or during straining. Additionally, one surface of the sample must be large enough to apply the appropriate transport geometry.

We also found that our crystals are hard and brittle. As reported in Chapter 3, pure, Al-flux grown SmB_6 is a very hard material, similar in hardness to diamond. While hardness and brittleness are not directly correlated, our observations of subsurface cracks, as well as samples that crack even under gentle polishing, especially when they are thinned, suggest that SmB_6 is extremely brittle under mechanical stresses. Although brittleness is not quantified in the same way as hardness, our observations are that SmB_6 is extremely brittle, making it difficult to strain. We also consider material parameters regarding compressibility. Young's modulus is most closely related to uniaxial strain, and to the best of the author's knowledge, there are no experimental reports of Young's modulus on SmB_6 in the literature. However, one report has noted that the bulk modulus of SmB_6 is approximately 90.5 GPa at 5 K [137], which is similar to metals like silver and brass. This would indicate that SmB_6 is somewhat compressible under hydrostatic pressure at the lowest temperatures.

5.4 Conclusion

In this chapter, results for uniaxial strain were presented on an Al-flux grown Hall bar. The resistance below 4 K was found to be tunable by 4% under 0.11% strain, and the bulk resistance above 4 K was not found to be tunable under the strains tested. Higher strain values yielded unusable data due to mechanical challenges in the epoxy or wiring and cracks in the sample. In contrast with Stern, et al., a strain of 0.8% could not be reached without

mechanical failure of the sample or epoxy. No surface conduction persisting to temperatures above 4 K was observed, and no hysteresis was found.

Additional strain measurements could be done with reduced width and thickness on the sample, but extra care must be taken with sample preparation and handling due to brittleness and susceptibility of the material to cracks. A purpose-built holder for the sample could be used to hold the sample end-to-end to avoid cracks and slippage in the epoxy, but for tension measurements, epoxy or another adhesive would be required.

Chapter 6

Conclusion and Outlook

6.1 Summary

In this work, comprehensive transport studies of the topological Kondo insulator SmB_6 were presented. Chapter 3 reviewed inverted resistance measurements on a double sided Corbino disk, which reveal that stoichiometric Al-flux-grown SmB_6 is a true bulk insulator at temperatures as low as 2 K, with a linear thermally activated behavior in the bulk resistivity. A high quality single crystal of Al-flux grown SmB_6 is immune to point defects in the bulk, setting SmB_6 apart from band TIs like Bi_2Se_3 or Bi_2Te_3, which are all degenerate bulk conductors.

Floating zone grown SmB_6, by contrast, possesses residual bulk conduction as revealed by inverted resistance measurements. The magnitude and temperature dependence of the residual conduction vary among floating–zone samples, implicating growth–dependent disorder. Flux grown SmB_6 samples with added vacancies and samples with La and Eu dopants reproduce this low-temperature feature of floating zone samples and support the origin of the conduction in disorder. However, point defects alone cannot account for the conduction. Chemical etching performed on both types of samples reveal a markedly higher density of extended defects in floating zone samples compared to flux grown, so one-dimensional paths along dislocations are found to short the insulating bulk and mask surface transport. Therefore, a high-quality, stoichiometric flux-grown sample should always be preferred over

a floating zone sample.

To complement these bulk studies, Chapter 4 presents work on the surface characteristics of SmB_6. A difficulty in studies of SmB_6 arises from the lack of agreement among experimental methods. Previous work to reconcile these results by constructing a parameter space for the carrier density and mobility of the surface pockets based on fundamental parameters and experimental results was summarized. In nearly all reports, the Hall bar results exceed fundamental limits in reports of carrier density, so the role of subsurface cracks as an additional surface conduction path was discussed. The Hall conductivity, σ_{xy}, is shown to be independent of crack conduction, and Hall bar geometry is found to be able to probe the higher mobility Γ pocket.

Ionic liquid gating was performed on Hall bar geometry on an Al-flux grown sample. The ionic liquid allows all surfaces to be gated at once, ensuring that the entire surface conduction channel is being tuned. Applied gate voltages from -2 V to $+2$ V allows for tuning of the resistance plateau by 70%. The obtained Hall conductivity was used to obtain an additional constraint for the Γ pocket in the parameter space. This constraint agrees exactly with the STM quasiparticle interference results for the Γ pocket, [74] and shows close agreement with ARPES as well.

Chapter 5 discusses uniaxial strain experiments on an Al-flux grown Hall bar. These studies were motivated by a recent report of extended surface conduction with a hysteresis feature up to 240 K. [135] In contrast to this reference, the results presented here found that the resistance below 4 K was tunable by only 4% under 0.11% strain, and the resistance above 4 K was not found to be tunable under the strains tested. No hysteresis in the bulk conduction, or surface conduction persisting to temperatures above 4 K, was observed, and the results presented in Stern, et al. were not reproduced. Attempts to apply greater strain to the sample did not yield usable data due to cracks in the sample and damage to the epoxy and wiring. Material parameters including hardness, brittleness, and elasticity constants were briefly discussed in relation to the challenges in applying strain.

6.2 Future Work and Open Questions

6.2.1 Impurities and Doping

Despite the attribution of many features of SmB_6 to impurities, not many systematic studies of impurities have been reported in the literature. While magnetic impurities, have been of interest in relation to Kondo symmetry breaking, studies on the interplay between dislocations and one-dimensional defects, both magnetic and nonmagnetic, provide an area for future research. The effect of one-dimensional defects that permeate through the sample from surface to surface is also of interest. Future studies imaging dislocation networks and quantifying conduction through these paths using thermal and spectroscopic probes could be performed. An investigation of floating zone samples in particular, to understand why they are so susceptible to bulk conduction, is necessary.

6.2.2 Surface Studies

In light of the result that floating zone samples are susceptible to bulk conduction, ionic liquid gating on floating zone samples could be performed to investigate whether the surface conduction can be tuned in the same way as in a flux-grown sample. If the effect is very different from the flux-grown results presented in this work, it would add evidence to the observation that floating zone grown samples differ significantly in their properties, perhaps even that floating zone samples are bulk conductors and do not host topologically protected surface states. This pattern is already present in the literature; most studies finding a topologically protected conduction are performed on flux-grown samples, while studies that argue for trivial conduction are performed on floating zone samples.

Additional strain measurements could also be performed, as the results presented in this work are preliminary. Uniaxial strain provides a complementary picture to the hydrostatic pressure reports in the literature. Further attempts to reproduce the results of Stern, et al. would be interesting given the dramatic result presented in that work. For future studies, a reduced cross-sectional area for the strained sample is recommended, while also taking care with sample handling due to brittleness and susceptibility of the material to cracks. For

compression measurements, a purpose-built holder for the sample could be used to secure the sample end-to-end to avoid cracks and slippage in the epoxy, but for tension measurements, epoxy or another adhesive would still be required.

Bibliography

[1] J. Kondo. Resistance minimum in dilute magnetic alloys. *Progress of Theoretical Physics*, 32:37, 1964.

[2] N. F. Mott. Rare earth compounds with mixed valencies. *Philosophical Magazine*, 30(2):403, 1974.

[3] G. Aeppli and Z. Fisk. Kondo Insulators. *Comments Cond. Mat. Phys.*, 16(3):155–165, 1992.

[4] H. C. Longuet-Higgins and M. de V. Roberts. The electronic structure of the borides MB_6. *Proceedings of the Royal Society A*, 224(1158):336–347, 1954.

[5] Yu. B. Paderno, V. I. Novikov, and E. S. Garf. Electrical properties of hexaborides of the alkaline- and rare-earth metals at low temperatures. *Poroshkovaya Metallurgiya*, 11(83):70–73, 1969.

[6] A. Menth, E. Buehler, and T. H. Geballe. Magnetic and semiconducting properties of SmB_6. *Physical Review Letters*, 22(7):295, 1969.

[7] J. W. Allen, B. Batlogg, and P. Wachter. Large low-temperature Hall effect and resistivity in mixed-valent SmB_6. *Physical Review B*, 20:4807, 1979.

[8] S. von Molnar, T. Theis, A. Benoit, A. Briggs, J. Flouquet, J. Ravex, and Z. Fisk. Study of the energy gap in single crystal SmB_6. In P. Wachter and H. Boppart, editors, *Valence Fluctuations*, page 389. North-Holland Publishing Company, 1982.

[9] Yu. B. Paderno, S. Pokrzywnicki, and B Stalinski. Magnetic properties of some rare earth hexaborides. *Phys. Stat. Sol.*, 24:K73–K76, 1967.

[10] J. C. Nickerson, R. M. White, K. N. Lee, R. Bachmann, T. H. Geballe, and G. W. Hull, Jr. Physical Properties of SmB_6. *Physical Review B*, 3(6):2030, 1971.

[11] V. V. Glushkov, A. V. Kuznetsov, O. A. Churkin, S. V. Demishev, Yu. B. Paderno, N. Yu. Shitsevalova, and N. E. Sluchanko. Spin gap formation in SmB_6. *Physica B*, 378-380:614–615, 2006.

[12] S. Yeo, K. Song, N. Hur, Z. Fisk, and P. Schlottmann. Effects of Eu doping on SmB_6 single crystals. *Physical Review B*, 85:115125, 2012.

[13] E. E. Vainshtein, S. M. Blokhin, and Yu. B. Paderno. X-ray spectral investigation of samarium hexaboride. *Soviet Physics - Solid State*, 6:2318, 1965.

[14] J.-N. Chazalviel, M Campagna, G. K. Wertheim, and P. H. Schmidt. Study of valence mixing in SmB_6 by x-ray photoelectron spectroscopy. *Physical Review B*, 14(10):4586, 1976.

[15] R. L. Cohen, M. Eibschutz, and K. W. West. Electronic and magnetic structure of SmB_6. *Physical Review Letters*, 24(8):383, 1970.

[16] J. W. Allen and R. M. Martin. Surface mixed valence in Sm and SmB_6. *Physical Review B*, 21(4):1335, 1980.

[17] C. M. Varma. Mixed-valence compounds. *Reviews of Modern Physics*, 48:219, 1976.

[18] M. B. Maple and D. Wohlleben. Nonmagnetic 4f shell in the high-pressure phase of SmS. *Physical Review Letters*, 27:511, 1971.

[19] F. Lapierre, M. Ribault, F. Holtzberg, and J. Flouquet. New states in SmS? *Solid State Communications*, 40:347, 1981.

[20] G. K. Wertheim, W. Eib, E. Kaldis, and M. Campagna. Mixed valency of TmSe. *Physical Review B*, 22:6240, 1980.

[21] J. M. Tarascon, Y. Isikawa, B. Chevalier, J. Etourneau, P. Hagenmuller, and M. Kasaya. Valence transition of samarium in hexaboride solid solutions $Sm_{1-x}M_xB_6$ (M = Yb^{2+}, Sr^{2+}, La^{3+}, Y^{3+}, Th^{4+}. *J. Physique*, 51:3877, 1980.

[22] T. Kasuya, K. Kojima, and M. Kasaya. Theory and experiment on SmB_6. In R. D. Parks, editor, *Valence Instabilities and Related Narrow-Band Phenomena*, page 137. Plenum Press, 1977.

[23] M. Kasaya, J. M. Tarascon, and J. Etourneau. Study of the valence transition in La- and Yb-substituted SmB_6. *Solid State Communications*, 33:1005–1007, 1980.

[24] J. Beille, M. B. Maple, J. Wittig, Z. Fisk, and L. E. DeLong. Suppression of the energy gap in SmB_6 under pressure. *Mat. Res. Bull*, 28(12):7397, 1983.

[25] E. Beaurepaire, J. P. Kappler, and G. Krill. X-ray-absorption near-edge structure study in mixed-valent samarium systems. *Physical Review B*, 41(10):6768, 1990.

[26] S. Nozawa, T. Tsukamoto, K. Kanai, T. Haruna, S. Shin, and S. Kunii. Ultrahigh-resolution and angle-resolved photoemission study of SmB_6. *Journal of Physics and Chemistry of Solids*, 63:1223–1226, 2002.

[27] S. Souma, H. Kumigashira, T. Ito, T. Takahashi, and S. Kunii. Direct observation of pseudogap of SmB_6 using ultrahigh-resolution photoemission spectroscopy. *Physica B*, 312-313:329–330, 2002.

[28] H. Miyazaki, T. Hajiri, T. Ito, S. Kunii, and S. Kimura. Momentum-dependent hybridization gap and dispersive in-gap state of the Kondo semiconductor SmB_6. *Physical Review B*, 86:075105, 2012.

[29] W. T. Fuhrman, J. Leiner, P. Nikolić, G. E. Granroth, M. B. Stone, M. D. Lumsden, L. DeBeer-Schmidtt, P. A. Alekseev, J.-M. Mignot, S. M. Mignot, S. M. Koohpayeh, P. Cottingham, W. A. Phelan, L. Schoop, T. M. Schoop, T. M. McQueen, and C. Broholm. Interaction driven subgap spin exciton in the Kondo insulator SmB_6. *Physical Review Letters*, 114:036401, 2015.

[30] I. V. Berman, N. B. Brandt, V. V. Moschalkov, S. N. Pashkevich, V. I. Sidorov, E. S. Konovalova, and Yu. B.Paderno. Effect of pressure on the correlation gap in a compound with intermediate valency SmB_6. *JETP Letters*, 38:477, 1983.

[31] J. C. Cooley, M. C. Aronson, Z. Fisk, and P. C. Canfield. SmB_6: Kondo Insulator or Exotic Metal? *Physical Review Letters*, 74(9):1629, 1995.

[32] A. Barla, J. Derr, J. P. Sanchez, B. Salce, G. Lapertot, B. P. Doyle, R. Ruffer, R. Lengsdorf, M. M. Abd-Elmeguid, and J. Flouquet. High-Pressure Ground State of SmB_6: Electronic Conduction and Long Range Magnetic Order. *Physical Review Letters*, 94:166401, 2005.

[33] J. Derr, G. Knebel, D. Braithwaite, B. Salce, J. Flouquet, K. Flachbart, S. Gabani, and N. Shitsevalova. From unconventional insulating behavior towards conventional magnetism in the intermediate-valence compound SmB_6. *Physical Review B*, 77:193107, 2008.

[34] A. Lacerda, D. Rickel, M. F. Hundley, P. C. Canfield, J. D. Thompson, Z. Fisk, P. Haen, and F. Lapierre. High field magnetoresistance in SmB_6. *Physica B*, 199-200:469–470, 1994.

[35] J. C. Cooley, M. C. Aronson, A. Lacerda, Z. Fisk, P. C. Canfield, and R. P. Guertin. High magnetic fields and the correlation gap in SmB_6. *Physical Review B*, 52(10):7322, 1995.

[36] Y. Nakajima, P. Syers, X. Wang, R. Wang, and J. Paglione. One-dimensional edge state transport in a topological Kondo insulator. *Nature Physics*, 12:213, 2015.

[37] S. Wolgast, Y. S. Eo, T. Ozturk, G. Li, Z. Xiang, C. Tinsman, T. Asaba, B. Lawson, F. Yu, J. W. Allen, K. Sun, L. Li, Ç. Kurdak, D.-J. Kim, and Z. Fisk. Magnetotransport measurements of the surface states of samarium hexaboride using Corbino structures. *Physical Review B*, 92:115110, 2015.

[38] K. Flachbart, S. Gabáni, E. Konovalova, Y. Paderno, and V. Pavlik. Pulsed magnetic field study of the spin gap in intermediate-valent SmB_6. *Physica B*, 404:2985–2987, 2009.

[39] S. Gabáni, G. Pristás, I. Takaáčová, N. Sluchanko, K. Siemensmeyer, N. Shitsevalova, V. Filipov, and K. Flachbart. Surface and bulk components of electrical conductivity

in the (presumably special topological) Kondo insulator SmB_6 at lowest temperatures. *Solid State Sciences*, 47:17, 2015.

[40] K. v. Klitzing, G. Dorda, and M. Pepper. New Method for Hihg-Accuracy Determination of the Fine-Structure Constant Based on Quantized Hall Resistance. *Physical Review Letters*, 45:494, 1980.

[41] D. J. Thouless, M. Kohmoto, M. P Nightingale, and M. den Nijs. Fractionalized Fermi liquid on the surface of a topological Kondo insulator. *Physical Review Letters*, 49:405, 1982.

[42] C. L. Kane and E. J. Mele. Quantum spin Hall effect in graphene. *Physical Review Letters*, 95:226801, 2005.

[43] C. L. Kane and E. J. Mele. Z_2 topological order and the quantum spin Hall effect. *Physical Review Letters*, 95:146802, 2005.

[44] B. A. Bernevig, T. L. Hughes, and S.-C. Zhang. Quantum spin Hall effect and topological phase transition in HgTe quantum wells. *Science*, 314(5806):1757, 2006.

[45] M. Konig and S. Wiedmann and C. Brune and A. Roth and H. Buhmann and L. W. Molenkamp and X.-L. Qi and S.-C. Zhang. Quantum spin Hall insulator state in HgTe quantum wells. *Science*, 318(5851):766, 2007.

[46] L. Fu, C. L. Kane, and G. Mele. Topological insulators in three dimensions. *Physical Review Letters*, 98:106803, 2007.

[47] J. E. Moore and L. Balents. Topological invariants of time-reversal-invariant band structures. *Physical Review B*, 75:121306, 2007.

[48] L. Fu and C. L. Kane. Topological insulators with inversion symmetry. *Physical Review B*, 76:045302, 2007.

[49] Y. Ando. Topological Insulator Materials. *Journal of the Physical Society of Japan*, 82:102001, 2013.

[50] Y. S. Eo. *Surface and bulk transport of samarium hexaboride*. PhD thesis, University of Michigan, 2017.

[51] M. Dzero, K. Sun, V. Galitski, and P. Coleman. Topological Kondo insulators. *Physical Review Letters*, 104:106408, 2010.

[52] T. Takimoto. SmB_6: A promising candidate for a topological insulator. *Journal of the Physical Society of Japan*, 80:123710, 2011.

[53] M. Dzero, K. Sun, P. Coleman, and V. Galitski. Theory of topological Kondo insulators. *Physical Review B*, 85:045130, 2012.

[54] F. Lu, J. Zhao, H. Weng, Z. Fang, and X. Dai. Correlated topological insulators with mixed valence. *Physical Review Letters*, 110:096401, 2013.

[55] L. Li, K. Sun, C. Kurdak, and J. W. Allen. Emergent mystery in the Kondo insulator samarium hexaboride. *Nature Reviews Physics*, 2:463–479, 2020.

[56] S. Wolgast, Ç. Kurdak, K. Sun, J. W. Allen, D.-J. Kim, and Z. Fisk. Low-temperature surface conduction in the Kondo insulator SmB_6. *Physical Review B*, 88:180405(R), 2013.

[57] D. J. Kim, S. Thomas, T. Grant, J. Botimer, Z. Fisk, and J. Xia. Surface Hall effect and nonlocal transport in SmB_6: evidence for surface conduction. *Scientific Reports*, 3:3150, 2013.

[58] P. Syers, D. Kim, M. S. Fuhrer, and J. Paglione. Tuning bulk and surface conduction in the proposed topological Kondo insulator SmB_6. *Physical Review Letters*, 114:096601, 2015.

[59] Q. Song, J. Mi, D. Zhao, T. Su, W. Yuan, W. Xing, Y. Chen, T. Wang, T. Wu, X. H. Chen, X. C. Xie, C. Zhang, J. Shi, and W. Han. Spin injection and inverse Edelstein effect in the surface states of topological Kondo insulator SmB_6. *Nature Communications*, 7:13485, 2016.

[60] J. D. Denlinger, J. W. Allen, J.-S. Kang, K. Sun, B. I. Min, Dae-Jeong Kim, and Z. Fisk. SmB_6 Photoemission: Past and Present. In *Proceedings of the International Conference on Strongly Correlated Electron Systems*, volume 3, page 017038. JPS, 2014.

[61] M. Neupane, N. Alidoust, S.-Y. Xu, T. Kondo, Y. Ishida, D. J. Kim, Chang Liu, I. Belopolski, Y. J. Jo, T.-R. Chang, H.-T. Jeng, T. Durakiewicz, L. Balicas, H. Lin, A. Bansil, S. Shin, Z. Fisk, and M. Z. Hasan. Surface electronic structure of the topological Kondo insulator candidate correlated electron system SmB_6. *Nature Communications*, 4:2991, 2013.

[62] N. Xu, P. K. Biswas, J. H. Dil, R. S. Dhaka, G. Landolt, S. Muff, C. E. Matt, X. Shi, N. C. Plumb, M. Radovic, E. Pomjakushina, K. Conder, A. Amato, S. V. Borisenko, R. Yu, H. M. Weng, Z. Fang, X. Dai, J. Mesot, H. Ding, and M. Shi. Direct observation of the spin texture in SmB_6 as evidence of the topological Kondo insulator. *Nature Communications*, 5:4566, 2014.

[63] J. Jiang, S. Li, T. Zhang, Z. Sun, F. Chen, Z. R. Ye, M. Xu, Q. Q. Ge, S. Y. Tan, X. H. Niu, M. Xia, B. P. Xie, Y. F. Li, X. H. Chen, H. H. Wen, and D. L. Feng. Observation of possible topological in-gap surface states in the Kondo insulator SmB_6 by photoemission. *Nature Communications*, 4:3010, 2013.

[64] E. Frantzeskakis, N. de Jong, B. Zwartsenberg, Y. K. Huang, Y. Pan, X. Zhang, J. X. Zhang, F. X. Zhang, L. H. Bao, O. Tegus, A. Varykhalov, A. de Visser, and M. S. Golden. Kondo hybridization and the origin of metallic states at the (001) surface of SmB_6. *Physical Review X*, 3:041024, 2013.

[65] Z.H. Zhu, Z. Nicolaou, G. Levy, N. P. Butch, P. Syers, X. F. Wang, J. Paglione, G. A. Sawatzky, I. S. Elfimov, and A. Damascelli. Polarity-driven surface metallicity in SmB_6. *Physical Review Letters*, 111:216402, 2013.

[66] P. Hlawenka, K. Siemensmeyer, E. Weschke, A. Varykhalov, J. Sánchez-Barriga, N. Y. Shitsevalova, A. V. Dukhnenko, V. B. Filipov, S. Gabáni, K. Flachbart, O. Rader,

and E. D. L. Rienks. Samarium hexaboride is a trivial surface conductor. *Nature Communications*, 9:517, 2018.

[67] H. Hermann, P. Hlawenka, K. Siemensmeier, E. Weschke, J. Sánchez-Barriga, A. Varykhalov, N. Y. Shitsevalova, A. V. Dukhnenko, V. B. Filipov, S. Gabáni, K. Flachbart, O. Rader, M. Sterrer, and E. D. L. Rienks. Contrast reversal in scanning tunneling microscopy and its implications for the topological classification of SmB_6. *Advanced Materials*, 32:1906725, 2020.

[68] J. D. Denlinger, J. W. Allen, J.-S. Kang, K. Sun, J.-W. Kim, J. H. Shim, B. I. Min, Dae-Jeong Kim, and Z. Fisk. Temperature dependence of linked gap and surface state evolution in the mixed valent topological insulator SmB_6, 2014. arXiv:1312.6637 [cond-mat.str-el].

[69] J. D. Denlinger, S. Jang, G. Li, L. Chen, B. J. Lawson, T. Asaba, C. Tinsman, F. Yu, K. Sun, J. W. Allen, Ç. Kurdak, D.-J. Kim, Z. Fisk, and L. Li. Consistency of photoemission and quantum oscillations for surface states of SmB_6, 2016. arXiv:1601.07408 [cond-mat.str-el].

[70] M. M. Yee, Y. He, A. Soumyanarayanan, D.-J. Kim, Z. Fisk, and J. E. Hoffman. Imaging the Kondo insulating gap on SmB_6, 2013. arXiv:1308.1085 [cond-mat.str-el].

[71] S. Rößler, T.-H. Jang, D.-J. Kim, L. H. Tjeng, Z. Fisk, F. Steglich, and S. Wirth. Hybridization gap and Fano resonance in SmB_6. *Proc. Natl. Acad. Sci. USA*, 111:4798, 2014.

[72] S. Rößler, L. Jiao, D.-J. Kim, S. Seiro, K. Rasim, F. Steglich, L. H. Tjeng, Z. Fisk, and S. Wirth. Surface and electronic structure of SmB_6 through scanning tunneling microscopy. *Philosophical Magazine*, 96(31):3262–3273, 2016.

[73] C. E. Matt, H. Pirie, A. Soumyanarayanan, M. M. Yee, Y. He, D. T. Larson, W. S. Paz, J. J. Palacios, M. H. Hamidian, and J. E. Hoffman. Consistency between ARPES and STM measurements on SmB_6. *Physical Review B*, 101:085142, 2020.

[74] H. Pirie, Y. Liu, A. Soumyanarayanan, P. Chen, Y. He, M. M. Yee, P. F. S. Rosa, J. D. Thompson, D.-J. Kim, Z. Fisk, X. Wang, J. Paglione, D. K. Morr, M. H. Hamidian, and J. E. Hoffmann. Imaging emergent heavy Dirac fermions of a topological Kondo insulator. *Nature Physics*, 16:52, 2020.

[75] Y. Ohtsubo, Y. Yamashita, K. Hagiwara, S. Ideta, K. Tanaka, R. Yukawa, K. Horiba, H. Kumigashira, K. Miyamoto, T. Okuda, W. Hirano, F. Iga, and S. Kimura. Nontrivial surface states of samarium hexaboride at the (111) surface. *Nature Communications*, 10:2298, 2019.

[76] S. Thomas, D. J. Kim, S. B. Chung, T. Grant, Z. Fisk, and J. Xia. Weak antilocalization and linear magnetoresistance in the surface state of SmB_6. *Physical Review B*, 94:205114, 2016.

[77] S. Biswas, R. Nagarajan, S. Sarkar, K. R. Amin, M. C. Hatnean, S. Tewari, G. Balakrishnan, and A. Bid. Robust local and nonlocal transport in the topological Kondo insulator SmB_6 in the presence of a high magnetic field. *Physical Review B*, 92:085103, 2015.

[78] F. Chen, C. Shang, Z. Jin, D. Zhao, Y. P. Wu, Z. J. Xiang, Z. C. Xia, A. F. Wang, X. G. Luo, T. Wu, and X. H. Chen. Magnetoresistance evidence of a surface state and a field-dependent insulating state in the Kondo insulator SmB_6. *Physical Review B*, 91:205133, 2015.

[79] M. Shahrokhvand, S. Pezzini, M. R. van Delft, U. Zeitler, N. E. Hussey, and S. Wiedmann. Bulk and in-gap states in SmB_6 revealed by high-field magnetotransport. *Physical Review B*, 96:205125, 2017.

[80] P. C. Canfield and Z. Fisk. Growth of single crystals from metallic fluxes. *Philosophical Magazine B*, 65:6:1117, 1992.

[81] W. A. Phelan, S. M. Koohpayeh, P. Cottingham, J. A. Tutmaher, J. C. Leiner, M. D. Lumsden, C. M. Lavelle, X. P. Wang, C. Hoffmann, M. A. Siegler, N. Haldolaarachchige, D. P. Young, and T. M. McQueen. On the chemistry and physical

properties of flux and floating zone grown SmB_6 single crystals. *Scientific Reports*, 6:20860, 2016.

[82] M. C. Hatnean, M. R. Lees, D. McK. Paul, and G. Balakrishnan. Large, high quality single-crystals of the new topological Kondo insulator, SmB_6. *Scientific Reports*, 3:307, 2013.

[83] G. Li, Z. Xiang, F. Yu, T. Asaba, B. Lawson, P. Cai, C. Tinsman, A. Berkley, S. Wolgast, Y. S. Eo, D.-J. Kim, C. Kurdak, J. W. Allen, K. Sun, X. H. Cheng, Y. Y. Wang, Z. Fisk, and L. Li. Two-dimensional Fermi surfaces in Kondo insulator SmB_6. *Science*, 346:1208, 2014.

[84] B. S. Tan, Y.-T. Hsu, B. Zeng, M. Ciomaga Hatnean, N. Harrison, Z. Zhu, M. Hartstein, M. Kiourlappou, A. Srivastava, M. D. Johannes, T. P. Murphy, J.-H. Park, L. Balicas, G. G. Lonzarich, G. Balakrishnan, and S. E. Sebastian. Unconventional Fermi surface in an insulating state. *Science*, 349:6245, 2015.

[85] M. Hartstein, W. H. Toews, Y.-T. Hsu, B.Zeng, X. Chen, M. C. Hatnean, Q. R. Zhang, S. Nakamura, A. S. Padgett, G. Rodway-Gant, J. Berk, M. K. Kingston, G. H. Zhang, M. K. Chan, S. Yamashita, T. Sakakibara, Y. Tanako, J.-H. Park, L. Balicas, N. Harrison, N. Shitsevalova, G. Balakrishnan, G. G. Lonzarich, R. W. Hill, M. Sutherland, and S. E. Sebastian. Fermi surface in the absence of a Fermi liquid in the Kondo insulator SmB_6. *Nature Physics*, 14:166, 2017.

[86] Y. Xu, S. Cui, J. K. Dong, D. Zhao, T. Wu, X. H. Chen, K. Sun, H. Yao, and S. Y. Li. Bulk Fermi surface of charge-neutral excitations in SmB_6 or not: a heat-transport study. *Physical Review Letters*, 116:246403, 2016.

[87] M.-E. Boulanger, F. Laliberté, M. Dion, S. Badoux, N. Doiron-Leyraud, W. A. Phelan, S. M. Koohpayeh, W. T. Fuhrman, J. R. Chamorro, T. M. McQueen, X. F. Wang, Y. Nakajima, T. Metz, J. Paglione, and L. Taillefer. Field-dependent heat transport in the topological Kondo insulator SmB_6: Phonons scattered by magnetic impurities. *Physical Review B*, 97:245141, 2018.

[88] Y. S. Eo, S. Wolgast, A. Rakoski, D. Mihaliov, B. Y. Kang, M. S. Song, B. K. Cho, M. Ciomaga Hatnean, G. Balakrishnan, Z. Fisk, S. R. Saha, X. Wang, J. Paglione, and Ç. Kurdak. Comprehensive surface magnetotransport study of SmB_6. *Physical Review B*, 101:155109, 2020.

[89] W. T. Fuhrman, J. R. Chamorro, P. A. Alekseev, J.-M. Mignot, T. Keller, J. A. Rodriguez-Rivera, Y. Qiu, P. Nikolić T. M. McQueen, and C. Broholm. Screened moments and extrinsic in-gap states in samarium hexaboride. *Nature Communications*, 9:1539, 2018.

[90] J. C. Souza, P. F. S. Rosa, J. Sichelschmidt, M. Carlone, P. A. Venegas, M. O. Malcolms, P. M. Menegasso, R. R. Urbano, Z. Fisk, and P. G. Pagliuso. Metallic islands in the Kondo insulator SmB_6, 2020. arXiv:2010.03719 [cond-mat.str-el].

[91] W. T. Fuhrman and P. Nikolić. Magnetic impurities in Kondo insulators and the puzzle of samarium hexaboride, 2018. arXiv:1807.00005v1 [cond-mat.str-el].

[92] S. Gabáni, M. Orendáč, G. Pristáš, E. Gažo, P. Diko, S. Piovarči, V. Glushkov, N. Sluchanko, A. Levchenko, N. Shitsevalova, and K. Flachbart. Transport properties of variously doped SmB_6. *Philosophical Magazine*, 96(31):3274–3283, 2016.

[93] Y. S. Eo, A. Rakoski, J. Lucien, D. Mihaliov, Ç. Kurdak, P. F. S. Rosa, and Z. Fisk. Transport gap in SmB_6 protected against disorder. *Proceedings of the National Academy of Sciences*, 116(26):12638, 2019.

[94] H. Shen and L. Fu. Quantum oscillation from in-gap states and a non-Hermitian Landau level problem. *Physical Review Letters*, 121:026403, 2018.

[95] N. Harrison. Highly asymmetric nodal semimetal in bulk SmB_6. *Physical Review Letters*, 121:026602, 2018.

[96] Z. Xiang, B. Lawson, T. Asaba, C. Tinsman, L. Chen, C. Shang, X. H. Chen, and L. Li. Bulk rotational symmetry breaking in Kondo insulator SmB_6. *Physical Review X*, 7:031054, 2017.

[97] S. Gabáni, K. Flachbart, E. Konovalova, M. Orendáč, Y. Paderno, V. Pavlík, and J. Šebek. Properties of the in-gap states in SmB_6. *Solid State Communications*, 117:641–644, 2001.

[98] S. M. Thomas, X. Ding, F. Ronning, V. Zapf, J. D. Thompson, Z. Fisk, J. Xia, and P. F. S. Rosa. Quantum oscillations in flux-grown SmB_6 with embedded aluminum. *Physical Review Letters*, 122:166401, 2019.

[99] M. Hartstein, H. Liu, Y.-T. Hsu, B. S. Tan, M. Ciomaga Hatnean, G. Balakrishnan, and S. E. Sebastian. Intrinsic bulk quantum oscillations in a bulk unconventional insulator SmB_6. *iScience*, 23:101632,, 2020.

[100] S. Wolgast, Y. S. Eo, K. Sun, L. Li, Ç. Kurdak, F. F. Balakirev, M. Jaime, D.-J. Kim, and Z. Fisk. Reduction of the low-temperature bulk gap in samarium hexaboride under high magnetic fields. *Physical Review B*, 95:245112, 2017.

[101] P. K. Liao, K. E. Spear, and M. E. Schlesinger. The B-Sm (boron-samarium) system. *Journal of Phase Equilibria*, 17(4):348, 1996.

[102] S. M. Koohpayeh, D. Fort, and J. S. Abell. The optical floating zone technique: A review of experimental procedures with special reference to oxides. *Progress in Crystal Growth and Characterization of Materials*, 54:121–137, 2008.

[103] Z. Fisk, A. S. Cooper, P. H. Schmidt, and R. N. Castellano. Preparation and lattice parameter of the rare earth tetraborides. *Mat. Res. Bull*, 7:285–288, 1972.

[104] G. D. Sturgeon, J.-P. Mercurio, J. Etourneau, and P. Hagenmuller. Single crystals of SmB_6 for conductivity and other measurements. *Mat. Res. Bull*, 9:117–120, 1974.

[105] Y. Luo, H. Chen, J. Dai, Z. Xu, and J. D. Thompson. Heavy surface state in a possible topological Kondo insulator: Magnetothermoelectric transport on the (001) plane of SmB_6. *Physical Review B*, 91:075130, 2015.

[106] K. A. Gschneider and F. W. Calderwood. The Al-Sm (Aluminum-Samarium) System. *Bulletin of Alloy Phase Diagrams*, 10(1):37, 1989.

[107] S. Kimura and K. Kitamura. Floating zone crystal growth and phase equilibria: a review. *Journal of the American Ceramic Society*, 75(6):1440–46, 1992.

[108] Y. S. Eo, A. Rakoski, S. Sinha, D. Mihaliov, W. T. Fuhrman, S. R. Saha, P. F. S. Rosa, Z. Fisk, M. Ciomaga Hatnean, G. Balakrishnan, J. R. Chamorro, S. M. Koohpayeh, T. M. McQueen, B. Kang, M. Song, B. Cho, M. S. Fuhrer, J. Paglione, and Ç. Kurdak. Bulk transport paths through defects in floating zone and Al flux grown SmB_6. *Journal of Superconductivity and Novel Magnetism*, 2020. arXiv:2011.08923 [cond-mat.str-el].

[109] A. Ourmazd. The electrical properties of dislocations in semiconductors. *Contemporary Physics*, 25:251, 1984.

[110] D. Hull and D. J. Bacon. *Introduction to Dislocations*. Elsevier, Ltd., 5 edition, 2011.

[111] S. Wolgast, Y. S. Eo, Ç. Kurdak, D.-J. Kim, and Z. Fisk. Conduction through subsurface cracks in bulk topological insulators, 2015. arXiv:1506.08233 [cond-mat.str-el].

[112] A. Kebede, M. C. Aronson, C. M. Buford, P. C. Canfield, J. H. Cho, B. R. Coles, J. C. Cooley, J. Y. Coulter, Z. Fisk, J. D. Goettee, W. L. Hults, A. Lacerda, T. D. McLendon, P. Tiwari, and J. L. Smith. Studies of the correlated electron system SmB_6. *Physica B*, 223-224:256–259, 1996.

[113] L. J. van der Pauw. A method of measuring specific resistivity and Hall effect of discs of arbitrary shape. *Philips Research Reports*, 13:1:1–9, 1958.

[114] O. M. Corbino. Azioni elettromagnetiche dovute agli ioni dei metalli deviati dalla traiettoria normale per effetto di un campo. *Nuovo Cimento*, 1:397, 1911.

[115] Y. S. Eo, K. Sun, Ç. Kurdak, D.-J. Kim, and Z. Fisk. Inverted resistance measurements as a method for characterizing the bulk and surface conductivities of three-dimensional topological insulators. *Physical Review Applied*, 9:044006, 2018.

[116] N. E. Sluchanko, A. A. Volkov, V. V. Glushkov, B. P. Gorshunov, S. V. Demishev, M. V. Kondrin, A. A. Pronin, N. A. Samarin, Y. Bruynseraede, V. V. Moshchalkov, and S. Kunii. Nature of the low-temperature anomalies in the physical properties of

the intermediate-valent compound SmB_6. *Journal of Experimental and Theoretical Physics*, 88:533, 1999.

[117] K. Flachbart, S. Gabáni, E. Konovalova, Y. Paderno, and V. Pavlik. Ground state formation in intermediate-valent SmB_6. *Physica B*, 293:417–421, 2001.

[118] E. Hall. Variation of hardness of metals with grain size. *Nature*, 173(4411):948–949, 1954.

[119] P. P. Debye and E. M. Conwell. Electrical properties of n-type germanium. *Physical Review*, 93:693, 1954.

[120] P. W. Chapman, O. N. Tufte, J. D. Zook, and D. Long. Electrical properties of heavily doped silicon. *Journal of Applied Physics*, 34:3291, 1963.

[121] T. H. Geballe, A. Menth, E. Buehler, and G. W. Hull. Properties of SmB_6 doped with Eu and Gd. *Journal of Applied Physics*, 41:904, 1970.

[122] D. J. Kim, J. Xia, and Z. Fisk. Topological surface state in the Kondo insulator samarium hexaboride. *Scientific Reports*, 13:466, 2014.

[123] W. T. Fuhrman, J. C. Leiner, J. W. Freeland, M. van Veenendaal, S. M. Koohpayeh, W. A. Phelan, T. M. McQueen, and C. Broholm. Diamagnetic Sm^{3+} in the topological Kondo insulator SmB_6. *Physical Review B*, 99:020401(R), 2019.

[124] W. Kohn. Effective mass theory in solids from a many-particle standpoint. *Physical Review*, 105:509, 1957.

[125] A. Rakoski, Y. S. Eo, K. Sun, and Ç. Kurdak. Understanding low-temperature bulk transport in samarium hexaboride without relying on in-gap bulk states. *Physical Review B*, 95:195133, 2017.

[126] B. Skinner. Properties of the donor impurity band in mixed valence insulators. *Physical Review Materials*, 3:104601, 2019.

[127] R. Hall and J. C. Bean. Misfit dislocations in lattice-mismatched epitaxial films. *Critical Reviews in Solid State and Material Sciences*, 17:507, 1992.

[128] M. Kasaya, H. Kimura, Y. Isikawa, T. Fujita, and T. Kasuya. Valence instabilities and electrical properties of the La- and Yb-substituted SmB_6. In L.M. Falicov, W. Hanke, and M.B. Maple, editors, *Valence Fluctuations in Solids*, page 251. North-Holland Publishing Company, 1981.

[129] A. Rakoski, Y. S. Eo, K. Sun, and Ç. Kurdak. Investigation of high-temperature bulk transport characteristics and skew scattering in samarium hexaboride. *Journal of Superconductivity and Novel Magnetism*, 33(1):265, 2020.

[130] J. T. Ye, S. Inoue, K. Kobayashi, Y. Kasahara, H. T. Yuan, H. Shimotani, and Y. Iwasa. Liquid-gated interface superconductivity on an atomically flat film. *Nat. Mater.*, 9(2):125, 2010.

[131] T. Sato, S. Marukane, and T. Morinag. Ionic Liquids for the Electric Double Layer Capacitor Applications. In Scott Handy, editor, *Applications of Ionic Liquids in Science and Technology*, chapter 6. IntechOpen, 2011.

[132] D. M. McCann, M. Misek, K. V. Kamenev, and A. D. Huxley. Pressure-Temperature Phase Diagram of Ionic Liquid Dielectric DEME-TFSI. *Physics Procedia*, 75:252, 2015.

[133] H. Yuan, H. Shimotani, A. Tsukazaki, A. Ohtomo, M. Kawasaki, and Y. Iwasa. High-density carrier accumulation in ZnO field-effect transistors gated by electric double layers of ionic liquids. *Advanced Functional Materials*, 19:1046, 2009.

[134] S. Gabáni, E. Bauer, M. Della Mea, K. Flachbart, Y. Paderno, V. Pavlík, and N. Shitsevalova. Insulator-metal phase transition in SmB_6 under pressure. *Journal of Magnetism and Magnetic Materials*, 272-276:397–399, 2004.

[135] A. Stern, M. Dzero, V. M. Galitski, Z. Fisk, and J. Xia. Surface-dominated conduction up to 240 K in the Kondo insulator SmB_6 under strain. *Nature Materials*, 16:708–711, 2017.

[136] C. W. Hicks, M. E. Barber, S. D. Edkins, D. O. Brodsky, and A. P. Mackenzie. Piezoelectric-based apparatus for strain tuning. *Review of Scientific Instruments*, 85:065003, 2014.

[137] T. Tamaki, T. Goto, S. Kunii, M. Kasaya, T. Suzuki, , T. Fujimura, and T. Kasuya. Elastic properties of SmB_6 and Sm_3Se_4. *Journal of Magnetism and Magnetic Materials*, 47&48:469–471, 1985.